

Search for hidden photons as dark matter candidates with the FUNK experiment

Zur Erlangung des akademischen Grades eines

Doktors der Naturwissenschaften

von der KIT-Fakultät für Physik des
Karlsruher Instituts für Technologie (KIT)

genehmigte

Dissertation

von

M. Sc. Arnaud Andrianavalomahefa

aus Antananarivo, Madagaskar

Tag der mündlichen Prüfung: 13. Dezember 2019

Referent: Prof. Dr. Thomas Schwetz

Korreferent: Prof. Dr. Ralph Engel

Betreuer: Dr. Darko Veberič, Prof. Dr. Ralph Engel

Abstract

The origin and nature of dark matter are one of the biggest open questions in modern science. There is a class of hypotheses in which hidden photons, postulated in an extension of the standard model of particle physics, are the origin of dark matter. Those hidden photons are produced in a non-thermal process in the early universe and can have a wide range of masses. Many experiments have been set up to search for such photons in different kinematic ranges.

In this work, we present a novel setup, assembled at the Karlsruhe Institute of Technology, to search for hidden photon signatures in the dark matter halo. Our experiment uses a large spherical mirror to induce the conversion of local hidden-photon dark matter into real detectable photons through a Maxwellian-like transition. These photons can be collected at the center of curvature of the mirror and their wavelength is directly related to the mass of the hidden photons.

We report on the experimental strategies and measurement campaigns performed in the visible and near-UV spectra, to search for hidden-photon dark matter in the eV mass range. In this regime, we expect that our setup could be sensitive to a rate as low as one detectable hidden-photon-to-photon conversion every ~ 15 min, allowing us to probe formerly uncharted region of the parameter space.

We scanned the visible and near-UV range of frequencies and searched for hidden photons with masses between 2 eV and 8 eV. The result from our latest data runs provides the up-to-date strongest limit for direct hidden-photon searches in this region of the parameter space. This work is in part published in several conference proceedings (a) and will be the basis an upcoming publication (b).

In a second part of this work, we discuss the future challenges of the experiment and aim at hunts for hidden-photon dark matter with lower masses.

-
- (a) A. Andrianavalomahefa, et al., *Search for dark photons as candidates for dark matter with FUNK*, Proc. 36th Int. Cosmic Ray Conf. (ICRC2019).
 - (b) A. Andrianavalomahefa, et al., *Limits from the FUNK experiment on the mixing strength of hidden-photon dark matter in the visible and near-ultraviolet wavelength range*, submitted to Phys. Rev. D.

Zusammenfassung

Der Ursprung der Dunklen Materie ist eine der größten offenen Fragen der modernen Wissenschaft. Eine mögliche teilchenphysikalische Erklärung der Dunklen Materie stellen "verborgenen Photonen" dar, die in Erweiterungen des Standardmodells der Teilchenphysik postuliert werden. Diese verborgenen Photonen werden in einem nicht-thermischen Prozess im frühen Universum erzeugt und können ein breites Spektrum an Massen aufweisen. Viele Experimente wurden bisher durchgeführt, um nach solchen Photonen in verschiedenen kinematischen Bereichen zu suchen.

In dieser Arbeit präsentieren wir ein neuartiges Experiment, das am Karlsruher Institut für Technologie aufgebaut wurde, um nach der Signatur verborgener Photonen im Halo der Dunklen Materie zu suchen. Unser Experiment verwendet einen großen sphärischen Spiegel, um die Umwandlung lokaler verborgener Photonen in echte nachweisbare Photonen durch einen Maxwell'schen Übergang zu induzieren. Diese Photonen können im Krümmungszentrum des Spiegels gesammelt werden und ihre Wellenlänge steht in direktem Zusammenhang mit der Masse der verborgenen Photonen.

Wir berichten über die experimentellen Strategien und Messkampagnen im sichtbaren und nahem UV Licht, um nach Dunkler Materie mit verborgenem Photon im eV-Massenbereich zu suchen. In diesem Regime erwarten wir eine hohe Empfindlichkeit unseres Experiments und könnten eine Rate von Konvertierungen von verborgene Photonen zu Photonen von bis zu 0.25/Stunde nachweisen und damit einen bisher unerforschten Bereich des Parameterraums untersuchen.

Unsere Messungen im sichtbaren und nahem UV Frequenzbereich erlauben die Suche nach verborgenen Photonen mit Massen zwischen 2 eV und 8 eV. Das Ergebnis der Datenanalyse ergibt die aktuell stärksten Grenzen für die direkte Suche nach verborgenen Photonen in diesem Bereich des Parameterraums. Diese Arbeit wurde teilweise in mehreren Konferenzberichten veröffentlicht (a) und bildet die Grundlage für eine bevorstehende Veröffentlichung (b).

In einem zweiten Teil dieser Arbeit diskutieren wir die zukünftigen Herausforderungen des Experiments und zielen auf die Suche nach Dunkler Materie mit geringerer Masse.

-
- (a) A. Andrianavalomahefa, et al., *Search for dark photons as candidates for dark matter with FUNK*, Proc. 36th Int. Cosmic Ray Conf. (ICRC2019).
 - (b) A. Andrianavalomahefa, et al., *Limits from the FUNK experiment on the mixing strength of hidden-photon dark matter in the visible and near-ultraviolet wavelength range*, submitted to Phys. Rev. D.

Contents

1	Introduction	1
2	Hidden Photons	5
2.1	General picture	6
2.2	HP-Photon mixing	10
2.3	Hidden-Photon Dark Matter	16
2.4	Search for HPDM with a dish antenna	21
3	The FUNK experiment	31
3.1	General setup	32
3.2	Search in the near-UV and visible spectra	37
3.3	A glimpse into FUNK++	57
4	Background photons	63
4.1	Internal background	63
4.2	Thermal radiation	66
4.3	Cherenkov radiation	68
5	Data analysis	77
5.1	Background measurement	78
5.2	Standard measurement	83
5.3	Deviation from homogeneous Poissonian process	93
5.4	Memory effect	101
5.5	Fourier analysis	113
5.6	Systematical uncertainties	116
5.7	Improved exclusion limit	120
6	Summary and conclusions	123
A	Flux of particles entering a box	127
A.1	Downward muons crossing a horizontal surface	127
A.2	Downward muons crossing one side of a vertical surface	127
A.3	Average path-length	129

CONTENTS

B Miscellaneous	131
B.1 Average Signal power	131
B.2 Width of the Signal	132
B.3 Microwave techniques	134
Acknowledgements	139
Acronyms	141
Bibliography	143

1

Introduction

To the best of our understanding of Cosmology, the Universe needs a sizable amount of non-luminous matter. This Dark Matter (DM) represents about 27% of the energy budget of the Universe.

The first conclusive hint came in 1933 from Zwicky, after his observation of the kinematics of galaxies near the edge of the Coma cluster and the estimated light-to-mass ratio of this cluster [1]. In the years since, the number of evidences for DM has grown and they come from different important epochs of Cosmology. Starting from the observations of the rotational curves of galaxies [2], the inferred baryonic and total mass densities of galaxy clusters [3], gravitational lensing [4], the dynamics of collisions between galaxy clusters [5], tracing back to the epoch of structure formation [6], and to the very early moments of the Universe with the remarkable agreement between independent measurements from the Cosmic Microwave Background (CMB) [7] and the abundance of primordial elements from the Big Bang Nucleosynthesis (BBN) to predict the fraction of baryonic matter in the Universe [8].

Obtaining a consistent picture across this entire range of observations turns out to be difficult to realize with alternative theories inclined to a modification of gravity [9]. Hence the paradigm has somewhat shifted towards particle DM. On the other hand, DM in the form of ordinary matter bound into Massive Compact Halo Objects (MACHOs) are, from one side, widely excluded by searches for gravitational microlensing [10], and from the other, not compatible with the abundance of primordial elements produced from the BBN. The latest data from Planck [11] suggests that the density parameter of the matter content of the Universe is $\Omega_m = 0.315 \pm 0.007$. Only ~15% of this fraction is fed by the baryon density, while the other ~85% is the form of Cold DM. The need of a cold and collisionless DM is claimed to explain the formation of galaxies and large-scale structures in the Λ CDM cosmology. These realizations also force us to look for DM particle beyond the Standard Model (SM).

There are no shortage of candidates from theories and at all energy scale. In the last decades, most of the experimental efforts favored the search for a whole category of new heavy particles, known as Weakly Interacting Massive Particles (WIMPs). These particles have a mass in the GeV to TeV range and they interact only weakly with SM particles. Their existence are naturally backed up by models of supersymmetry [12] and they are typically produced through a mechanism of thermal freeze-out in the early Universe. Nevertheless, the constant null results confirmed by recent measurements [13], while nearing the irreducible background floor of coherent neutrino scattering, begin to cast some doubts about WIMPs. At the same time, this also shed lights on the other candidates.

Only recently, more attention has been devoted to search for the lower-mass alternatives, known as Weakly Interacting Slim Particles (WISPs) which, besides other fundamental theoretical motivations, also provide natural Cold DM [14]. Axions and massive Hidden Photons (HPs) figure amongst the popular WISPs. This thesis is focused on HP particles as DM candidates. The HPs come from a simple class of extensions of the SM containing an additional $U(1)$ gauge symmetry, as predicted by many theories [14, 15]. They do not need to be DM. If they exist in nature, they would kinetically mix with ordinary photons [16] and thus opening many windows beyond the SM [17].

In a similar fashion to the misalignment mechanism invoked for the axions, HPs can also be non-thermally produced in the early universe and survive as a Cold DM condensate until present [18]. This is the DM candidate we are aiming at. This production mechanism yields a large phase space compatible with Cold DM signatures. In recent years, considerable progresses have been made to constrain the viable parameter space from both astrophysical and cosmological observations as well as from laboratory experiments which are rather dedicated for axion searches [19]. One drawback of these experiments is that they are often tuned to resonate with the specific axion or HP mass, which trades a very slow scan of the mass against a huge sensitivity.

In 2013, the authors of [20] proposed a new technique, based on a *dish antenna*, which combines both a high sensitivity and a broadband scan. The idea is to use a spherical metallic plate which can focus at its center of curvature, a tiny electromagnetic flux induced by the HPs. The first experimental setup was realized in Tokyo [21, 22] by using a $\sim 0.2 \text{ m}^2$ parabolic mirror and scanning in the optical range of frequencies. At the Karlsruhe Institute of Technology, the FUNK experiment deploys a spherical mirror about 70 times larger and with an extended sensitivity range.

This thesis is structured as follows. In Chapter 2, we give an overview of the physics of HPs and we review the detection principle using a dish antenna. In Chapter 3, we describe in details the setup of the FUNK experiment and discuss the search strategies in the near-UV and visible spectra. Furthermore, we examine the possibility of future searches at different range of frequencies. In Chapter 4, we study the various sources background of the experiment. In Chapter 5, we present a detailed analysis of the measurements and in Chapter 6 we summarize and conclude on our findings.

2

Hidden Photons

Contents

2.1	General picture	6
2.1.1	Propagation and Interaction eigenstates	6
2.1.2	Indirect and Direct constraints	7
2.2	HP-Photon mixing	10
2.2.1	Modified Maxwell's equations	11
2.2.2	Propagation in vacuum	12
2.2.3	Propagation in matter	12
2.3	Hidden-Photon Dark Matter	16
2.3.1	Production and Parameter space	16
2.3.2	HPDM condensate	19
2.3.3	Laboratory searches	20
2.4	Search for HPDM with a dish antenna	21
2.4.1	Surface emission	22
2.4.2	Directionality	24
2.4.3	Signal power	26
2.4.4	Sensitivity	28

In the most elementary scenario, the Standard Model (SM) of particle physics can be extended by an additional $U(1)$ gauge group. The gauge boson associated with this new Abelian group is known as Hidden Photon (HP) or dark photon or also para-photon^a. Such a feature tends to generically arise as a residual symmetry of many higher-dimensional extensions of the SM [14, 15]. At low energies (far below the electroweak scale), these HPs exclusively couple with the SM sector via a kinetic mixing with ordinary photons [16] and the effective Lagrangian can be written as follows,

$$-\mathcal{L} = \frac{1}{4}(A_{\mu\nu}A^{\mu\nu} + X_{\mu\nu}X^{\mu\nu}) + \frac{m_{\tilde{\gamma}}^2}{2}X_{\mu}X^{\mu} + \frac{\chi}{2}A_{\mu\nu}X^{\mu\nu} + J_{\mu}A^{\mu}. \quad (2.1)$$

^a For consistency, we use the term Hidden Photon (denoted by $\tilde{\gamma}$) throughout this thesis.

The term in brackets is a kinetic term for the gauge fields A and X , where $A_{\mu\nu} = \partial_\mu A_\nu - \partial_\nu A_\mu$ and $X_{\mu\nu} = \partial_\mu X_\nu - \partial_\nu X_\mu$ denote the visible and hidden field-strength tensors, respectively. $m_{\tilde{\gamma}}$ and χ , both free parameters, represent the mass of the HPs and their kinetic-mixing parameter with ordinary photons. Lastly, J^μ is the ordinary charge current. Let us note that here and for the rest of this chapter, we choose the metric convention $(+, -, -, -)$ and employ natural units $\hbar = c = \epsilon_0 = 1$.

On the $m_{\tilde{\gamma}}$ -axis, experimental searches are spanning a huge range of masses from 10^{-20} eV up to 10^{12} eV, and providing a rich phenomenology beyond the SM [17]. On the χ -axis, predicted sizes of the mixing parameter, in particular from string theory, spread from 10^{-3} to as low as 10^{-17} , although with no clear minimum [14, 19]. Interestingly, it has also been argued recently that HPs produced with a non-thermal mechanism in the early universe, can survive as cold Dark Matter (DM) till present [18, 19, 23]. The resulting phase space is considerable and promotes lower mass DM ($\lesssim 1$ MeV), thus requiring to explore new search strategies. Let us also stress that this is different from the usual picture where heavy HPs only mediate the interaction to a hidden sector, which then contains a generic fermionic DM. Here, the DM candidate is the gauge boson.

This chapter is structured as follows. In Section 2.1, we examine the phenomenological implication of the kinetic mixing and review existing constraints from laboratory experiments and astrophysical observations of HP as Weakly Interacting Slim Particles (WISPs). In Section 2.2, we revisit the modifications of Maxwell's equations introduced by the Lagrangian (2.1) and derive the field solutions. In Section 2.3, we discuss HPs in the context of cold DM particles and describe the existing direct searches in this direction. And in Section 2.4, we introduce the technique used at the FUNK experiment to search for Hidden-Photon Dark Matter (HPDM).

2.1 General picture

To begin with, we note that this section aims at summarizing the exhaustive reviews in [14, 17], on the quest for HPs, and references there-in.

2.1.1 Propagation and Interaction eigenstates

There are essentially two ways to understand the kinetic mixing of tensor fields appearing in Eq. (2.1). Both ways lead to different phenomenological interpretations of the mixing, but physically equivalent. In some sense, these can be achieved by means of suitable field redefinitions which are explained below. In the next section, we will explicitly diagonalize the Lagrangian so that these pictures emerge naturally.

Propagation or Mass eigenstates

Applying the transformation $A^\mu \rightarrow A^\mu - \chi X^\mu$ and keeping terms of $\mathcal{O}(\chi)$, Eq. (2.1) becomes

$$-\mathcal{L} = \frac{1}{4}(A_{\mu\nu}A^{\mu\nu} + X_{\mu\nu}X^{\mu\nu}) + \frac{m_\gamma^2}{2}X_\mu X^\mu + J_\mu(A^\mu - \chi X^\mu), \quad (2.2)$$

where we have successfully removed the kinetic mixing term and diagonalized the Lagrangian in the new (A^μ, X^μ) basis. In this basis, we identify a *massless* and a *massive* photon eigenstates, which propagate independently. The coupling of HP to ordinary matter is achieved with the last term of Eq. (2.2), $\chi J_\mu X^\mu$. In this picture, charge particles then acquire an additional hidden charge which is suppressed by the mixing-parameter value. This also provides us with number of ways to probe for HP signature, for example with precision measurement of modifications in Coulomb's law or also via their scattering with or decay into SM particles. We shall come back to that later.

Interaction or Flavor eigenstates

Likewise, under the transformation^b $X^\mu \rightarrow X^\mu - \chi A^\mu$, the first order Lagrangian becomes

$$-\mathcal{L} = \frac{1}{4}(A_{\mu\nu}A^{\mu\nu} + X_{\mu\nu}X^{\mu\nu}) + \frac{m_\gamma^2}{2}(X_\mu X^\mu - 2\chi A_\mu X^\mu) + J_\mu A^\mu. \quad (2.3)$$

^b Rotating from mass to flavor eigenstates can be achieved with $A = A' - \chi X'$ and $X = X' + \chi A'$.

In this picture, the SM particles remain uncharged under X . Rather, the non-trivial off-diagonal mass term $\propto A_\mu X^\mu$ allows oscillation between the HP and ordinary photon eigenstates. In analogy to neutrino oscillation, we may also talk about *active* and *sterile* photon. Hence this basis is called interaction basis. The various detection techniques aim at either constraining or observing a flux of HP-to-photon conversion. The FUNK experiment pursues this road.

2.1.2 Indirect and Direct constraints

In Fig. 2.1, we present the global spectrum of indirect and direct searches for HPs, stretching over several orders of magnitude in mass. Outside the phase space labeled "Cold Dark Matter", which we discuss in Section 2.3.1, HPs are not required to be component of the DM. All other colored regions indicate disfavored parameter space for HPs. Each of these constraints may appear more transparent in one or the other picture of the kinetic mixing described above. We briefly describe them below.

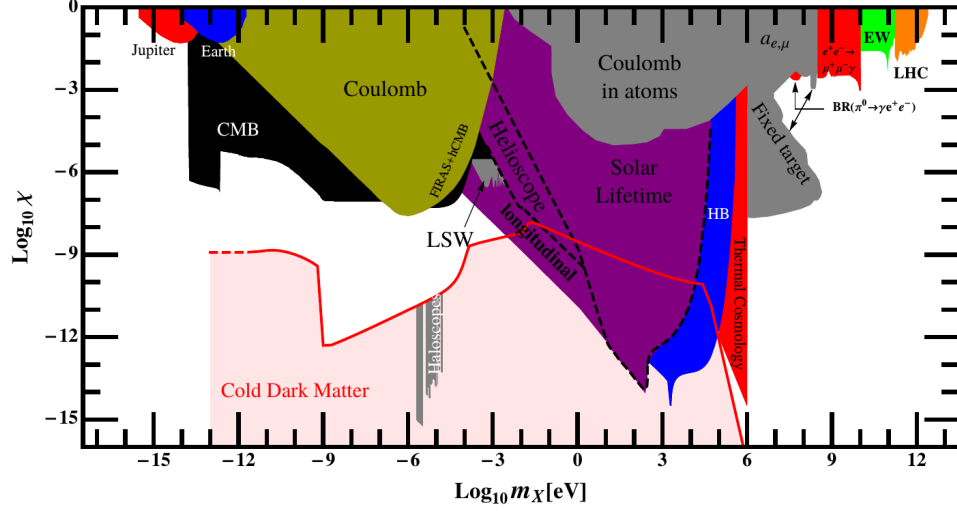


Figure 2.1: Overview of the theoretical and experimental efforts in the search of HP particles in the last decades. The figure was taken from [17] and is not up-to-date.

Astrophysical and cosmological bounds

- **Large-scale magnetic field**
As we will develop in Section 2.2, the presence of HPs modifies the usual Maxwell's equations. In particular, they provide a source term for an additional magnetic field which can be tested at large scale. The non-observation of unexplained anomalies in the static magnetic fields of "Earth" and "Jupiter" [24, 25] have been used to constrain HPs with very low masses.
- **Energy loss of stars**
In the interior of hot and dense stars, HPs can be produced resonantly and escape to the surface unimpeded [26]. Such a mechanism can rapidly accelerate the energy loss of stars and thus changes the course of stellar evolution. Furthermore, contribution from "longitudinal" oscillation mode in the plasma also enhances the HP production flux [27]. Thus, study of the "Solar lifetime", the cooling rate of horizontal branch ("HB") and red giant stars ("RG", not in Fig. 2.1) provides tight constraints on a large portion of the HP parameter space [28].
- **Cosmic Microwave Background (CMB)**
The strength of the HP-photon mixing within the primordial plasma can lead to some distortions in the CMB spectrum [29]. These distortions are strongly constrained from very precise measurements of the CMB. Additionally, consideration for the cosmological implication of a

thermal population of HPs in form of Warm DM [30] (labeled “thermal Cosmology”) and hidden CMB [31] (labeled “FIRAS + hCMB”) are also shown.

Laboratory experiments

- **Non-Coulomb force**
The hidden-charge acquired by ordinary matter modifies the Coulomb potential between two charged particles by introducing an exponential deviation, that becomes suppressed with the distance between the two particles [32]. Such a deviation can be tested in laboratory [33, 34] and has been used to constrain HP with masses in the (sub)- μeV and (sub)-keV ranges. These bounds are labeled “Coulomb” and “Coulomb in atoms” [35, 36].
- **Muon $g - 2$ anomaly**
Another first motivation for HPs was to resolve the observed $(g - 2)_\mu$ anomalous magnetic moment of muons [37]. The parameter space excluded by measurements of the magnetic moments of electrons and muons are labeled “ $a_{e,\mu}$ ”. Nevertheless, the hypothesis of HPs as explanation of the $(g - 2)_\mu$ was decisively ruled out by null results from measurements of the visible [38] and invisible [39, 40] decay channels of the HPs.
- **Scattering and Decay**
At high energies, HPs can be directly produced in scattering experiments with “fixed targets”, at colliders (“ $e^+e^- \rightarrow \mu^+\mu^-\tilde{\gamma}$ ”, “LHC”), or via the subsequent rare decay of the produced mesons (“ $\pi^0 \rightarrow \tilde{\gamma}e^+e^-$ ”) [41, 42]. The HPs can then decay into visible or invisible sectors. Hence these experiments search for either peaks in the invariant mass distribution or missing energy events. Alternatively, HPs can also be tested in electroweak precision (“EW”) measurements [43].
- **Light-Shinning through a Wall (“LSW”)**
At smaller masses, experimental techniques directly exploit the photon-to-HP oscillation. As their name suggests, these LSW experiments (e.g. [44, 45]) shine a laser onto a thick wall, opaque to ordinary photons. There is however a certain probability that these photons oscillate to HPs before the wall, traverse through and oscillate back to detectable photons after the wall, where a suitable detector is placed [46]. Moreover, the oscillation probability can be enhanced by employing tuned optical cavities in both sides of the wall [47]. From the length of the oscillation zone, the targeted mass range is typically in the meV range.

- **Helioscopes**
In connection with the energy loss of stars mentioned above, “Helioscopes” which were originally designed for the detection of solar axions [48], can also be used to probe HP production in the interior of the Sun. The idea resembles to the LSW experiments. HPs can be produced in the solar core, escape easily to the surface, propagate to Earth, and eventually oscillate back to ordinary photons inside the detector zone [26]. Here, the *wall* represents everything intervening between the HP-production site and the detector.
- **Haloscopes**
Haloscopes [49] are another type of photon-regeneration experiments, also primarily aimed for axion DM searches [50]. Here, the idea is similar to the LSW experiments, but instead, employing microwave cavities. A first emitter cavity is fed with microwave powers in the frequency mode of the cavity. This allows a resonant enhancement of the photon-to-HP oscillation probability. Then, the produced HPs can permeate through the cavity shielding and get picked-up in a second detector cavity, tuned to the same frequency, where they oscillate back to ordinary microwaves [51]. The current limit concerns masses $\lesssim 3 \mu\text{eV}$ (not shown in Fig. 2.1) and is comparable to the limits set by “Coulomb” and “CMB” around this region, but also offering promising prospects for the near future [52].
- **Radio telescopes**
At extremely low energies, the HP-photon mixing can be tested with conventional radio astronomy. Here, the basic idea is that the HP-photon oscillations can modulate the broadband spectra of astrophysical sources. The limit (not shown in Fig. 2.1) from a compilation of present and future radio observations are sensitive to strengths of the mixing parameter of $O(10^{-3})$ [53].

Besides these searches for WISPy HP, many experiments are also devoting efforts to search for HPDM. We will comment on them in Section 2.3.3.

2.2 HP-Photon mixing

After this brief overview on the general extent of the HP phenomenology, we are now going to have a close look at the consequences of the new kinetic mixing to our understanding of classical electromagnetism. In this section, we revisit the expressions of Maxwell’s equations in presence of an additional $U(1)$ symmetry and we find the propagating field solutions in vacuum. Then, we also include the matter effects.

2.2.1 Modified Maxwell's equations

Let us begin with the equations of motion which follow from Eq. (2.1). Using the Euler-Lagrange equations $\partial_\mu[\partial\mathcal{L}/\partial_\mu(\partial A^\beta)] = \partial\mathcal{L}/\partial A^\beta$ we have

$$\begin{aligned}\partial_\mu A^{\mu\nu} + \chi\partial_\mu X^{\mu\nu} &= J^\nu, \\ \chi\partial_\mu A^{\mu\nu} + \partial_\mu X^{\mu\nu} &= m_\gamma^2 X^\nu.\end{aligned}\quad (2.4)$$

Together with the geometrical properties of the tensor fields

$$\begin{aligned}\partial_\lambda A_{\mu\nu} + \partial_\mu A_{\nu\lambda} + \partial_\nu A_{\lambda\mu} &= 0, \\ \partial_\lambda X_{\mu\nu} + \partial_\mu X_{\nu\lambda} + \partial_\nu X_{\lambda\mu} &= 0,\end{aligned}\quad (2.5)$$

these equations generalize the laws of electromagnetism in presence of an additional $U(1)$ gauge group kinetically mixed with the SM $U(1)$. With a suitable gauge choice, we can solve for the gauge fields A and X .

To get familiar with these equations, let us write them explicitly in terms of the electromagnetic fields \mathbf{E} , $\hat{\mathbf{E}}$, \mathbf{B} , $\hat{\mathbf{B}}$, where we use the hat-notation for hidden fields. With our metric convention, the structures of the field tensors are given by

$$\begin{aligned}A^{0i} &= -E^i, & A^{ij} &= -\epsilon^{ijk} B_k, \\ X^{0i} &= -\hat{E}^i, & X^{ij} &= -\epsilon^{ijk} \hat{B}_k,\end{aligned}\quad (2.6)$$

where $i = 1, 2, 3$ and ϵ^{ijk} is the Levi-Civita symbol. Expanding Eq. (2.4) along its 0th and i th components, we obtain

$$\begin{aligned}\nabla \cdot (\mathbf{E} + \chi\hat{\mathbf{E}}) &= \rho, \\ \nabla \cdot (\chi\mathbf{E} + \hat{\mathbf{E}}) &= -m_\gamma^2 X^0, \\ \nabla \times (\mathbf{B} + \chi\hat{\mathbf{B}}) &= \mathbf{J} + \frac{\partial}{\partial t}(\mathbf{E} + \chi\hat{\mathbf{E}}), \\ \nabla \times (\chi\mathbf{B} + \hat{\mathbf{B}}) &= -m_\gamma^2 \mathbf{X} + \frac{\partial}{\partial t}(\chi\mathbf{E} + \hat{\mathbf{E}}),\end{aligned}\quad (2.7)$$

where we have written $A^\mu = (A^0, \mathbf{A})$, $X^\mu = (X^0, \mathbf{X})$ and $J^\mu = (\rho, \mathbf{J})$ in terms of the electric potentials A^0, X^0 , the vector potentials \mathbf{A}, \mathbf{X} , the ordinary charge density ρ and the ordinary current density \mathbf{J} . Likewise, Eq. (2.5) gives the usual homogeneous equations

$$\begin{aligned}\nabla \cdot \mathbf{B} &= 0, \\ \nabla \times \mathbf{E} &= -\frac{\partial \mathbf{B}}{\partial t}, \\ \nabla \cdot \hat{\mathbf{B}} &= 0, \\ \nabla \times \hat{\mathbf{B}} &= -\frac{\partial \hat{\mathbf{B}}}{\partial t}.\end{aligned}\quad (2.8)$$

It is trivial to verify that these equations correctly reproduce the standard Maxwell's equations when we turn off the kinetic mixing ($\chi \rightarrow 0$).

2.2.2 Propagation in vacuum

First, we consider motion in free space, i.e. $\rho = 0$ and $\mathbf{J} = \mathbf{0}$. We choose a Lorenz gauge^c such that $\partial_\mu A^\mu = 0 = \partial_\mu X^\mu$ with $A_0 = 0 = X_0$. The equations of propagation can be obtained following classical procedure in electromagnetism. Using the identity $\nabla(\nabla \cdot \mathbf{V}) = \nabla^2 \mathbf{V} + \nabla \times (\nabla \times \mathbf{V})$, we have

^c For the field X , there is no gauge freedom because of the mass term. However, the condition is enforced by Eq. (2.4). This can be seen by taking the gradient of the second equation.

$$\begin{aligned} \nabla(\nabla \cdot (\mathbf{E} + \chi \hat{\mathbf{E}})) &= \nabla^2(\mathbf{E} + \chi \hat{\mathbf{E}}) - \nabla \times (\partial_t \mathbf{B} + \chi \partial_t \hat{\mathbf{B}}) \\ &= \nabla^2(\mathbf{E} + \chi \hat{\mathbf{E}}) - \partial_t^2(\mathbf{E} + \chi \hat{\mathbf{E}}) \\ &= 0. \end{aligned} \quad (2.9)$$

Similarly for the second equation. It follows

$$\begin{aligned} \partial^2(\mathbf{E} + \chi \hat{\mathbf{E}}) &= 0, \\ \partial^2(\chi \mathbf{E} + \hat{\mathbf{E}}) + m_{\tilde{\gamma}}^2 \hat{\mathbf{E}} &= 0, \end{aligned} \quad (2.10)$$

where we use a shorthand $\partial^2 = \partial_t^2 - \nabla^2$. Let us look for plane wave solutions $\propto e^{i(\omega t - \mathbf{k} \cdot \mathbf{x})}$. The operator ∂^2 brings down a term $k^2 - \omega^2$. The two non-trivial solutions to Eq. (2.10) correspond to the eigenfrequencies $\omega^2 = k^2$ and $\omega^2 = p^2 + m_{\tilde{\gamma}}^2$ associated to the eigenvectors $(1, 0)$ and $(-\chi, 1)$. The general solution is given thus by

$$\begin{pmatrix} \mathbf{E} \\ \hat{\mathbf{E}} \end{pmatrix} = \mathbf{E}_m \begin{pmatrix} 1 \\ 0 \end{pmatrix} e^{i(\omega t - \mathbf{k} \cdot \mathbf{x})} + \hat{\mathbf{E}}_m \begin{pmatrix} -\chi \\ 1 \end{pmatrix} e^{i(\omega t - \mathbf{p} \cdot \mathbf{x})}, \quad (2.11)$$

where \mathbf{E}_m and $\hat{\mathbf{E}}_m$ denote complex amplitudes. The first term is simply an ordinary propagating electromagnetic wave. The second term is a matter wave associated to a particle of mass $m_{\tilde{\gamma}}$. It is this last bit that forms our DM solution. We shall come back to this point in Section 2.3.

2.2.3 Propagation in matter

Maxwell's equations

Let us now turn to the effect of matter on the kinetic mixing. It is convenient to rearrange Eq. (2.7) as follows,

$$\begin{aligned} \nabla \cdot \mathbf{E} &= \rho + \chi m_{\tilde{\gamma}} X^0, \\ \nabla \times \mathbf{B} &= \partial_t \mathbf{E} + \mathbf{J} + \chi m_{\tilde{\gamma}}^2 \mathbf{X}, \\ \nabla \cdot \hat{\mathbf{E}} &= -m_{\tilde{\gamma}}^2 X^0 - \chi \rho, \\ \nabla \times \hat{\mathbf{B}} &= \partial_t \hat{\mathbf{E}} - m_{\tilde{\gamma}}^2 \mathbf{X} - \chi \mathbf{J}, \end{aligned} \quad (2.12)$$

where we only kept terms of $\mathcal{O}(\chi)$. We follow again standard treatments in electrodynamics and being inspired by the development of axion electrodynamics for dielectric haloscopes [54]. We want to find a suitable formulation for Eq. (2.12) in linear dielectric media and are interested in plane wave solutions propagating in a such background. Let us notice that the homogeneous Eqs. (2.8) remain unaffected since they result from inherent properties of the field tensors.

To account for the electromagnetic response of the medium, we first split its charge and current densities into their free (ρ_f, \mathbf{J}_f) and bound (ρ_b, \mathbf{J}_b) components. In presence of an electric field \mathbf{E} , the dielectric medium responds by a macroscopic polarization \mathbf{P} . This is because of the local displacement of bound charges along the direction of the \mathbf{E} -field, resulting in formation of microscopic dipoles. The medium polarization is connected to the bound-charge density such that $\rho_b = -\nabla \cdot \mathbf{P}$. Furthermore, the material medium itself exhibits a macroscopic magnetization \mathbf{M} , which is due to the microscopic magnetic moments linked to the spin and angular momentum of electrons. Hence, the bound-current density is the sum of two currents such that $\mathbf{J}_b = \nabla \times \mathbf{M} + \partial_t \mathbf{P}$.

We also introduce the usual auxiliary fields defined as

$$\begin{aligned}\mathbf{D} &= \mathbf{E} + \mathbf{P}, \\ \mathbf{H} &= \mathbf{B} - \mathbf{M},\end{aligned}\tag{2.13}$$

where \mathbf{D} represents the macroscopic electric-displacement field and \mathbf{H} is the macroscopic magnetic field. Considering a propagating medium with linear response^d, the polarization and magnetization vectors are given by $\mathbf{P} = \kappa_e \mathbf{E}$ and $\mathbf{M} = \kappa_m \mathbf{H}$. The coefficients κ_e and κ_m are called electric and magnetic susceptibility of the medium, respectively. For such a medium, Eqs. (2.13) reduce to $\mathbf{D} = (1 + \kappa_e)\mathbf{E}$ and $\mathbf{H} = \mathbf{B}/(1 + \kappa_m)$.

^d That is the case for homogeneous and non-dispersive media

Using these definitions, we can rewrite Eq. (2.12) for the electric field as

$$\begin{aligned}\nabla \cdot \mathbf{E} &= \nabla \cdot \mathbf{D} - \nabla \cdot \mathbf{P} \\ &= \rho_f + \rho_b + \chi m_{\tilde{\gamma}}^2 X^0,\end{aligned}\tag{2.14}$$

and the magnetic field as

$$\begin{aligned}\nabla \times \mathbf{B} &= \nabla \times \mathbf{H} + \nabla \times \mathbf{M} \\ &= \partial_t \mathbf{D} - \partial_t \mathbf{P} + \mathbf{J}_f + \mathbf{J}_b + \chi m_{\tilde{\gamma}}^2 \mathbf{X},\end{aligned}\tag{2.15}$$

where $\rho_f = \rho - \rho_b$ and $\mathbf{J}_f = \mathbf{J} - \mathbf{J}_b$ are the free charge and current densities, respectively^e. These lead to the equations of motion for the auxiliary fields

$$\nabla \cdot \mathbf{D} - \rho_f = \chi m_{\tilde{\gamma}}^2 X^0, \tag{2.16}$$

$$\nabla \times \mathbf{H} - \partial_t \mathbf{D} - \mathbf{J}_f = \chi m_{\tilde{\gamma}}^2 \mathbf{X}. \tag{2.17}$$

^e For a perfect dielectric, we have $\rho_f = 0$ and $\mathbf{J}_f = \mathbf{0}$

Let us notice once again that these are the usual macroscopic formulations of the Maxwell's equations in linear media, when we turn off the kinetic mixing.

It is now convenient to express them in terms of quantities which directly characterize the electromagnetic response of the background medium. For a non-perfect dielectric medium with conductivity σ_e , the free-current density is given by Ohm's law, such that $\mathbf{J}_f = \sigma_e \mathbf{E}$. Taking the time derivative of both sides of Eq. (2.16), we have

$$\begin{aligned}\nabla \cdot \partial_t \mathbf{D} - \partial_t \rho_f &= (1 + \kappa_e) \nabla \cdot \partial_t \mathbf{E} + \nabla \cdot \mathbf{J}_f \\ &= (1 + \kappa_e) \nabla \cdot i\omega \mathbf{E} + \nabla \cdot \sigma_e \mathbf{E} \\ &= i\omega(1 + \kappa_e - i\sigma_e/\omega) \nabla \cdot \mathbf{E} = i\omega \chi m_{\tilde{\gamma}}^2 \mathbf{X}.\end{aligned}\quad (2.18)$$

In the first line, we used the continuity equation $\partial_\mu J_f^\mu = \partial_t \rho_f + \nabla \cdot \mathbf{J}_f = 0$. The next steps follow from our plane wave ansatz. Focusing now on Eq. (2.17), we note that $\partial_t \mathbf{D} + \mathbf{J}_f = (1 + \kappa_e) \partial_t \mathbf{E} + \sigma_e \mathbf{E} = (1 + \kappa_e - i\sigma_e/\omega) \partial_t \mathbf{E}$.

Summarizing, the field equations in matter can be expressed as follows,

$$\begin{aligned}\epsilon \nabla \cdot \mathbf{E} &= \chi m_{\tilde{\gamma}}^2 X^0, \\ \nabla \times \mathbf{H} - \epsilon \partial_t \mathbf{E} &= \chi m_{\tilde{\gamma}}^2 \mathbf{X}, \\ \nabla \cdot \hat{\mathbf{E}} + m_{\tilde{\gamma}}^2 X^0 &= -\chi \rho, \\ \nabla \times \hat{\mathbf{B}} - \partial_t \hat{\mathbf{E}} + m_{\tilde{\gamma}}^2 \mathbf{X} &= -\chi \mathbf{J},\end{aligned}\quad (2.19)$$

which are completed by the homogeneous Eqs. (2.8) and with the constitutive relations for a linear medium characterized by (ϵ, μ) , such that

$$\begin{aligned}\mathbf{D} &= \epsilon \mathbf{E} = (1 + \kappa_e - i\sigma_e/\omega) \mathbf{E}, \\ \mathbf{H} &= \frac{\mathbf{B}}{\mu} = \frac{\mathbf{B}}{1 + \kappa_m}.\end{aligned}\quad (2.20)$$

ϵ and μ encode the electric permittivity and magnetic permeability of the medium. $n^2 = \epsilon \mu$ represents its refractive index. From Eq. (2.19), it is clear that the presence of matter does affect the propagation of the hidden fields. This can be accounted for by introducing an effective mixing.

Propagation equations

We are now ready to derive the equations of propagation of the electric fields in matter. We begin with the ordinary field. This is done by computing

$$\begin{aligned}\nabla(\nabla \cdot \mathbf{E}) &= \nabla^2 \mathbf{E} + \nabla \times (\nabla \times \mathbf{E}) \\ &= \nabla^2 \mathbf{E} - \mu \partial_t (\nabla \times \mathbf{H}) \\ &= \nabla^2 \mathbf{E} - \mu \epsilon \partial_t^2 \mathbf{E} - \mu \chi m_{\tilde{\gamma}}^2 \partial_t \mathbf{X} = \epsilon^{-1} \chi m_{\tilde{\gamma}}^2 \partial_t X^0.\end{aligned}\quad (2.21)$$

In a similar fashion, for the hidden field we have

$$\nabla^2 \hat{\mathbf{E}} - \partial_t^2 \hat{\mathbf{E}} + m_{\tilde{\gamma}}^2 \partial_t \mathbf{X} + \chi \partial_t \mathbf{J} = -m_{\tilde{\gamma}}^2 \nabla X^0 - \chi \nabla \rho. \quad (2.22)$$

In the last equation, the terms which contain the charge and current density can be written in terms of the vector fields, by using the first two equations in (2.12) such that

$$\partial_t \mathbf{J} + \nabla \rho = -(\partial_t^2 \mathbf{E} - \nabla^2 \mathbf{E}) - \chi m^2 (\partial_t \mathbf{X} + \nabla X^0). \quad (2.23)$$

Finally, rearranging Eqs. (2.21) and (2.22) and keeping terms of $\mathcal{O}(\chi)$, we obtain

$$\begin{aligned} (n^2 \partial_t^2 - \nabla^2) \mathbf{E}^2 &= -\chi m_{\tilde{\gamma}}^2 (\mu \partial_t \mathbf{X} + \epsilon^{-1} \nabla X^0), \\ \chi (\partial_t^2 - \nabla^2) \mathbf{E} + (\partial_t^2 - \nabla^2) \hat{\mathbf{E}} &= m_{\tilde{\gamma}}^2 (\partial_t \mathbf{X} + \nabla X^0). \end{aligned} \quad (2.24)$$

These two equations describe the propagation of the (hidden) electric fields inside an homogeneous and non-dispersive medium. In what follows, we also suppose that the medium of interest is non-permeable, i.e. $\mu \approx \mu_0 = 1$ and $n^2 = \epsilon$.

Field solutions

Following the same consideration as in the vacuum case, we work in Lorenz gauge with $A^0 = 0 = X^0$ and look for plane wave solutions. Eq. (2.24) becomes

$$\begin{bmatrix} k^2 - n^2 \omega^2 & -\chi m_{\tilde{\gamma}}^2 \\ \chi(k^2 - \omega^2) & k^2 - \omega^2 + m_{\tilde{\gamma}}^2 \end{bmatrix} \begin{pmatrix} \mathbf{E}_m \\ \hat{\mathbf{E}}_m \end{pmatrix} = 0, \quad (2.25)$$

where \mathbf{E}_m and $\hat{\mathbf{E}}_m$ denote complex amplitudes. Finding non-trivial solutions requires the determinant of the above matrix to be 0. The general solution is given by

$$\begin{pmatrix} \mathbf{E} \\ \hat{\mathbf{E}} \end{pmatrix} = \mathbf{E}_m \begin{pmatrix} 1 \\ \chi^{\text{eff}} - \chi \end{pmatrix} e^{i(\omega t - \mathbf{k} \cdot \mathbf{x})} + \hat{\mathbf{E}}_m \begin{pmatrix} -\chi^{\text{eff}} \\ 1 \end{pmatrix} e^{i(\omega t - \mathbf{p} \cdot \mathbf{x})}, \quad (2.26)$$

with the eigenstates

$$k^2 = n^2 \omega^2 \quad \text{and} \quad p^2 = \omega^2 - m_{\tilde{\gamma}}^2, \quad (2.27)$$

and the effective kinetic mixing in matter defined as

$$\chi^{\text{eff}} = \chi \frac{m_{\tilde{\gamma}}^2}{m_{\tilde{\gamma}}^2 + (n^2 - 1)\omega^2}. \quad (2.28)$$

For consistency check, let us remark that we reproduce the results in vacuum when $n = 1$.

2.3 Hidden-Photon Dark Matter

2.3.1 Production and Parameter space

Up to now, we essentially considered the implications of an additional $U(1)$ symmetry to the SM and how we could detect the new gauge boson as WISPs. If such a symmetry is indeed present in nature, it is only natural to also ask if these HPs could be good candidates for DM while not spoiling cosmological observations.

HPs from thermal freeze-out

Consideration of a thermal population of HPDM principally rules out heavy masses ($\gtrsim 1$ MeV) and firmly constrains the possibility of a *warm* population (keV–MeV) [30]. Moreover, HP relic with lighter masses and realized from the freeze-out mechanism would constitute a *hot* population, which are not compatible with large structure formation, if they are predominant, since they can prevent gravitational clumps.

Nonetheless, relativistic HPs with meV masses can be produced after Big Bang Nucleosynthesis (BBN) but before CMB decoupling, and contribute to the standard picture of Big Bang in forms of dark radiation [31]. In this context, they are constrained from the measurement of the effective number of neutrino species and baryon-to-photon ratio at the time of decoupling. These HPs would also leave an imprint of hidden CMB in the cosmos and possibly distort the measured CMB spectrum. That gives the bound labeled “FIRAS + hCMB” in Fig. 2.1.

Thermal HPDM are produced via resonant conversion of photons in the primeval plasma, at a certain temperature. The main production channels are $\gamma e^\pm \rightarrow \tilde{\gamma} e^\pm$, $e^+e^- \rightarrow \tilde{\gamma}$, and $e^+e^- \rightarrow \gamma\tilde{\gamma}$. The production efficiency depends on the effective mixing^f in Eq. (2.28). In turns, this can be used to constrain the HP phase space to the observed relic abundance of DM, in order to avoid overproduction.

^f This relates to the temperature and frequency of the plasma [26].

The next issue concerns their cosmological stability. As the universe cools down, the kinetic mixing $\chi_{\text{eff}} \sim \chi$ still allows HPs to decay into SM particles^g. Requiring a viable DM with lifetime of the order of the age of the universe strongly constrains the decay rate and thus the mixing. The sharp cut-off from the “Thermal Cosmology” bound in Fig. 2.1 correspond to the energy threshold for $\tilde{\gamma} \rightarrow e^+e^-$. For $m_{\tilde{\gamma}} \geq 2m_e$, this is the dominant decay channel. The decay epoch is somewhat less relevant for the course of BBN and CMB. In that sense, constraints are quite loose for decaying heavy HPs.

^g HPs are example of decaying DM.

For $m_{\tilde{\gamma}} < 2m_e$, HPs can be cosmologically stable although they still can decay via $\tilde{\gamma} \rightarrow 3\gamma$, at loop level, with a relatively suppressed decay

rate. These photons would then contribute to the intergalactic diffuse photon background. Demanding that the gamma ray flux from decaying HPs should not exceed the observed background disfavors HPDM with masses $m_{\tilde{\gamma}} \gtrsim 100$ keV.

On the other side, HPs with masses $m_{\tilde{\gamma}} \lesssim 100$ keV are light enough to be produced via resonant oscillation inside the hot and dense environment of stars, thereby providing an efficient cooling mechanism for the stars. However, observations of stellar evolution put strong bounds on the mixing parameter (see labels ‘‘Solar lifetime’’ and ‘‘HB’’ in Fig. 2.1), essentially discarding all parameter space below 100 keV, where thermal HPDM are viable.

The conclusion of [30] is that HPDM, produced solely through thermal kinetic mixing, cannot be the predominant component of DM if they are warm, and fundamentally excluded if they are cold.

HPs from the misalignment mechanism

The essence of WISPy Cold DM lies in the fact that they have to be produced non-thermally in the early universe. One way to realize that is the misalignment mechanism, usually invoked for axions (see e.g. [19]). Recently, it has been argued in [18] that the same mechanism can be also used to produce extremely cold HPDM. We summarize the idea below.

To understand the idea, let us first briefly review the misalignment mechanism in the context of a scalar field in an expanding universe. The equation of motion for a massive scalar field ψ with the Lagrangian $L_\psi = \partial_\mu \psi \partial^\mu \psi / 2 - m_\psi^2 \psi^2 / 2$, in curved space with metric g , is given by

$$\frac{1}{\sqrt{-g}} \partial_\mu (\sqrt{-g} g^{\mu\nu} \partial_\nu \psi) + m_\psi^2 \psi = 0. \quad (2.29)$$

For an homogeneous field ($\partial_i \psi = 0$) in the Friedmann–Lemaître–Robertson universe whose signature is $g_{\mu\nu} = \text{diag}(1, -a^2(t)\delta_{ij})$, the above equation reduces to

$$\ddot{\psi} + 3H\dot{\psi} + m_\psi^2 \psi = 0, \quad (2.30)$$

where $H = \dot{a}/a$ is the Hubble rate. The energy-momentum tensor of this scalar field describes a perfect fluid with energy density ρ_ψ and pressure p_ψ , given by [55]

$$\begin{aligned} \rho_\psi &= \frac{1}{2} \dot{\psi}^2 + \frac{1}{2} m_\psi^2 \psi^2, \\ p_\psi &= \frac{1}{2} \dot{\psi}^2 - \frac{1}{2} m_\psi^2 \psi^2, \end{aligned}$$

respectively. Eq. (2.30) evokes a damped harmonic oscillator where the friction depends on the expansion rate of the universe and the frequency on the mass of the scalar field. We can characterize its solution as function of the evolution of the discriminant $9H^2 - 4m_\psi^2$.

At early times ($H \gg m_\psi$), the oscillator is overdamped and the field is stuck at its initial value. As the universe expands and this discriminant becomes negative, the field begins to roll down to its minimum value and undergoes oscillations. At later times ($H \ll m_\psi$), the solution is close to an undamped oscillator with frequency m_ψ . Therefore, we are left with an homogeneous scalar field with average energy density $\langle \rho_\psi \rangle = \langle m_\psi^2 \psi^2 \rangle$ and pressure $\langle p \rangle = 0$. This is precisely the behavior of non-relativistic matter. For the misalignment mechanism, the important bit is that the field picks up some random non-vanishing initial value. Then, an eventual inflationary scenario would generally smooth-out the field value at every point in space, and produce a *nearly* homogeneous field which would behave like a very cold boson-condensate, today.

The crucial realization in [18] was to show that the same mechanism can also be applied to a massive vector field X . In this case, after a fortuitous episode of inflation, each of the spatial components X^i of the vector field evolves according to Eq. (2.30). After some weakly damped oscillations, this scenario eventually leads to a population of (extremely) cold HPs. In order to be a viable DM candidate, this population needs to allow large structure formation and eventually survives through all cosmological evolutions.

For the consideration in [18], the allowed parameter space of HPDM is obtained by preventing the HPs to decay on timescale shorter than the age of the universe and by constraining thermalization process such as $\tilde{\gamma}e^\pm \leftrightarrow \gamma e^\pm$ in the primordial plasma. At higher masses, the constraints from HP decay are much stronger and require $m_{\tilde{\gamma}} < 2m_e$. The context is similar to the case of thermal HPDM, discussed previously. In principle, there is also a lower bound for the mass, $m_{\tilde{\gamma}} \gtrsim 10^{-24}$ eV, which mainly comes from arguments on structure formation. Lastly, reproducing the right abundance of relic DM essentially depends on the initial value of the field.

This idea for the production of HPDM was reconsidered [19]. In particular, the allowed parameter space has been considerably improved by accounting for resonant effects which affect thermalization processes in the plasma and by including bounds from the effective number of neutrino species and the inferred baryon-to-photon ratio from BBN and CMB, thus clarifying the role of HPs in the early universe. The definite parameter space corresponds to the region labeled “Cold Dark Matter” in Fig. 2.1. Finally, it is worth to note that there exists other mechanism which can generate sufficiently cold population of HP and mimic DM [23].

2.3.2 HPDM condensate

As the universe temperature decreases, χ_{eff} relaxes to its *vacuum* value χ . In this course, the first combination of field solutions in Eq. (2.26) simply describes the propagating eigenstate of ordinary photons. It is the second combination of fields,

$$\hat{\mathbf{E}}_m \begin{pmatrix} -\chi_{\text{eff}} \\ 1 \end{pmatrix} e^{i(\omega t - \mathbf{p} \cdot \mathbf{x})}, \quad (2.31)$$

that can form a condensate at early times and survive as cold DM till present [19]. This is our DM solution. With the small kinetic mixing, the DM field is mostly hidden. However, it also carries a minuscule but ordinary oscillating electric field. This particular signature can later be exploited to search for unambiguous evidences of the presence of HPDM.

In this case, the de Broglie wave-vector \mathbf{p} and angular frequency ω of the field solution are given by the momentum and energy of the local DM relic, such that

$$\mathbf{p} = m_{\tilde{\gamma}} \mathbf{v}_{\text{DM}}, \quad (2.32)$$

$$\omega = m_{\tilde{\gamma}} [1 + \mathcal{O}(v_{\text{DM}}^2)], \quad (2.33)$$

where $|\mathbf{v}_{\text{DM}}| = v_{\text{DM}} \simeq 10^{-3}$ is the average velocity of galactic cold DM. More explicitly, the DM field oscillates at a frequency

$$\nu = 240 \text{ Hz} \left(\frac{m_{\tilde{\gamma}}}{\text{eV}} \right). \quad (2.34)$$

On the other hand, the energy density stored in the HP electromagnetic field is given by

$$\begin{aligned} \rho_{\text{HP}} &= \frac{1}{2} (|\hat{\mathbf{E}}|^2 + |\hat{\mathbf{B}}|^2) + \frac{m_{\tilde{\gamma}}^2}{2} |\mathbf{X}^2| \\ &= \frac{1}{2} |\hat{\mathbf{E}}|^2 \left(1 + \frac{p^2}{\omega^2} \right) + \frac{m_{\tilde{\gamma}}^2}{2\omega^2} |\hat{\mathbf{E}}|^2 \\ &= \frac{|\hat{\mathbf{E}}_m|^2}{2} + \mathcal{O}(v_{\text{DM}}^2). \end{aligned} \quad (2.35)$$

We recall that for plane waves, $\hat{\mathbf{B}} = -(\mathbf{k} \times \hat{\mathbf{E}})/\omega$ and $\mathbf{X} = i\hat{\mathbf{E}}/\omega$. Furthermore in the last step, we averaged the field amplitude over time, which gives a factor of 1/2.

If we now assume that HPs make up the whole DM present in the galactic halo and whose density is $\rho_{\text{CDM}} = 0.3 \text{ GeV cm}^{-3}$, then this fixes the energy density in the HP field such that $\rho_{\text{HP}} \equiv \rho_{\text{CDM}}$. It is convenient to write this

condition in terms of $|\mathbf{E}_{\text{DM}}| = \chi|\hat{\mathbf{E}}_m|$, which represents the amplitude of the *visible* DM field in vacuum, according to Eq. (2.31). Hence,

$$\rho_{\text{HP}} = \frac{\langle |\mathbf{E}_{\text{DM}}|^2 \rangle}{2\chi^2} = \rho_{\text{CDM}}, \quad (2.36)$$

where we also averaged over possible random pointing directions of \mathbf{E}_{DM} . It could also be assumed that the HP field is homogeneous and has an uniform direction in space after inflation. Then, if this direction is not affected by gravitational clumping during structure formation, the HPs would have the same pointing direction today, over a sufficiently large region of space [19].

2.3.3 Laboratory searches

In Section 2.1.2, we briefly explored the rich phenomenological implications of the existence of HPs in nature. These considerations do not demand a DM candidate. In recent years, many progresses have also been made to constrain the parameter space allowing HPs to be cold DM. Below, we summarize the different direct-detection techniques currently available and being used to search for evidences of HPDM.

- **HP absorption in WIMPs detector**
Current direct detection experiments of DM, which are optimized to low mass WIMPs, are also sensitive to (sub)-MeV and (sub)-keV HPs. Like ordinary photons, HPs can be absorbed in the bulk material of these detectors and produce an ionization signal. The absorption coefficient is analogue to the usual photoelectric effect but of the size of the hidden charge χe of electrons [56]. Bounds coming from these experiments are extremely competitive, with some already surpassing conventional astrophysical bounds [57–59].
- **Cavity haloscopes**
The general principles of (axion) DM haloscopes were already explained in Section 2.1.2. The only difference now is that we do not need an emitter cavity^h. The HPs are already present in the form of cold DM filling homogeneously the detector cavity. Thus in principle, we simply need slowly tune the cavity mode to the driving HP frequency and obtain a resonant signal. On the other-hand, the HPs do not need the magnetic field used in these experiments to couple axions to ordinary photons. As such, the results from current axion searches can be essentially used — with suitable replacements of the effective axion coupling and some geometrical factors — to constrain possible HP signal [19]. Bounds obtained with this approach turn to be very stringent for μeV HPs (labeled “Haloscopes” in Fig. 2.1).

^h This also means that the expected power is $\propto \chi^2$, while it is $\propto \chi^4$ in the LSW fashion.

- **Dish antenna**
This is the road taken by the FUNK experiment. The details of the technique are explained in the next section. In brief, the idea consists of employing a metallic mirror, with a good spherical shape. At the conducting surface of this mirror, HPs can be *converted* to visible photons, which then get focused at its center curvature. This technique presents a certain number of advantages, but most importantly, it is a broadband approach, i.e. we do not need to tune the setup for each specific HP mass. In addition, it is feasible to probe on different regions of the HP parameter space with essentially the same setup. As evidence, competitive limits were recently obtained in the eV [21, 22, 60, 61], meV [62], and μeV [21, 63] mass ranges.
- **Dielectric haloscopes**
These are new generation of detectors, still under development, and will complement traditional cavity experiments by targeting axions and HP in the sub-meV range [64]. For the case of HPs, the projected sensitivity goes down to an unprecedented limit of $\chi \sim 10^{-15}$ for HP mass $m_{\tilde{\gamma}} \sim 0.1$ meV. These experiments use very same idea as the FUNK experiment, but in place of a single metallic mirror, they feature several layers of dielectric mirrors which serve as a conversion region and especially arranged to boost the signal power [54].

2.4 Search for HPDM with a dish antenna

The idea of utilizing a spherical cap with reflective surfaces — hence a *dish antenna* — was first proposed in [20]. The principle relies on the HP-Photon mixing which allows for a certain probability of surface emission of ordinary photons when the DM field impinges on a conducting material. More generally, the same principle applies to the extent that the DM field transits across two dielectric media with different refractive indices. The necessary condition being that the effective kinetic mixing χ_{eff} , which is function of the medium refraction index n as seen in Eq. (2.28), must jump sizably at the interface between the two media [65]. That is the idea relied by dielectric haloscopes mentioned earlier.

In this context, we may talk about HP-to-photon conversion in a rather loose manner. Indeed, it is not understood^{*i*} in the sense of oscillation from HP to ordinary photon state as usually pictured in laser and cavity experiments or also for the production of HPs in the interior of stars (see Sections 2.1.2 and 2.3.3). Instead, the surface emission comes from the interaction of the visible component, E_{DM} , of the HPDM field with ordinary charged matter, namely the free electrons of the conducting material. At this point, the

^{*i*} It is expressly clarified in [65] that both pictures are just two different limits of the same physics.

treatment is merely classical electromagnetism. These electrons can oscillate under the presence of the tiny \mathbf{E}_{DM} and emit an ordinary electromagnetic wave with the same frequency $\omega = m\tilde{\gamma}$.

This emitted wave is our HPDM signal. Hence, the first clear advantage is that we are looking for a monochromatic wave. Its power also scales with the emitting area. In addition, the low momentum of the HPs implies that the signal propagates almost perpendicularly to the emitting surface. Moreover, having a detector with sufficient spatial resolution, this directionality can further be exploited to confirm the DM nature of the signal.

In the following, we review the dish antenna calculations in greater details and improve them, in particular, by properly including the reflectivity^j of the emitting surface into the signal power and providing other generalization. Furthermore, we correct for a spurious numerical factor spotted in the original calculation of [20]. Finally, we discuss the sensitivity of a dish setup and address the main advantages and limitations of this technique.

^j This is not critical for good reflectors. However, a poor reflectivity can degrade the signal power significantly.

2.4.1 Surface emission

For general purpose, we consider two linear dielectric media with different refractive indices $n_1 = \sqrt{\epsilon_1}$ and $n_2 = \sqrt{\epsilon_2}$, and with a separation interface at $x = 0$, i.e within the (y, z) plane. We use the index 1 or 2, in subscript or superscript as convenient, to refer to quantities defined in one or the other medium. Let us now suppose a right-moving (from $x = -\infty$ to $x = +\infty$) HPDM electric field with amplitude $\hat{\mathbf{E}}_{m,\parallel}^0$. We want to study the reflection and transmission properties of the interface between the two media.

For simplicity, we first assume normal incidence at the interface. The solutions to the propagation equations are given by the superposition of plane-wave eigenstates according Eq. (2.26). The fields amplitudes are simply fixed by the initial and boundary conditions. The usual equations $\nabla \times \mathbf{E} = -\partial_t \mathbf{B}$ and $\nabla \times \hat{\mathbf{E}} = -\partial_t \hat{\mathbf{B}}$ ensure the continuity of the tangential components of the electric fields at the interface. Furthermore, we also require the continuity of their first derivatives. Hence at $x = 0$, the interface conditions are

$$\begin{aligned} \hat{\mathbf{E}}_{m,\parallel}^0 \begin{pmatrix} -\chi_1 \\ 1 \\ \chi_1 p_1 \\ -p_1 \end{pmatrix} e^{i(\omega t - \mathbf{p}_1 \cdot \mathbf{x})} + \hat{\mathbf{E}}_{m,\parallel}^{(1)} \begin{pmatrix} -\chi_1 \\ 1 \\ -\chi_1 p_1 \\ p_1 \end{pmatrix} e^{i(\omega t + \mathbf{p}_1 \cdot \mathbf{x})} + \mathbf{E}_{m,\parallel}^{(1)} \begin{pmatrix} 1 \\ \chi_1 - \chi \\ k_1 \\ (\chi_1 - \chi)k_1 \end{pmatrix} e^{i(\omega t + \mathbf{k}_1 \cdot \mathbf{x})} \\ = \hat{\mathbf{E}}_{m,\parallel}^{(2)} \begin{pmatrix} -\chi_2 \\ 1 \\ \chi_2 p_2 \\ -p_2 \end{pmatrix} e^{i(\omega t - \mathbf{p}_2 \cdot \mathbf{x})} + \mathbf{E}_{m,\parallel}^{(2)} \begin{pmatrix} 1 \\ \chi_2 - \chi \\ -k_2 \\ -(\chi_2 - \chi)k_2 \end{pmatrix} e^{i(\omega t - \mathbf{k}_2 \cdot \mathbf{x})}. \end{aligned} \quad (2.37)$$

The symbol \parallel is to indicate the parallel components of the fields^k. Let us notice that, only here, we have explicitly written the plane-wave solutions in such a way that they are left-moving in medium (1) (reflected) and right-moving in medium (2) (transmitted). To satisfy the conditions in Eq. (2.37) at all time, all plane waves must oscillate at the same frequency $\omega = m_{\bar{\gamma}}$. Then, to satisfy these at all positions (y, z) on the interface, the initial normal incidence implies $p_i = (m_{\bar{\gamma}}v_{\text{DM}}, 0, 0)^T$, $k_i = (n_i m_{\bar{\gamma}}, 0, 0)^T$. Furthermore, the effective mixing in Eq. (2.28) simplifies to $\chi_i = \chi/n_i^2$.

^k \mathbf{E} is always transverse to the propagation direction, while the direction of $\hat{\mathbf{E}}$ can be arbitrary [65].

Given an initial condition $\hat{\mathbf{E}}^0$, it is easy to solve Eq. (2.37) at $x = 0$. At the leading order, the field amplitudes are given by

$$\text{reflected} \begin{cases} \mathbf{E}_{m,\parallel}^{(1)} = \frac{2p_1(\chi_1 - \chi_2)(k_2 - p_2)}{(p_1 + p_2)(k_1 + k_2)} \hat{\mathbf{E}}_{m,\parallel}^0 & \approx \frac{\chi}{n_1^2} \left(1 - \frac{n_1}{n_2}\right) \hat{\mathbf{E}}_{m,\parallel}^0 \\ \hat{\mathbf{E}}_{m,\parallel}^{(1)} = \frac{p_1 - p_2}{p_1 + p_2} \hat{\mathbf{E}}_{m,\parallel}^0 & \approx 0 \end{cases} \quad (2.38)$$

$$\text{transmitted} \begin{cases} \mathbf{E}_{m,\parallel}^{(2)} = \frac{2p_1(\chi_2 - \chi_1)(k_1 + p_2)}{(p_1 + p_2)(k_1 + k_2)} \hat{\mathbf{E}}_{m,\parallel}^0 & \approx \frac{\chi}{n_2^2} \left(1 - \frac{n_2}{n_1}\right) \hat{\mathbf{E}}_{m,\parallel}^0 \\ \hat{\mathbf{E}}_{m,\parallel}^{(2)} = \frac{2p_1}{p_1 + p_2} \hat{\mathbf{E}}_{m,\parallel}^0 & \approx \hat{\mathbf{E}}_{m,\parallel}^0. \end{cases} \quad (2.39)$$

In the last approximations, we replaced the effective mixing and momenta with their respective expressions and neglected the $p_2 \sim 10^{-3}m_{\bar{\gamma}}$ compared to $k_{1,2} \sim m_{\bar{\gamma}}$. These results can be cross-checked with the derivation in [65].

To make the meaning of Eqs. (2.38) and (2.39) more transparent, let us consider the following situation. We suppose the medium (1) is vacuum, i.e. $n_1 = 1$, and medium (2) consists of some dielectric material. First, it is clear that the hidden electric field traverses across the two media almost unimpeded. This is of course to be expected since it is only its ordinary field partner which interacts with matter, namely with the atoms of the dielectric material.

On the other-hand, we have ordinary electric fields emitted at the interface and propagating away on both sides with amplitudes suppressed by the mixing parameter. This can again be easily understood. Our DM solution carries an ordinary electric field with amplitude $\propto \chi$. This oscillating field can excite the vibrational mode of electrons in the medium, which in turns, emit an electromagnetic wave matching the same frequency. The fractions of reflected and transmitted amplitudes simply involve the reflectivity of the interface between the two media.

If we consider medium (2) to be a good reflector for the wavelength of interest^l, i.e. with $|n_2(\lambda)| \gg 1$, we obtain $|\mathbf{E}_{m,\parallel}^{(1)}| \approx \chi |\hat{\mathbf{E}}_{m,\parallel}^0|$ and $|\mathbf{E}_{m,\parallel}^{(2)}| \approx 0$. The

^l For e.g. in the visible spectrum, we can use a metallic mirror.

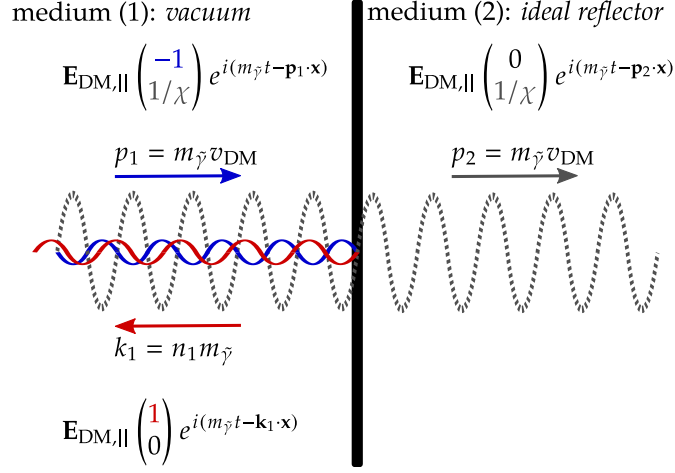


Figure 2.2: Boundary conditions for normal incidence and surface emission. The dashed wave represents the hidden component of the HPDM field, which is fully transmitted with $\mathbf{E}_{\text{DM},\parallel} = \chi \hat{\mathbf{E}}_{m,\parallel}^0$. The solid waves are the visible fields. In blue is the incoming wave, and in red the reflected one with the same amplitude but phase shifted. Let us remark that for these ordinary electric fields, the total phase shift equals π at the point of reflection. At other locations, the differing phase velocities between the incoming ($\lambda = 2\pi/(m_{\tilde{\gamma}}v_{\text{DM}})$) and outgoing ($\lambda = 2\pi/m_{\tilde{\gamma}}$) waves contributes to an additional phase shift. Thus we do not have a complete destructive interference.

ideal situation is sketched in Fig. 2.2. Since we argued that having a good reflector is rather a desirable feature for the dish antenna method to work, we focus on such a setup from now on and neglect the transmitted wave.

2.4.2 Directionality

In the previous section, we have seen that in case of normal incidence the outgoing wave is emitted perpendicularly to the interface. Naturally, the same result also holds if we neglect the HP momentum since only momentum in the tangential direction needs to be conserved. For non-normal incidence, the interface conditions depicted in Fig. 2.2 are always applicable with the difference that we must also ensure that the non-vanishing tangential components of the wave vectors are continuous^m, i.e. $\mathbf{k}_1 \cdot \mathbf{x}|_{(x=0,y,z)} = \mathbf{p}_1 \cdot \mathbf{x}|_{(x=0,y,z)}$. On the other hand, the energy conservation implies $|\mathbf{k}_1|^2 = |\mathbf{p}_1|^2 + m_{\tilde{\gamma}}^2$. Writing these conditions in terms of the parallel and normal components of the wave vectors, we have

$$\begin{aligned} k_{1,\parallel} &= p_{1,\parallel} = p_1 \sin \tilde{\beta} \\ k_{1,\perp} &= \sqrt{p_{1,\perp}^2 + m_{\tilde{\gamma}}^2} = \sqrt{p_1^2 \cos^2 \tilde{\beta} + m_{\tilde{\gamma}}^2}, \end{aligned} \quad (2.40)$$

^m For the hidden field, the momentum is fully transmitted, so $\mathbf{p}_1 = \mathbf{p}_2$.

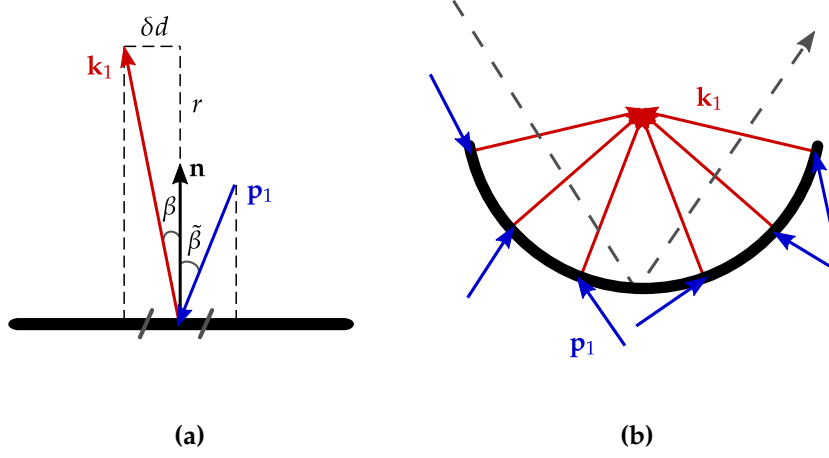


Figure 2.3: (a) Illustration of the direction of propagation of the reflected signal (originally sketched in [66]). (b) The idea of a dish setup (originally sketched in [20]). Signal come together at the center of curvature of the dish. Background lights from far-away are reflected at the focal point (half-radius), reflection from near-by sources (dash gray line) are unfocused.

where $\tilde{\beta}$ is the angle of incidence of the HPDM field with respect to the normal to the interface plane. Thus, the outgoing wave is emitted with an angle β such that

$$\sin \beta = \frac{k_{1,\parallel}}{k_1} = \frac{v_{\text{DM}} \sin \tilde{\beta}}{\sqrt{1 + v_{\text{DM}}^2}}. \quad (2.41)$$

At a finite distance r from the interface, this gives a displacement of

$$\delta d = r v_{\text{DM}} \sin \tilde{\beta} + \mathcal{O}(v_{\text{DM}}^2), \quad (2.42)$$

with respect to the normal direction. The angles $\tilde{\beta}$, β and the displacement δd are illustrated in Fig. 2.3(a). Looking at Eq. (2.42), it is clear that the offset is small. At a few meters of distance, the signal emitted by a single surface element is only displaced by a few millimeters with respect to the normal direction. In other words, the signal is focused and we can gain a geometrical amplification by using a spherical cap (see Fig. 2.3(b)). At the center of curvature of the latter, the signal intensity is spread over a small area of radius $\sim r v_{\text{DM}}$.

A more careful calculation which takes into account the spherical aberration for large geometry, as it is case of the FUNK experiment, leads to an increase of the spreading radius by about 70% [66]. In addition, there is also a global offset of the main peak of the order of $r v_{\text{lab}}$, which is due the movement of earth, and thus the lab frame, with respect to galactic rest-frame

and the earth's precession around the north pole [67]. Ultimately, the spatial distribution of the signal and its seasonal movement onto the detector's plane enable a directional sensitivity for the dish setup, which can be used to map-out the full velocity distribution of DM in the galactic halo.

For the FUNK experiment, aiming first at discovering HPDM signature, the directional information is not primarily essential. Indeed, it is averaged-out¹ in the signal power estimate. Nevertheless, the detector size (29 mm diameter) were chosen as large enough in order to accommodate these broadening effects.

¹ We actually average over the direction of the HP field. However, since only parallel components are converted, these also depend on the momentum distribution.

2.4.3 Signal power

The situation is already pictured in Fig. 2.2. As mentioned, we are essentially interested in the reflected electromagnetic wave in medium (1). Nonetheless, we leave the expression of the refractive index general for the moment. For estimating the signal power, we can neglect the HP momentum by setting $\mathbf{p}_1 = \mathbf{0}$, because most of their energy comes from their mass with a small correction of $\mathcal{O}(v_{\text{DM}}^2)$. By extension, this also means that we do not expect a significant modulation of the signal power or the signal rate — neither from a finite distribution of the DM velocities nor from the movement of Earth through the DM wind — as long as we sufficiently capture all signals. In line with our former discussion, these information are only relevant for searches aiming at directional sensitivity and using detectors with spatial resolution.

The FUNK experiment searches for a first signal. At a finite distance from the interface, we measure an ordinary electric field \mathbf{E}^{out} , which is a superposition of the reflected field interfering with the DM field. Plugging the solutions (2.38) into the left-hand side of Eq. (2.37), we have

$$\begin{aligned} \mathbf{E}^{\text{out}} \equiv \mathbf{E}_{\parallel}^{\text{out}} &= \mathbf{E}_{\parallel}^{(1)} - \chi_1 \hat{\mathbf{E}}_{\parallel}^0 \\ &= \mathbf{E}_{m,\parallel}^{(1)} e^{i(m\gamma t - \mathbf{k}_1 \cdot \mathbf{x})} - \chi_1 \hat{\mathbf{E}}_{m,\parallel}^0 e^{im\gamma t} \\ &= \frac{\mathbf{E}_{\text{DM},\parallel}}{n_1} e^{im\gamma t} \left(\frac{1}{\eta} e^{-i\mathbf{k}_1 \cdot \mathbf{x}} - \frac{1}{n_1} \right). \end{aligned} \quad (2.43)$$

In the last step, we have introduced the coefficient

$$\frac{1}{\eta} = \frac{1}{n_1} - \frac{1}{n_2}, \quad (2.44)$$

which will be related to the surface reflectivity. Besides, the parallel component of the *visible* DM field is given by

$$\mathbf{E}_{\text{DM},\parallel} = \chi \hat{\mathbf{E}}_{m,\parallel}^0 = \chi \hat{\mathbf{E}}_m^0 \cos \alpha, \quad (2.45)$$

where α denotes the angle between the incident $\hat{\mathbf{E}}_m^0$ and the interface plane. The oscillating field \mathbf{E}^{out} also generates an auxiliary magnetic field

$$\mathbf{H}^{\text{out}} = -\frac{\mathbf{k}_1 \times \mathbf{E}^{\text{out}}}{m_{\bar{\gamma}}}. \quad (2.46)$$

The energy flux density associated to this outgoing electromagnetic wave is given by the usual Poynting vector defined as,

$$\mathbf{S} = \Re(\mathbf{E}^{\text{out}}) \times \Re(\mathbf{H}^{\text{out}}). \quad (2.47)$$

To evaluate the real part of the electric and magnetic fields, which represent the physical states, let us introduce the following notations. We write $n_1 = |n_1|e^{i\delta_1}$, $\eta = |\eta|e^{i\phi}$ and $\mathbf{E}_{\text{DM}} = |\mathbf{E}_{\text{DM}}|e^{i\psi}$, where δ_1, ϕ, ψ are complex phases. In general, the momentum \mathbf{k}_1 also acquires an imaginary part through the complex index^o n_1 . This gives an attenuation coefficient $a_1 = \Im(n_1)m_{\bar{\gamma}}$ such that $e^{-i\mathbf{k}_1 \cdot \mathbf{x}} = e^{-a_1x}e^{-in_1^*m_{\bar{\gamma}}x}$, where n_1^* is here understood as the real part of the refractive index. Then using Eqs. (2.43) and (2.46), the physical fields can be expressed as follows,

^o In our convention, the refractive index is in the form $n = 1 + \kappa_e - i\sigma_e/\omega$, see Eq. (2.20).

$$\Re(\mathbf{E}^{\text{out}}) = \mathbf{u} \frac{|\mathbf{E}_{\text{DM},\parallel}|}{|n_1|} \left\{ \frac{1}{|\eta|} e^{-a_1x} \cos(m_{\bar{\gamma}}(t - n_1^*x) - \delta_1 - \phi + \psi) - \frac{1}{|n_1|} \cos(m_{\bar{\gamma}}t - \delta_1 + \psi) \right\}, \quad (2.48)$$

$$\Re(\mathbf{H}^{\text{out}}) = (\mathbf{x} \times \mathbf{u}) \frac{|\mathbf{E}_{\text{DM},\parallel}|}{|\eta|} e^{-a_1x} \cos(m_{\bar{\gamma}}(t - n_1^*x) - \phi + \psi), \quad (2.49)$$

where \mathbf{u} and \mathbf{x} are unit vectors along the directions of the electric field $\mathbf{E}_{\text{DM},\parallel}$ and propagation \mathbf{k}_1 .

We are now ready to compute the average signal power P emitted by an interface of area A , such that $P = A\overline{|\mathbf{S}|}$. Using Eqs. (2.48) and (2.49), we obtain

$$P = \frac{A}{2} \frac{\langle |\mathbf{E}_{\text{DM},\parallel}|^2 \rangle}{|n_1| |\eta|} e^{-a_1x} \times \overline{\left[\frac{1}{|\eta|} e^{-a_1x} \cos \delta_1 - \frac{1}{|n_1|} \cos(\delta_1 + \phi - n_1^*m_{\bar{\gamma}}x) \right]_x}. \quad (2.50)$$

This expression is general^p. The parameter $1/|\eta|$ encodes the reflectivity of the interface with regards to the DM field. The exponential term accounts for the damping of the propagating wave in lossy media. And the oscillating term describes the interference pattern between the signal and the

^p The same expression holds for axion signal, by replacing \mathbf{E}_{DM} with an appropriate amplitude scale, for e.g. see Eq. (3.12) in [54].

(homogeneous) DM field. The average is taken over all pointing directions of \mathbf{E}_{DM} (indicated by the bracket), along the direction of propagation x , and over the time t . The details of the averaging are relegated to Appendix B.1. Ultimately, Eq. (2.50) can be written as

$$\begin{aligned} P &= \frac{A}{2|\eta|^2} \langle |\mathbf{E}_{\text{DM},\parallel}|^2 \rangle \langle \cos^2 \alpha \rangle \\ &= \frac{A}{|\eta|^2} \chi^2 \langle \cos^2 \alpha \rangle \rho_{\text{CDM}}. \end{aligned} \quad (2.51)$$

The last step follows from our assumption, in Eq. (2.36), that the cold DM relic is entirely composed of HP condensate. As for the reflectivity, we can see from Eq. (B.6) that a good reflector has

$$\frac{1}{|\eta|^2} = \frac{1+R}{2} + \mathcal{O}(R-1)^2. \quad (2.52)$$

2.4.4 Sensitivity

Eq. (2.51) directly translates the sensitivity of a dish setup to the strength of the mixing parameter. This reads as

$$\chi = 3.2 \times 10^{-14} \left(\frac{P_{\text{det}}}{10^{-23} \text{ W}} \right)^{1/2} \left(\frac{A/|\eta|^2}{\text{m}^2} \right)^{-1/2} \left(\frac{\langle \cos^2 \alpha \rangle}{2/3} \right)^{-1/2} \left(\frac{\rho_{\text{CDM}}}{0.3 \text{ GeV cm}^{-3}} \right)^{-1/2}, \quad (2.53)$$

where P_{det} is the minimum detectable power of HP induced signal in presence of background and taking finite efficiency of the detector. The above expression suggests that with the goal of achieving a high sensitivity, we need to have (i) a good reflector, (ii) a large reflecting area with very good focus, and (iii) a detector capable of measuring a very low signal power. Fulfilling these requirements is what indeed brings some limitations to the dish antenna technique. We will comment on that in a moment.

Depending on the investigated spectral range and the available detector technology, it is sensible to express Eq. (2.53) either in terms of the signal power P_{det} (at lower frequencies) or the signal rate R_{det} (at higher frequencies). The current status of the FUNK experiment, which is the main emphasis of this work, is situated in the optical spectrum. There, we can use a photodetector at the quantum limit and count single photons emitted from the surface. In this case, R_{det} depends on the dark count rate of the detector, its quantum efficiency and the measurement time. In the future, we also plan to extend the scope of search to microwave frequencies. Then, P_{det} is more conveniently expressed in terms of the noise temperature of the detector, the detection bandwidth, and the integration time. We examine both cases separately in Sections 3.2.1 and 3.3.1.

Advantages of a dish setup

Let us now return to our general discussion on the sensitivity of such an experiment, starting with the real benefits.

- Signal focused at twice the focal point
As illustrated in Fig. 2.3(b), the spherical design of the antenna provides an enhancement of the signal power thanks to a geometrical amplification and a background suppression^q. All emitted signal waves are gathered at the center of the sphere, while far-away background join at the focal point (at half the radius). Other sources reflected by the surface are typically not focused. Moreover, as argued in [20], the loss of resonance enhancement in comparison with cavity experiments, is typically compensated by an effective quality factor $\sim A/\lambda_{\bar{\gamma}}^2$ of the dish setup. In particular, in (sub)-optical wavelengths it is currently the best option because the resonance enhancement of optical cavities ($\propto \lambda_{\bar{\gamma}}^2$) and other geometrical factors quickly degrade at shorter wavelengths.
- Broadband search
In contrast with cavity experiments, a dish experiment does not require a tuning of the *volume* of the setup to match the HP mass and demands a very slow scan over the mass range. In other terms, we can perform a broadband scan with essentially the same setup. The performance of such a scan is only limited by the bandwidth and sensitivity reach of the available detector in the desired mass range.
- Narrow peak signal
Since the HPs are very cold, we expect a clear monochromatic signal peaked at a frequency $\omega \approx m_{\bar{\gamma}}$. Although the signal power is feeble, it should be distinguishable from other noise such as thermal background which has a white spectrum. The width of the HPDM line depends on the velocity distribution of local DM. Assuming a Maxwellian distribution, we find in Eq. (B.17) that for GHz–THz frequencies, the signal widths are in the kHz–MHz ranges, which should be within the bandwidth resolution of most spectrometers.

^q This does not apply to background from sources directly hitting the detector.

Limitations

Naturally, the dish antenna technique presents some limitations which are in competition with the advantages listed above. Besides the technical challenge of overcoming $\chi \propto \sqrt{P_{\text{det}}}$ with very low-noise detectors and an effective background reduction, the design of the setup limits the usage to frequency ranges from microwaves to Ultraviolet (UV). Nonetheless, that gives us a space of about 6 orders of magnitude in masses to explore.

- **Reflectivity**
As argued, a crucial condition for the signal detection is that the surface material must have a high reflection coefficient, and thus a negligible absorption coefficient, within the range of wavelengths of interest. For the FUNK experiment, which uses an aluminum-coated mirror, this severely limits the sensitivity to frequencies beyond far-UV, i.e above a few 10 eV. At higher frequencies, the aluminum becomes transparent [68] and overkill any potential signal.
- **Loss of focus**
For the dish principle to work, it is also primarily essential to achieve an optimal geometrical amplification. This brings two issues. First, the convergence mechanism is only effective in the limit where diffraction can be neglected, i.e when the light-ray approximation is valid. This also includes possible roughness of the surface. For a setup of the size of FUNK, this limits its sensitivity to masses above a few μeV [20]. Second, as discussed in Section 2.4.2, due to the non-ideal imaging property of the spherical antenna and the DM velocity dispersion, the signal is spread over some finite area. Moreover, the relative motion of Earth in the galactic frame drives the signal spot around a certain pattern. Capturing sufficiently these variations necessitates a larger detector area. However, this is only reasonable if the increase of the background rate of the detector is slower than the increase of the captured signal rate, with an increasing area of the detector.

Summarizing, using the dish antenna technique, the FUNK experiment can probe HPDM with masses between $\mathcal{O}(\mu\text{eV})$ and $\mathcal{O}(10\text{ eV})$. The method is a broadband scan and the sensitivity is, in principle, only detector limited.

3

The FUNK experiment

Contents

3.1 General setup	32
3.1.1 Facility	32
3.1.2 Mirror	33
3.2 Search in the near-UV and visible spectra	37
3.2.1 Sensitivity equation	37
3.2.2 Detector	37
3.2.3 Data Acquisition chain	41
3.2.4 Single Photoelectron calibration	43
3.2.5 Temperature and Pressure monitoring	53
3.2.6 Muon monitoring	54
3.3 A glimpse into FUNK++	57
3.3.1 Sensitivity equation	58
3.3.2 Sensitivity limits	59

The FUNK or Finding U(1)s of Novel Kind experiment is dedicated to search for direct evidences of Hidden-Photon Dark Matter (HPDM). Based on the idea of a dish antenna explained in Section 2.4, the experiment uses a large spherical metallic mirror with an area of ($\sim 14 \text{ m}^2$) to convert possible local HP condensates into real detectable photons. These photons constitute our Dark Matter (DM) signal. They come together at the center of curvature of the “mirror sphere” where we placed a suitable photo-detector. This simple setup also has the convenient merit that with a minimum modification, it is feasible to probe with high-sensitivity a huge portion of the uncharted HPDM parameter space, from μeV to eV mass ranges. In its current phase, the FUNK experiment operates in the eV range and searches for HP-to-photon signature in the optical spectrum. Initial testings were first conducted with a readily available Charge-Coupled Device (CCD) camera [69], after which



Figure 3.1: The FUNK experiment in image.

FUNK underwent several upgrades to eventually improve its sensitivity by more than two orders of magnitude.

In this chapter, we go through details of the experiment and the search in the middle-Ultraviolet (UV) and visible spectra. Furthermore, we discuss experimental challenges and strategies for FUNK++, the future of the experiment at lower energies. We give benchmarks for the potential sensitivity reaches of FUNK++, using various detectors in radio frequencies.

3.1 General setup

3.1.1 Facility

The initial phase of FUNK began in earlier 2015. The basic experimental setup consists of three main parts: *(i)* a portion of a spherical mirror — *(ii)* a dedicated low-noise photo-detector — *(iii)* the Data Acquisition (DAQ) related instruments. We describe the aspects of each of these parts in the following sections. The entire equipment was installed inside a closed experimental facility located at the Institute of Nuclear Physics of KIT Campus Nord. This large facility ($18 \times 14 \times 9 \text{ m}^3$) formerly housed a Van-de-Graff accelerator, and as such, offers excellent environmental stability and isolation from possible external nuisances, especially thanks to its $\approx 2 \text{ m}$ thick concrete walls.

The main experimental zone takes up a volume of $4.98 \times 4.35 \times 4.30 \text{ m}^3$ and has been enclosed with a double-layer light-tight shielding made of $\approx 120 \text{ }\mu\text{m}$ black polyethylene sheet stretched over a thick-cotton curtain. Furthermore, we treated the floor within this confined area with a non-reflective matte-black paint. These measures were taken mainly to limit contributions from ambient background sources as well as their possible reflections (e.g. Cherenkov photons in air which we discuss in Chapter 4). In addition, we also carefully removed all potential light sources inside the hall (e.g. residual neon light-bulbs).

Our installation allows us to remotely control all movable parts of the setup. These operations are fully automated. Thus during a measurement campaign, the experimental hall is locked-down and the data-taking runs in complete darkness. Furthermore, we continuously monitor the environmental conditions inside the hall before, during and after a complete run. These measurement procedures are further explained in Section 3.2.

3.1.2 Mirror

We reused parts of a spherical mirror originally manufactured for the fluorescence telescopes of the Pierre Auger Observatory [70]. The mirror consists of 36 individual segments with equal height $\delta h = 65 \text{ cm}$ but gradually decreasing widths, $65 \text{ cm} \geq \delta w \geq 55 \text{ cm}$, away from the equator. Each segment has a $\sim 18 \text{ mm}$ thick aluminium backing which were milled to reproduce the spherical shape, and then coated at high temperatures with $\sim 3 \text{ mm}$ layer of AlMgSi. The edges and inner reflective surface were then precisely milled with special diamond tools and finally protected by electrochemical anodisation [71]. These different procedures ultimately yields an overall reflectivity^a $R \approx 88 \%$ in the visible and near-UV spectra. The outer surface includes mechanical pieces necessary for the assembly and adjustment of the mirror matrix, see Fig. 3.3(a).

^a Our prototype has slightly lower reflectivity $R \approx 80 \%$.

The fully assembled mirror is a portion of a sphere with radius $r = 3.40 \text{ m}$. The delimiting four corners form a rectangular cut-out with height $h = 3.72 \text{ m}$ and width $w = 3.70 \text{ m}$. With such a geometry, the total reflecting surface A_{mirr} can be calculated as follows,

$$\begin{aligned} A_{\text{mirr}} &= r^2 \int_{\frac{\pi}{2}-\vartheta_0}^{\frac{\pi}{2}+\vartheta_0} d\vartheta \sin \vartheta \int_0^{\varphi_0} d\varphi \\ &= 2rh \arcsin(w/2r) = 14.56 \text{ m}^2, \end{aligned} \quad (3.1)$$

where $\sin \vartheta_0 = h/2r$ and $\sin(\varphi_0/2) = w/2r$ as sketched in Fig. 3.3(b). The assembling and testing of the mirror are reported in greater details in [69, 72]. In the following sections, we summarize the main achievement during these earlier stages of FUNK.

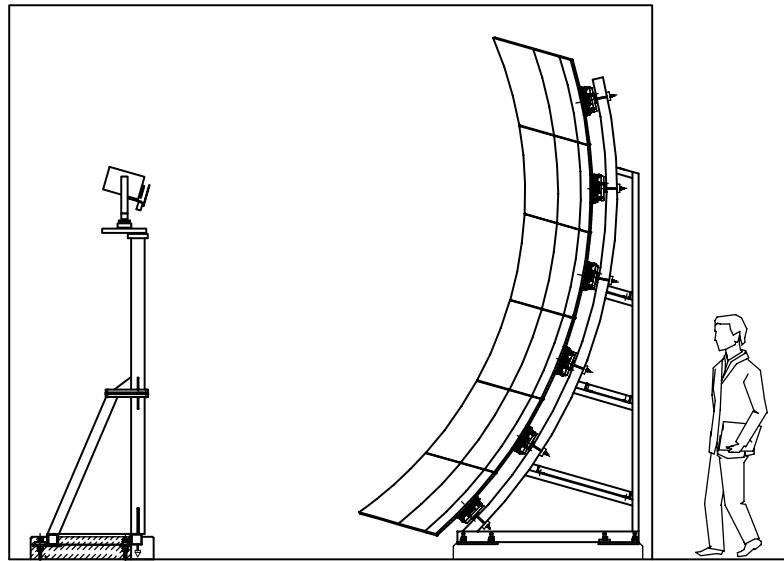


Figure 3.2: FUNK mirror setup. The photodetector is mounted on top of the pillar drawn, on the left, which is located at the central spot. The right part of the figure shows a comparison of the mirror size with a human body.

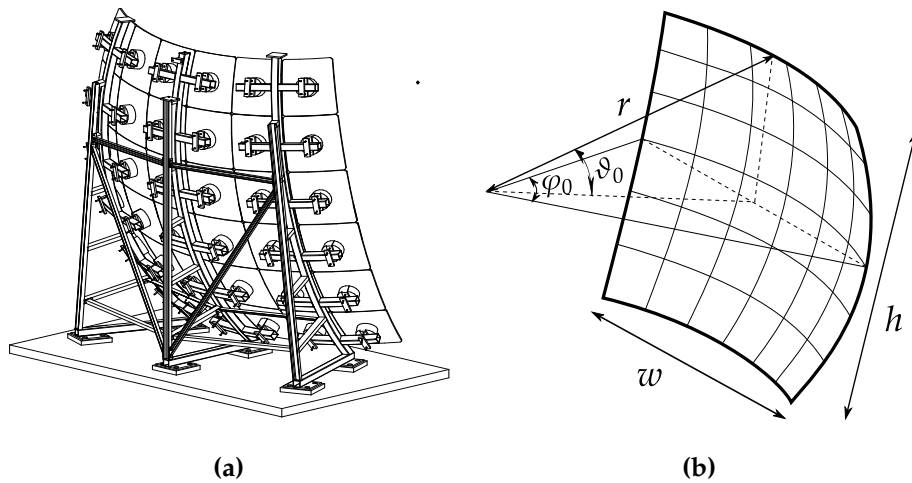


Figure 3.3: (a) Sketch of the mounting structure viewed from the back. Each mirror segment is attached to the metallic support via a single ball-joint, which allows precise longitudinal and directional adjustments. (b) Dimensions of the whole mirror with $r = 3.4$ m, $h = 3.72$ m, $w = 3.70$ m, $\vartheta_0 = 33^\circ$, and $\varphi_0 = 66^\circ$.

Initial assembly

The mirror is assembled in a 6×6 matrix. Initially, the assembly is conducted according to the same specifications as for the Auger fluorescence detectors. A rather strict requirement for FUNK is to achieve an optimal convergence of

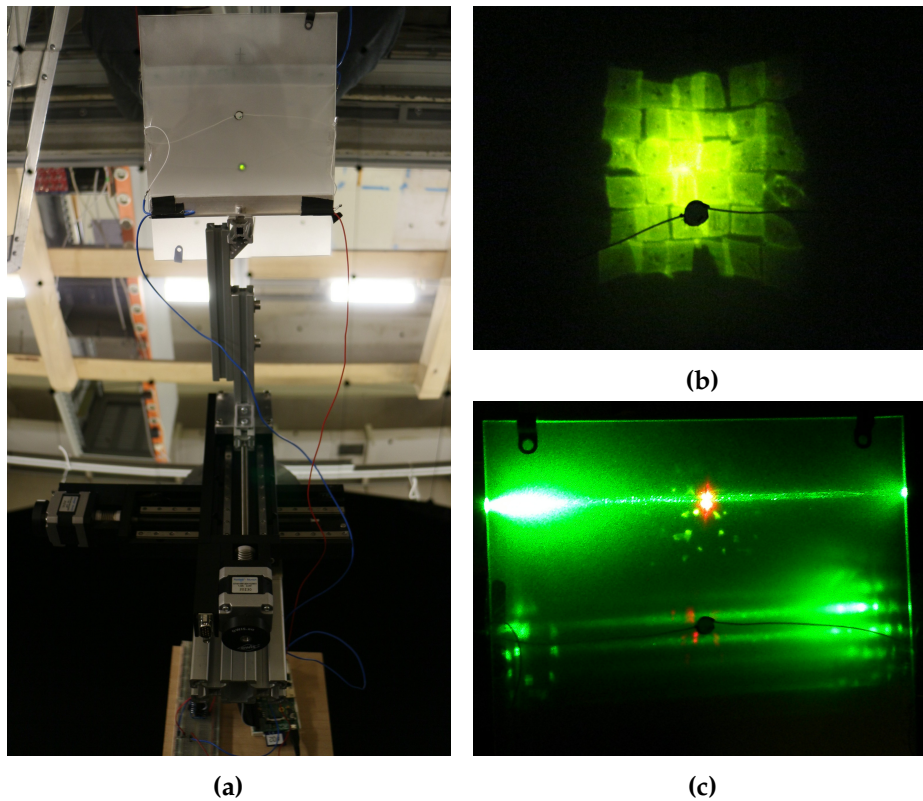


Figure 3.4: (a) Imaging device platform. The top part displays the frosted-glass onto which we can also see the LED and its reflected image. The bottom part shows the linear stage together with some electronic controllers. (b) Cross-sectional image obtained on the frosted glass as we drive the platform towards the mirror, away from the radius point. (c) Capture of the two crossing laser-beams (red and green) used for marking the final central spot.

the reflecting surfaces at the center of the sphere. For this purpose, we built a movable imaging platform to study the optical performance of the mirror. The imaging device, shown in Fig. 3.4(a), comprises a frosted-glass serving as a screen and a yellow-green LED used as a light source. The ensemble was mounted on a remotely controlled and motorized linear-stage.

The linear stage allows the platform to move along the mirror axis. Then, for each longitudinal position of the platform, a cross-sectional image of the reflected light-beams is captured. An example of such a capture is shown in Fig. 3.4(b). In this particular case, the LED was driven off the center of curvature, towards the focal point so that the mirror segments were not converging and we can see their individual shapes and aberrations. We employed a CCD camera to observe the LED reflection pattern on the frosted-glass screen, as we scanned around the central region.

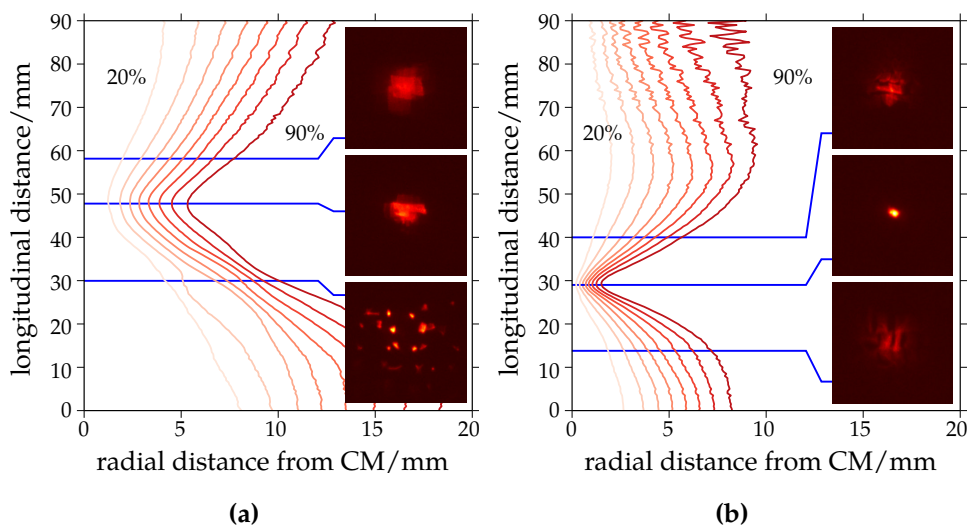


Figure 3.5: Point-spread function of the mirror before **(a)** and after **(b)** of the fine realignment campaign. Contour lines are drawn in step of 10 %, from 20 % to 90 % of the total amount of converging light (see text for details).

The result of such a scan is shown in Fig. 3.5(a), where contour-lines indicate fractions of light contained within certain radial distances around the image center-of-mass. The insets display images obtained at three longitudinal distances: before, at, and after the plane of maximal convergence. The location of the latter also contains the radius point. Nonetheless, the relatively large size of the smallest image-spot achieved, 90 % of the light within a radius of ~ 6 mm, suggests that the mirror elements, as an ensemble, are out of focus.

Realignment

The difficulty in achieving a better convergence (smaller image) and a better focus (sharper image) is two-fold: minimize the optical aberration of the mirror as a whole due its spherical geometry, and compensate for possible discrepancy between the radii of curvature of the individual elements. However, since it is possible to finely adjust the position and orientation of each mirror segment, the problem is solvable. After a dedicated realignment campaign, this procedure ultimately yielded an improvement of the point-spread function of the mirror by a factor of 3, with 90 % of the light contained within a ~ 2 mm spot-radius, as shown in Fig. 3.5(b). Finally, the new position of the central spot was marked for future references with two crossing laser-beams^b, which are illustrated in Fig. 3.4(c).

^b The central point is at half-distance between the LED and its point image within the frosted-glass plane.

3.2 Search in the near-UV and visible spectra

3.2.1 Sensitivity equation

The general sensitivity equation of a dish experiment to strength of the kinetic-mixing parameter χ is given in Eq. (2.53), in terms of the minimum detectable signal power P_{det} . In the optical spectrum, it is sensible to talk about single-photon emission from the mirror surface. Therefore, we aim to setup a counting experiment. Visible frequencies can be easily covered by Photomultiplier Tubes (PMTs) and further extended to UV frequencies with some specific tubes. We follow this option. The chosen PMT model is described in the next section.

For now, we want to express the sensitivity equation, more conveniently, in terms of the minimal detectable rate of HP-induced photons R_{det} . This is given by

$$P_{\text{det}} = R_{\text{det}} m_{\tilde{\gamma}} / q_{\text{eff}}, \quad (3.2)$$

where q_{eff} the quantum efficiency of the detector, internally limiting the counting. From Eq. (2.53), it follows that

$$\begin{aligned} \chi = 4.1 \times 10^{-12} & \left(\frac{R_{\text{det}}}{\text{Hz}} \frac{m_{\tilde{\gamma}}}{\text{eV}} / q_{\text{eff}} \right)^{1/2} \left(\frac{A/|\eta|^2}{\text{m}^2} \right)^{-1/2} \\ & \times \left(\frac{\langle \cos^2 \alpha \rangle}{2/3} \right)^{-1/2} \left(\frac{\rho_{\text{CDM}}}{0.3 \text{ GeV cm}^{-3}} \right)^{-1/2}. \end{aligned} \quad (3.3)$$

For practical application, R_{det} is limited by the dark count rate R_{dark} of the detector and the total measurement time t_{tot} . In absence of signal and assuming Poisson statistics, we have $R_{\text{det}} < \sqrt{2R_{\text{dark}}/t_{\text{tot}}}$ which yields

$$\chi \lesssim 1.2 \times 10^{-13} \left(\frac{R_{\text{dark}}}{\text{Hz}} \frac{\text{month}}{t_{\text{tot}}} \right)^{1/4} \left(\frac{m_{\tilde{\gamma}}}{\text{eV}} / q_{\text{eff}} \right)^{1/2} \left(\frac{A/|\eta|^2}{\text{m}^2} \right)^{-1/2}. \quad (3.4)$$

Thus, given an experimental setup, reducing and stabilizing the dark count rate is equally important as increasing the measurement time. The former option is more challenging but it keeps systematical uncertainties under control compared to statistical uncertainties. On the other hand, increasing the measurement time from one-month to one-year worth of data-taking would only improve the above limit by roughly 1/2.

3.2.2 Detector

We employ a 29 mm diameter PMT from the ET-9107QB low-noise series [73] manufactured by ET-Enterprises, see Fig. 3.6(a). This PMT offers an

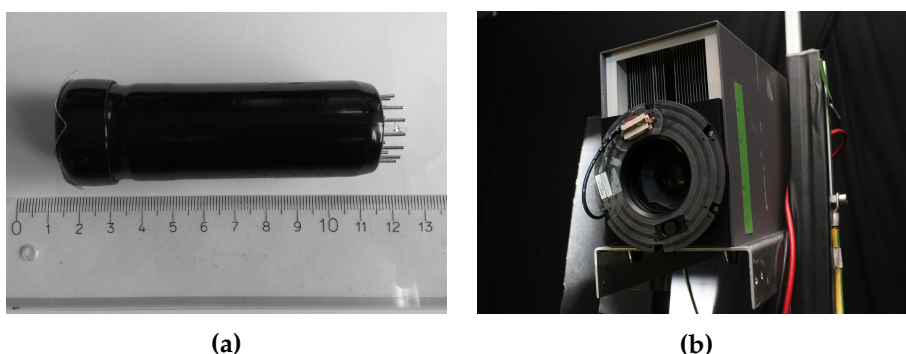


Figure 3.6: (a) Photograph of the ET-9107QB PMT. The entrance window is on the left-end (here covered), and some pin connectors to a high-voltage base are seen on the right-end. (b) Photograph of FACT50 housing the PMT with the NS65B optical shutter mounted in front. The photocathode can be seen through the iris-shutter. Also see Fig. 3.8.

appreciable high-gain performance at relatively low-voltage supplies, and a good Single Photoelectron (SPE) resolution, making it a suitable choice for single-photon counting applications. For the moment, we shall postpone all discussion about noise and dark currents to Chapter 4.

The PMT entrance window is made of a high-purity fused-silica glass which has a wide transparency range, with a transmission coefficient $\gtrsim 90\%$ from UV to near-Infrared (IR). The bialkali photocathode is sensitive to wavelengths from 150 nm to 630 nm, where the quantum efficiency^c q_{eff} exceeds 1% and reaches a peak of $q_{\text{eff}} \approx 24\%$ at $\lambda = 330$ nm. The quantum efficiency of the employed PMT is plotted in Fig. 3.7 as function of the incident photon wavelength. The active area of the photocathode has a diameter of ~ 25 mm, ensured to be large enough to compensate for eventual optical aberration and capture all possible HP signals emitted from the surface of the mirror, even in the presence of seasonal movements (see Section 2.4.2). Finally, the electron multiplier stage consists of 11 high-gain and high-stability Sb-Cs dynodes arranged on a linear voltage divider.

The operating voltage of the PMT was set to $V_{\text{op}} = 1050$ V, after a dedicated high-voltage scan [75] following standard recommendations [76]. This was achieved by monitoring the PMT dark count-rates, over a trigger threshold $V_{\text{thres}} = -30$ mV, as we gradually increase the applied high-voltage, from 550 V to 1800 V and in steps of 50 V [77]. The measured rate first rapidly increases, then stays on a broad plateau range. A suitable voltage supply is chosen around the transition knee between these two regimes. As voltage supplier, we utilize a CAEN-SY127 system [78] which also supplies the muon monitoring system described in Section 3.2.6. The hardware provides

^c q_{eff} depends on both the spectral transmission of the PMT window and the spectral response of the photocathode type [74].

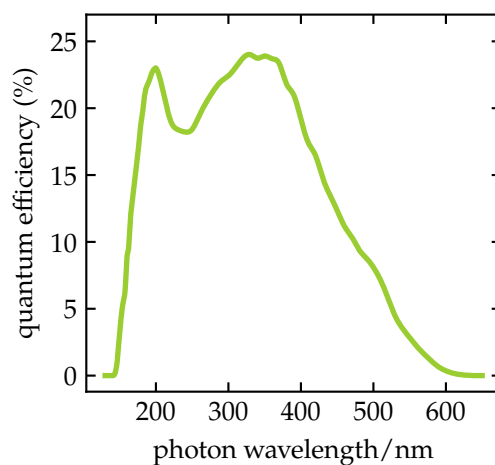


Figure 3.7: Quantum efficiency of the PMT as measured by the manufacturer for wavelengths from 200 nm to 630 nm, and extrapolated according to the published datasheet [73] from 150 nm to 200 nm.

an excellent voltage stability, with only an observed average fluctuation of $\leq 0.5\%$ over several months of measurement campaign.

The PMT is placed inside a designated FACT50 air-cooling module [79], as pictured in Fig. 3.6(b), which was originally intended to minimize background of thermal and thermionic^d origins. This device is, in principle, capable of reducing the physical temperature of the PMT by 50 K below room temperature. Nevertheless, for all measurements presented later, the cooling capability was disabled for essentially two reasons. First, the cooling process causes formation of ice on the electrode connectors, enhancing the surface conductivity of the latter and therefore provokes a drastic increase of leakage currents^e. Second, the setup would require an added double-layer of quartz glass, directly in front of the PMT window, to ensure thermal isolation. This would however modify the overall transmission spectrum of the window in front of the photocathode which, in turns, could possibly distort the quantum-efficiency curve of the PMT in an unforeseen way. Moreover, the additional volume of glass would likely produce many unwanted Cherenkov photons from direct muon hits. Therefore, decision was taken that for all measurement purposes, the FACT50 module would only serve as a convenient housing for the PMT and auxiliary, as a mounting structure for the detector arrangement which we describe in the next paragraph.

The camera support is mounted on top of a pillar at the location of the central spot, as seen in Fig. 3.8(a). We then placed the FACT50 housing on a motorized LTM60-150-HSM precision linear-stage [80] which can drive the camera laterally, *in* or *out* of the region where HP signal is expected. The camera can be driven up to a distance $d = 7.15$ cm away from the center of

^d The distinction is in whether photons or electrons are emitted due to temperature effect.

^e We recorded an increase of the background rate by a factor of 30 during trials [77].

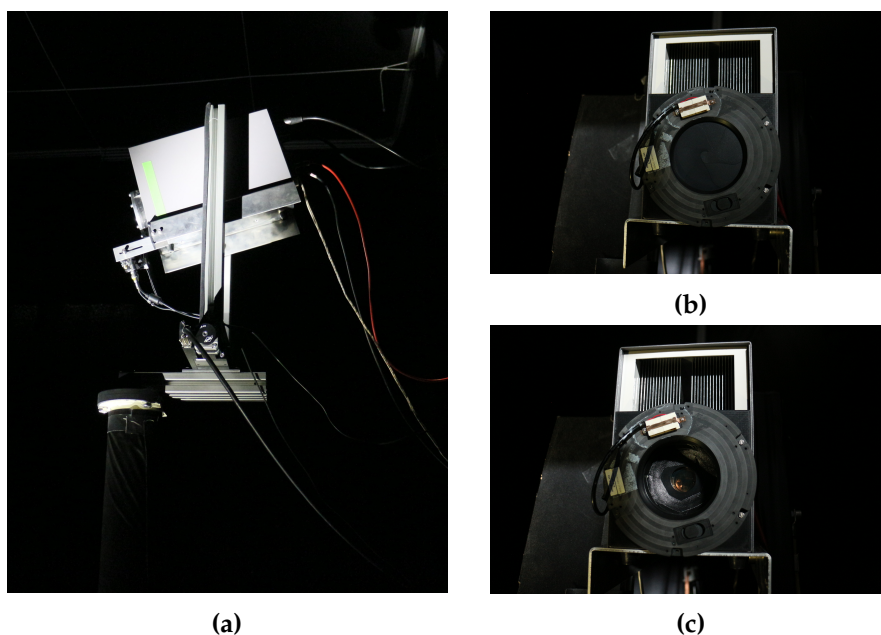


Figure 3.8: (a) Lateral view of the mounting structure of the PMT camera. In this figure, the mirror would be situated on the left. The figures on right show a close-up view on the front part of the detector, with the iris-shutter in *closed* (b) and *open* (c) modes, respectively.

curvature of the mirror, far enough to avoid any potential signal contribution and allowing us thus to measure the ambient background using the same detector. Because of the different imaging Field of View (FoV) at these two positions^f however, we added a felt baffle around the camera opening so as to obscure the scenery in the back. Since we also purposely employ a single PMT, we installed an automated NS65B optical shutter [81] in front of the PMT window in order to control its field of view (*open* or *closed*). This enables us to check for an eventual systematical drift between the *in* and *out* positions. The shutter has 6 Teflon-coated blades forming an iris diaphragm with a 65 mm aperture, as pictured in Figs. 3.8(b) and 3.8(c), and offering a perfect light-tightness. It is a sensible upgrade compared to the previously used customized Thorlabs MFF101 flipper [82] which only had an opacity^g of ~30 %.

^f Depending on the optical pathways, the PMT sees differently the reflection of the scenery behind its position.

^g In fact, the efficiency of the old shutter is possibly higher. However, a non-negligible memory of the PMT made the estimation non-trivial.

The shutter, the linear-stage and all other controllable parts of the experimental setup can be remotely accessed via network connection, through a dedicated slow-control unit, which also ensures data taking and storing and continuously provides the environmental status inside the experimental area. A complete description of this system can be found in [77]. Our

standard measurement uses a combination of the two measuring positions (PMT *in* or *out*) and the two optical modes (shutter *closed* or *open*).

3.2.3 Data Acquisition chain

Hardware

The output voltage of the PMT is digitized by a Picoscope oscilloscope 6404 series [83] which has an Analog-to-Digital Converter (ADC) with a resolution of 8 bits. The optimal voltage range of the Picoscope is set to ± 1 V at 50Ω input impedance, chosen to avoid occasional signal saturation. This corresponds to a voltage resolution of $\delta U = 7.874$ mV. The Picoscope can work either in external or internal-trigger mode. The external-trigger mode is useful for the SPE calibration procedure described in Section 3.2.4. For our standard run, the acquisition is systematically performed with an internal trigger, fixed to 8 ADC below baseline^h, which corresponds to a voltage dropping-threshold of ~ 63 mV on the output of the PMT. The baseline itself is estimated by capturing random traces before each acquisition and parsing them in a similar manner as described in the next section (see §. Software). The suitable threshold was determined after studying the triggering behavior of the Picoscope at given ADC threshold [77]. Then, for every trigger we capture a trace of 1000 bins before and after the trigger. The sampling period of the Picoscope is tuned to $\delta t = 0.8$ ns, or equivalently 1.25 GS/s. Hence each trace is 1.6 μ s long.

^h The PMT output signal is a negative pulse (see Fig. 3.9).

For all data-taking purposes, the measurement time is split into intervals of $\Delta t = 60$ s. There are two motivations for doing so. First, with our typical trigger rates of a few Hz, the Picoscope can only buffer traces captured during a limited amount of time before we read them out. This has the advantage that the acquisition can run uninterrupted and so no additional dead-time is introduced. Second, by keeping the duration of each measurement configuration short enough, we aim at limiting eventual systematical effects which could be introduced by switching between them. The DAQ implementation offers an excellent timing accuracy with an absolute uncertainty of ~ 1 ms, so that no additional corrections are necessary. This is a crucial requirement not to impact our sensitivity. Finally, all traces are stored in a computer together with information on the measurement mode (position of the PMT, status of the shutter, live time. . .) and the instantaneous environmental parameters (temperature, pressure) provided by the slow-control system. The formed dataset is then further analyzed off-line.

For some special runs, discussed later on, we also employ a Caen DT5751 digitizer [84] as alternative to the Picoscope. These runs were devised for studying the arrival time of events within the $\Delta t = 60$ s interval. Such a

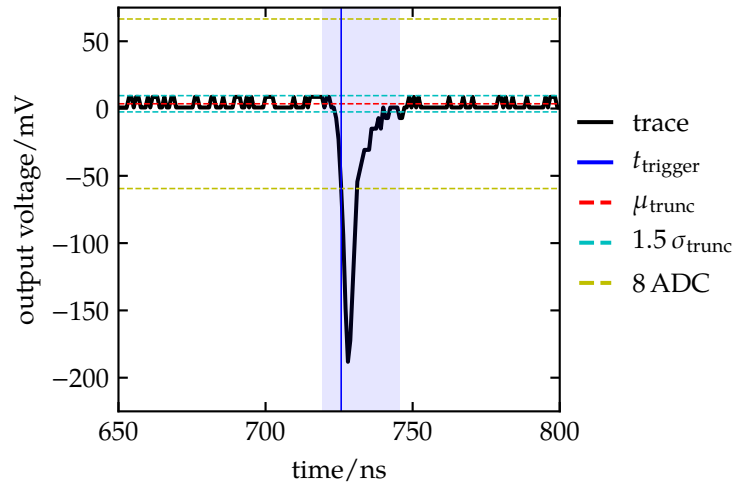


Figure 3.9: Example of a SPE pulse from the digitized output of the PMT and using default settings of the pulse-finder software. The black-line corresponds to trace captured by the Picoscope. The meaning of the other labels are explained in the text. We recall that the sampling time-period is $\delta t = 0.8$ ns and the voltage resolution is $\delta U = 7.874$ mV.

study is not possible with the Picoscope digitizer due to the absence of an absolute trigger-time tagging routine. Besides, it also enables us to perform a systematic cross-check on the overall performance of the DAQ system. The result yielded a relative trigger-rate difference of $\lesssim 3\%$ between the two digitizers, which can be explained by electronic noises. Unless otherwise stated and for all measurements presented later, the digitization of the PMT output is always accomplished with the Picoscope hardware.

Software

All stored traces are first parsed, off-line, with a dedicated pulse-finder software, after which, all identified pulses for each 60 s time bin are analyzed, then dumped again together with auxiliary information into an appropriate data format for more detailed analysis. The pulse-finder software runs in four steps. (i) A baseline estimator is executed over the whole trace, which then truncates out $p_0 = 4$ ADC around the baseline mode (most frequent baseline value). This gives us unbiased estimation of the mean μ_{trunc} and width σ_{trunc} of the trace baseline in ADC units. (ii) We prescribe an absolute trigger-threshold of $p_1 = 8$ ADC below μ_{trunc} , which matches the DAQ threshold. This consistency between software and hardware triggers is preferred in order to avoid over-counting pulses which would not have triggered the Picoscope but are still captured within the time window of an earlier trace. It also implies that no traces are empty. The position where the pulse strength

exceeds this threshold marks the trigger time t_{trigger} . (iii) Once a pulse signal is identified, the algorithm determines its length, i.e the pulse duration. This is done by scanning left and right of the trigger time, positions where the pulse strength falls below a certain threshold $p_2\sigma_{\text{trunc}} = 1.5\sigma_{\text{trunc}}$ relative to μ_{trunc} , for $p_3 = 7$ successive time bins. (iv) Each identified pulse is tagged and calibrated to extract other relevant parameters like its charge, amplitude, entropy, etc.

Hence, choices of the parameters p_0 and p_1 define the desirable strength of a pulse-like signal, while p_2 and p_3 determine its extent in time. The default settings of pulse-finder software are set to the above values, which are optimized from test runs to search for a SPE-like signal delivered by the FUNK PMT and in accordance with specifications of the latter [73]. A typical SPE signal found using these default parameters is shown in Fig. 3.9.

3.2.4 Single Photoelectron calibration

Given the single-photon like nature of the HP signal and its expected feeble power in the eV range, a fundamental prerequisite for FUNK is to achieve a precise and reliable SPE discrimination. As we shall demonstrate, standard techniques involving selection on the pulse charge or amplitude are not satisfactory enough. Therefore, we propose a new technique based on the pulse width and entropy.

Flasher runs

First, we performed a series of calibration runs by using a faint flashing blue-LED source. This enables us to study the typical properties of a SPE signal delivered by the PMT. The intensity and frequency of the LED flasher could be easily adjusted with an existing control box. Then, for each specific intensity we set the LED to flash 5000 times at a determined frequency of 10 Hz. In addition, each flash synchronizes an external trigger which signals the Picoscope to capture a trace of 5120×0.8 ns. Since the LED is rather positioned at an arbitrary place, this triggering mechanism provides us with an estimate of the average time during which a photon is liberated by the LED, get randomly bounced around, and finally being detected by the PMT. That is, we can discriminate between photons originating from the flasher device and coincidental triggers in the PMT output trace. For lower intensity of the LED flasher, it is unlikely to capture multiple photons arriving at the same time. Therefore, we typically observe a clean SPE signal, as illustrated in Fig. 3.10(a). As the intensity of the LED gradually increases and increasingly more photons are emitted, we begin to observe multiple photons reaching the PMT photocathode almost simultaneously and thus

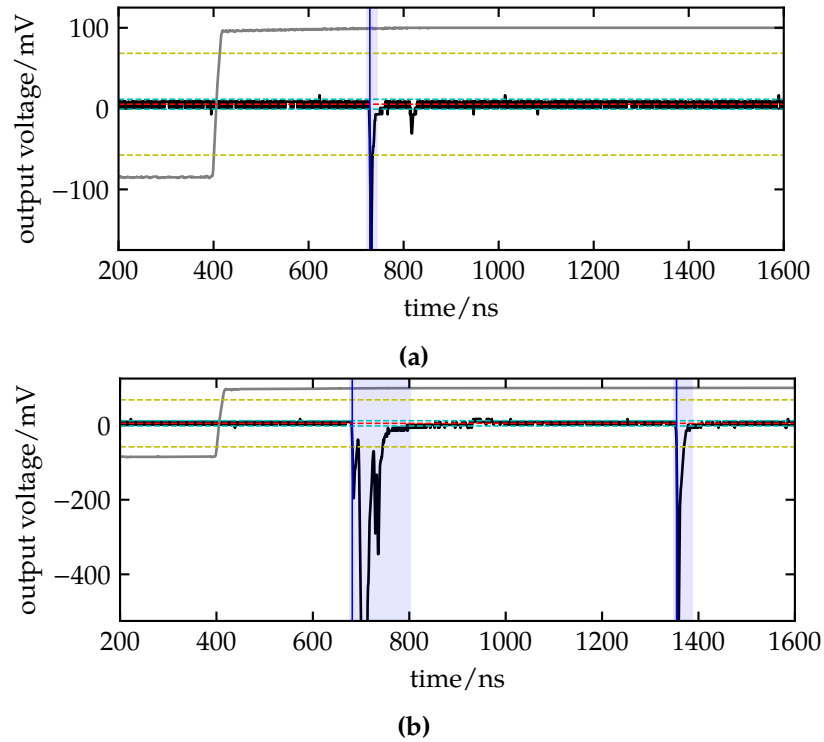


Figure 3.10: Example of typical events captured by the Picoscope for two different settings of the LED flasher, matching the red (a) and blue (b) lines in Fig. 3.11 (see text for details). The black and gray lines are the traces of the PMT output-voltage and the external-trigger signal, respectively. For the latter, the input voltage has been arbitrarily rescaled for plotting purpose. The other elements of the plot are the same used for our standard event finder, see Fig. 3.9.

yielding large pulse and afterpulse signals, as seen in Fig. 3.10(b). These multiple photon events, as later on being associated to shower events, are what we aim to discard with our quality cuts.

The results from these flasher runs can be summarized in Fig. 3.11, where we plotted the distribution of the collected anode charge Q against the intensity of the LED flasher in arbitrary units. We observe that the anode charge begins to develop a main peak at $Q \approx 10^8 e$. The main peak then slowly moves to a higher charge, leaving place to some wiggles at relatively lower charges, and eventually saturatesⁱ at $Q \gtrsim 10^9 e$ as more photons are simultaneously captured within a narrow time-window. This behavior is expected, and thus, these measurements show evidence that the PMT is indeed working properly. In fact, the charge distribution admits some interesting substructures, which are inherent to the origins of the pulses themselves. These will be further explained when we analyze *real* data

ⁱ The saturation is an artifact of the limitation of the voltage-range to ± 1 V.

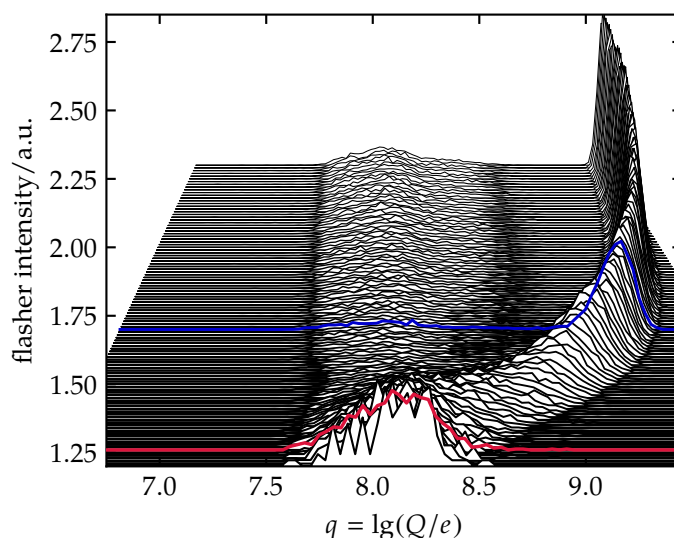


Figure 3.11: Development of the charge Q collected at the anode of the PMT as function of intensity of the LED flasher in arbitrary units. The red line corresponds to the settings used for the SPE study, while the blue line indicates a higher settings used for various illustrations in other plots.

in Section 5.2. In the present case, the calibration data is mostly driven by the flasher, i.e. most of the captured photons originate from the LED. This is why we essentially observe one single-peak in the charge distribution. In the same figure, we highlighted two lines in red and blue. The former corresponds to a particular setting of the LED flasher chosen for SPE study, and the latter indicates a higher value of the flasher intensity used for comparison.

SPE study

In this section, we focus on the SPE response of the detector. One straightforward but expensive way to achieve that is by employing a single-photon source. Another way, which we prefer, is to use a faint light source and apply a certain probability of capturing photons in order to mimic a single-photon emitter. The charge scan shown in Fig. 3.11 already hints where to look at. We set the intensity of the LED flasher to an optimal setting chosen so that the PMT only sees photons $\lesssim 20\%$ of the time and $\gtrsim 95\%$ of the non-empty captured traces only contain one single-pulse. The SPE phase space is then refined by performing a calibration run with this optimal setting. During this measurement, we collected $\sim 4.86 \times 10^5$ pulses which we treated as follows.

Two preliminary cuts are first applied, as presented in Fig. 3.12. (i) We require that the pulse rise-time, defined as $t_{\text{rise}} = t_{\text{mean}} - t_{\text{trigger}}$, must be positive. Here, t_{mean} denotes the time bin corresponding to the mean value

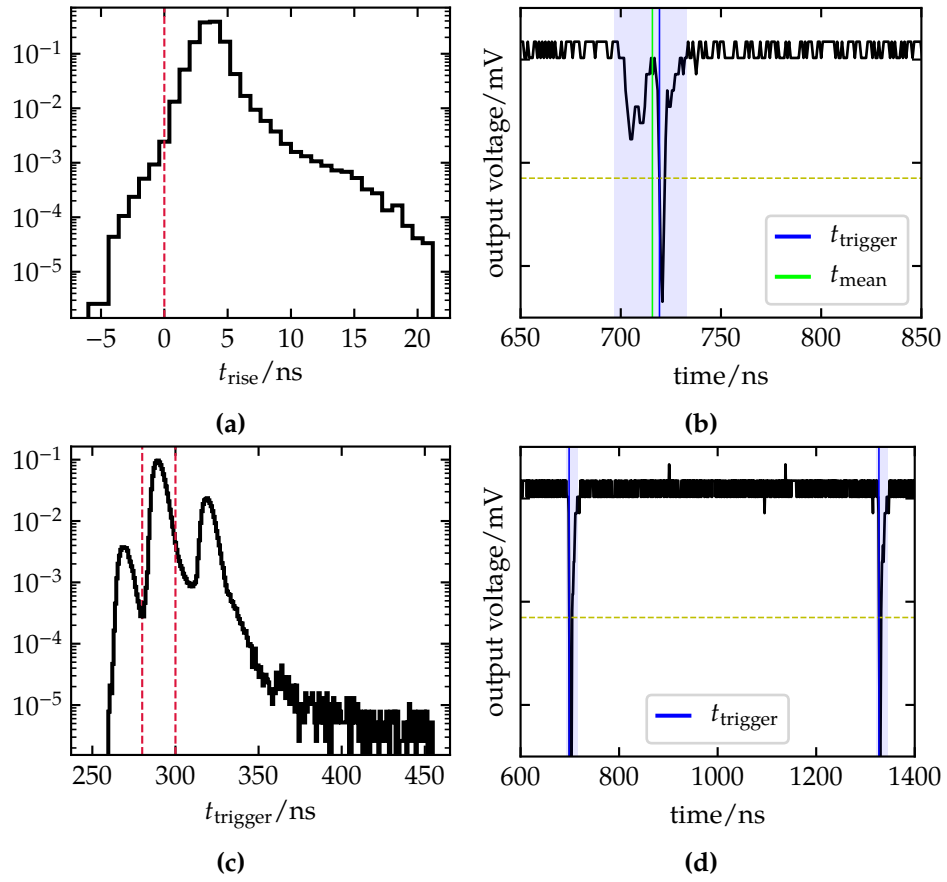


Figure 3.12: (a) Distribution of the pulse rise-time t_{rise} . (b) Illustration of a case where $t_{\text{rise}} = t_{\text{mean}} - t_{\text{trigger}}$ becomes negative, because of the pulse shape. (c) Distribution of the trigger time t_{trigger} , relative to the LED flasher signal (which goes off at ≈ 400 ns of the trace window, as seen in Fig. 3.10). (d) Example of a trace containing multiple pulses. The first one is likely from the LED, whereas the second one could be a coincidental hit.

^j The formal definition is of the pulse treated as a time distribution^j and t_{trigger} is the trigger time. This is intended to suppress spurious triggers possibly related to baseline fluctuations. (ii) We impose a strict arriving time-window of photons, with $280 \leq t_{\text{trigger}}/\text{ns} \leq 300$, relative to the LED flasher signal, in order to discard other coincidental triggers. These two cuts successively clear out 0.2% and 25.4% of the dataset, respectively. From the resulting dataset, we shall now identify pulses which are most likely associated to single-photon hits.

Standard event selection

A standard technique commonly used consists of fitting the distribution of the anode charge Q with an appropriate statical model. This technique however does not allow for an event-by-event discrimination, but rather gives an estimate of the expected total number of SPE over a certain background. There are many state-of-the-art models of SPE statistics in the literature [85–87], which are derived from first principles. These models assume that the number of secondary electrons generated by a primary electron emitted by the photocathode follows a certain probability distribution (e.g. Poisson), and for simplicity, the amplification process is taken uniform across each dynode stage^k.

The difficulty here is multiple: accounting for eventual irregularities across the dynode surfaces, non-linearities in the applied voltage divider, poor amplification due to sub-optimal trajectories of photons and electrons, etc. All of these effects result in a non-Poissonian and non-trivial cascade multiplication of electrons. Besides, there appears to be a wide variation on the shape of SPE spectra observed with various classes of PMTs [86]. Suffice it to say that there is no preferred model for the charge spectrum and for most practical cases, the description is at best semi-empirical. For example, using a Gaussian distribution [89] or a Polya distribution [90], etc. A full description of the collected charge also necessitates a proper modeling of the noise and dark current spectra, choices of which again rely upon ansatz.

It should be clear that cooking-up an arbitrarily complicated model lacking a physical motivation is not a desirable method. On the other-hand, the preselected calibration dataset should not be blindly used as an empirical template to estimate the *full* SPE statistics since it still contains both background pulses and contamination from poorly-amplified multiple photoelectrons. Nevertheless, for estimating the average gain^l $\langle G \rangle$ of the PMT it is enough to fit the main peak of the charge distribution from the low-light calibration run, as shown in Fig. 3.13. We obtain $\langle G \rangle = 1.12 \times 10^8$. The standard deviation of the gain is of the same order of magnitude. It should be noted that the PMT gain is rather sensitive to small fluctuations in the applied high-voltage. The latter is however well under-control as already mentioned in Section 3.2.2.

^k Such a statistical model is known as Galton-Watson branching process [88].

^l The gain is a random variable.

SPE phase space

Our proposed technique to estimate the full SPE statistics is based on a two-fold selection criteria applied on event-by-event basis: the pulse width σ_t and the pulse information-entropy S . These two quantities are computed by converting each pulse to a probability mass function p along the time

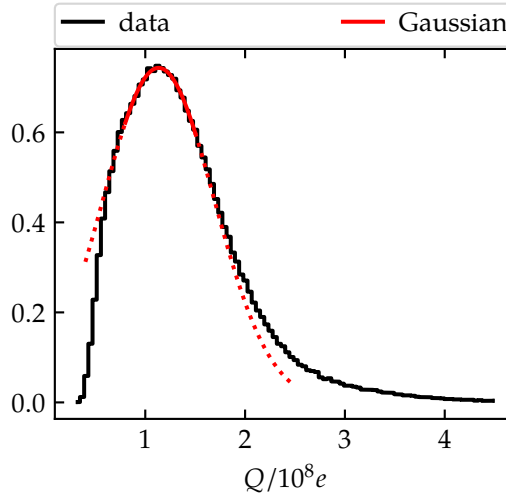


Figure 3.13: Distribution of the anode charge Q obtained from the calibration run with the optimal setting of the LED flasher. The red line is a Gaussian fit used to estimate the PMT gain, where the solid part indicates the fit range. The dotted part is to illustrate an obvious mis-modeling of the full extent of the spectrum, as discussed in the text.

axis t , defined as $p(t=t_i) = h_i$, where h_i is the pulse amplitude after proper normalization such that $\sum_i h_i = 1$. The time t is viewed as a random variable which takes discrete values t_0, t_1, \dots such that $t_{i+1} - t_i = \delta t$, where $\delta t = 0.8$ ns is our sampling period. In other words,

$$p(t=t_i) = p_i = \begin{cases} h_i & \text{if } t_{\text{begin}} \leq t_i \leq t_{\text{end}} \\ 0 & \text{otherwise} \end{cases}, \quad (3.5)$$

where t_{begin} and t_{end} are the beginning and ending of the pulse, respectively. The latter are evaluated according to the parameters of the pulse-finder software described in Section 3.2.3. The pulse width is then defined as the standard deviation of this time distribution. Similarly, the information entropy is calculated using Shannon's definition. That is,

$$\sigma_t = \sqrt{\langle t_i^2 \rangle - \langle t_i \rangle^2}, \quad (3.6)$$

$$S = - \sum_i p_i \ln p_i. \quad (3.7)$$

These two criteria were chosen to (i) avoid direct cuts on the pulse charge or amplitude whose standard deviations are comparable to their means — (ii) suppress long-duration pulses which are likely associated with multiple photoelectrons coming from non-HP sources. The combination of the two provides us with a strong discrimination power on the pulse shape. Indeed,

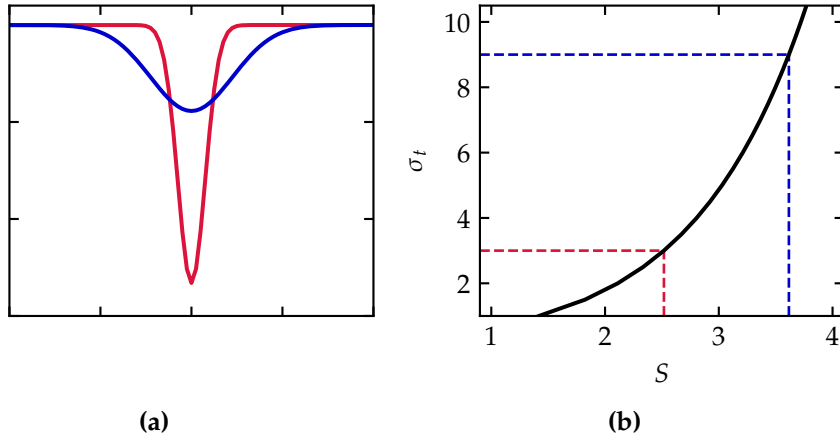


Figure 3.14: (a) Illustration of two pulses with the same charge but different shapes. (b) Pulse discrimination in the (σ_t, S) phase space. The dashed lines indicate the respective values of these quantities for the pulses drawn in (a) with the same colors.

the stochastic nature of photoelectron paths, from the photocathode and across the dynode structure, causes a dispersion of their arrival times at the anode and results in a certain shape of the output voltage. The typical width of a SPE signal is characteristic of the PMT timing performance. It depends upon several parameters such as the number of dynodes and their geometries, the voltage-divider design, etc. Multiple photon hits would have a more spread signal compared to a single photon hit, independently of the gain efficiency. Hence why a selection on the pulse width is a good choice. The informational entropy is intended to supplement this cut by quantifying the overall shape of the pulse.

To illustrate these statements let us take as an example, pulses with a Gaussian shape in time. Let us consider a family of Gaussian distributions $f(t, \mu_t, \sigma_t)$ with fixed mean μ_t but varying standard deviations σ_t , and let us evaluate at discrete times t_i , values of $p_i = f(t_i, \mu_t, \sigma_t)$ in a regular unit-step δt such that $t_{i+1} = t_i + \delta t$. Then, we renormalize the value of the probability density at each time t_i such that $\sum_i p_i = 1$ so as to have a proper probability mass function^m. This discretization procedure is approximately equivalent to the following definition,

$$\begin{aligned}
 p(t=t_i) = p_i &= \int_{t_i - \delta t/2}^{t_i + \delta t/2} dt f(t, \mu_t, \sigma_t) \\
 &= \mathcal{F}\left(\frac{t_i - \delta t/2 - \mu_t}{\sigma_t}\right) - \mathcal{F}\left(\frac{t_i + \delta t/2 - \mu_t}{\sigma_t}\right), \quad (3.8)
 \end{aligned}$$

^m The information entropy is formally defined for discrete distribution only. Although, extensions exist.

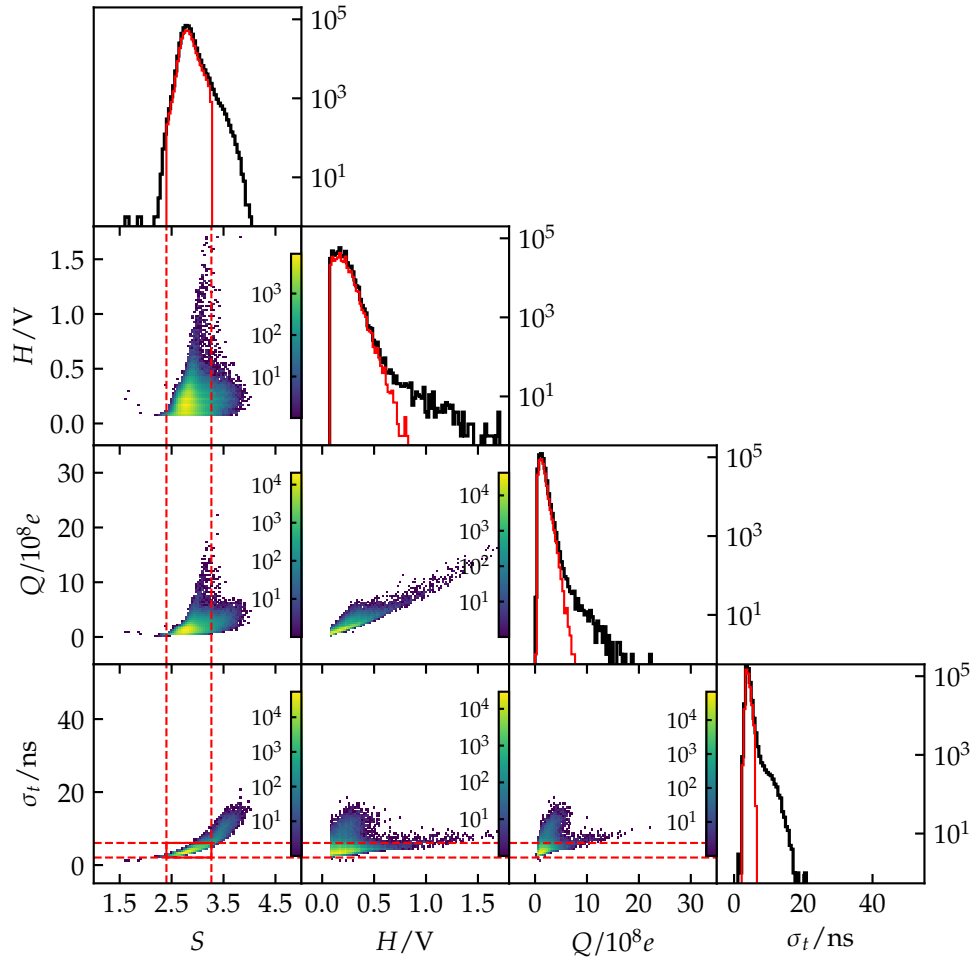


Figure 3.15: Distributions of the pulse width σ_t , entropy S , amplitude H , and charge Q , and density plots for each pair of variables showing their correlations. The red lines shows the ROI defined in the (σ_t, S) phase space, with $2.066 \leq \sigma_t/\text{ns} \leq 6.061$ and $2.400 \leq S \leq 3.266$ (see text for details). We also show how the distributions are affected after event selection.

where \mathcal{F} is the standard normal cumulative distribution. Thereafter, the calculation of the information entropy for each standard deviation is trivial.

In Fig. 3.14(a), we plotted two pulses with standard deviations $\sigma_t = 3$ and 9 (in arbitrary units), and whose time distributions satisfy Eq. (3.8). The corresponding entropies are estimated to $S = 2.51$ and 3.61, respectively. Since the areas under both curves are the same, these illustrate cases where we observe two pulses having the same charge but one being relatively spread in time as could be the result of poorly-amplified multiple photoelectrons. Since the information entropy only depends on the probability values, it is in a sense sensitive to the pulse shape. For our Gaussian approximation, the dependence between the pulse width and its entropy is plotted in Fig. 3.14(b), in case of integer sampling times.

Finally, we construct our ROI which most likely contains SPE signals by selecting 3 standard deviations around the respective means of the truncated distributions of the pulse widths and entropies obtained from the SPE calibration data run, and after applying the preliminary cuts explained in Fig. 3.12. This construction is presented in Fig. 3.15, where we plotted the distributions of relevant pulse quantities, namely their widths σ_t , their entropies S , their amplitudes H and their charges Q . All these distributions peak well around the SPE region, which is of course expected since we used the optimal settings of the LED flasher. In Fig. 3.16, we plotted the distributions of the same quantities but with a different setting of the LED flasher, as indicated in Fig. 3.11. This allows us to observe the movements of the main peaks towards a larger width, higher entropy, amplitude, and charge because of the increased probability of capturing more photons at the same time. Furthermore, we can observe the onset of a clear separation between single and multiple photons events.

In the same figures, we also plotted the 2D density scatter-plots for each pair of variables in order to display their correlations. There are two noticeable correlations, between (Q, H) and (σ_t, S) . The former is obvious since $Q = \int dt H(t)/Z$, where Z denotes the input impedance of the Picoscope digitizer. The correlation between (σ_t, S) can be understood from our discussion above on the pulse shape. Likewise, the *noisy* structures seen in the other distributions reflect on our argument that pulses with similar charges or amplitudes may have quite different shapes.

Finally, it is also instructive to apply the so-defined ROI to our series of flasher runs, in order to investigate its efficiency with varying intensity, i.e. the ratio between number of SPE events and detected pulses. The result is shown in Fig. 3.17, where we can see that the cut efficiency immediately drops as we increase the intensity of the LED flasher, which is again expected. After reaching a certain level however, the efficiency appears to increase again.

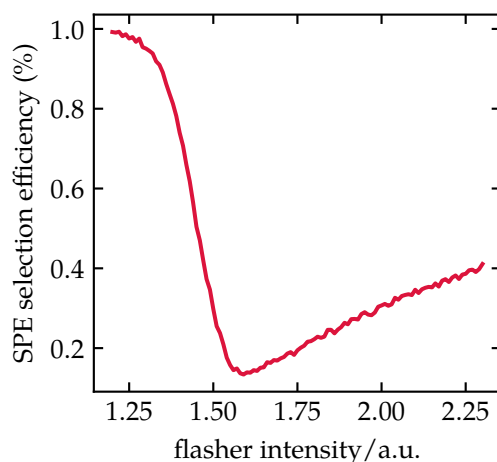


Figure 3.17: Efficiency of the quality cut explained in Fig. 3.15 directly applied to the flasher data runs (details are given in the text).

This is because of the subsequent increase in the number of afterpulses, whose shapes could become indistinguishable from a real SPE. In principle, afterpulses can be disregarded by means of a time correlation analysis. Nonetheless, for the typical rate of exposure recorded during our standard run and thanks to the relatively high trigger threshold, they only amount to a few percents. We shall come back to that in Chapter 5.

3.2.5 Temperature and Pressure monitoring

The FUNK experiment demands an absolute knowledge of the environmental conditions in which all measurements are performed, as it enables us to potentially identify different sources of background. This includes the temperature and pressure of the experimental facility. These quantities are uninterruptedly monitored at all times and independently of the main measurements. We recall that the FUNK setup is arranged within a $\sim 100 \text{ m}^3$ light-tight restricted zone, accommodated inside a windowless experimental area about 22 times larger. This facility is air-conditioned. In addition, the thick concrete walls provide a good thermal isolation. As such, the experiment benefits from an excellent temperature stability.

We placed two cross-calibrated high-precision DS18S20 sensors [91] to survey the temperatures of the room and the PMT enclosure. The result of a monitoring over a period of more than ~ 1.5 year is shown in Fig. 3.18. For this entire data, we can read that the maximal temperature difference does not exceed 4°C . For a typical one-month run, the temperature standard deviation recorded with both sensors is usually less than 0.2°C .

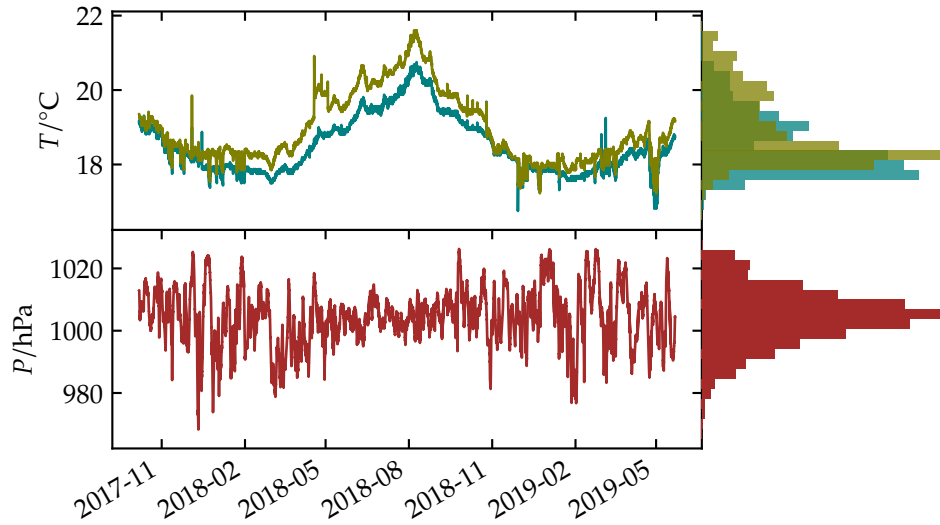


Figure 3.18: Temperatures (in green for the FACT50, in blue for the experimental hall) and atmospheric pressure monitored over a period of roughly 1.5 year. On the right are shown their distributions.

To monitor the atmospheric pressure, we used a BMP180 sensor [92]. The data is also shown in Fig. 3.18 for the same time span. Moreover, we found that the pressure data are well in agreement with outdoor measurements kindly provided by the *Institut für Meteorologie und Klimaforschung* (IMK, KIT). Details of the installation and the monitoring system are given in [77].

3.2.6 Muon monitoring

In response to the requirements of the FUNK experiment, we also monitor the rate of muons penetrating into the experimental area. In Section 4.3, we will evaluate the expected flux of muons from Cosmic Ray (CR) air-shower propagation, in order to conform with the measured data and infer rate of Cherenkov radiation produced by these CR muons.

Our muon monitoring system consists of three scintillator paddles (see Fig. 3.19), each comprised of scintillator bars connected through a light guide to a PMT. The geometries of the paddles are sketched in Fig. 3.20(a). The outputs of the built-in PMTs are connected to discriminators and coincidence counters which are read-out every 60 s, in parallel with the FUNK slow-control unit. The calibration of the scintillator paddles were done in [77] and their efficiency were estimated to $\geq 96\%$. The structure of three paddles is arranged in a such way to obtain both temporal and spatial coincidences of muons. The former corresponds to coincidence counting of two paddles stacked vertically one on top of the other (“vertical coincidence” from

single-muon track) and the latter is obtained from coincidence counting of the bottom paddle and one placed horizontally next to it (“horizontal coincidence” from muon bundle).

Measurement

The typical registered rates are 20 Hz for the vertical coincidence and 1 Hz for the horizontal coincidence, with a typical standard deviations of 5 % and 10 %, respectively, for daily datasets. These indicate that most muons arrive as single tracks rather than as bundles. In Fig. 3.21, we plotted the muon fluxes recorded over a period spanning more than 1.5 year, and where we can see a relatively stable variation of the rates. There is also indication of seasonal modulations. In particular, a well-known annual modulation, in connection with atmospheric variations, is visible.

Let us make a few comments on this. The annual modulation can be correlated [93, 94] or anti-correlated [95, 96] with the weighted average of atmospheric temperatures evaluated from the top of the atmosphere down to sea level or the observational level. The sign of the correlation depends somewhat on the *vertical depth* of the detector site, or put another way, on the energy spectrum of the observed muons.

The argument is that a thermal expansion of the atmosphere would increase the geometrical path length of muons and thus decreases the survival probability of low energy muons, that are predominantly observed by detectors at sea level and above. In contrast, high energy muons are less likely to decay in the atmosphere and they can penetrate deeper underground. In this case, the temperature effect becomes more relevant at the production level. Higher temperature means decrease in the air density, which implies a lower interaction rate and thus a higher probability for charged pions and kaons to decay into muons [97].

Likewise, there is also some dependence on the atmospheric pressure. As we shall see in Section 4.3, most of muons at sea level are in the GeV range and they can easily penetrate the ~ 2 m thick concrete shielding of the experimental area. In Section 5.2.4, we will find that our measurement of the rate of vertical muons is actually slightly anti-correlated with the pressure data, which is indeed expected.

Vertical muons

For future reference, a useful quantity is the integral intensity of vertical muons, $\mathcal{I}_{v,\mu}$. This represents the number of muons arriving at zenith angle $\vartheta \approx 0$, within a solid angle $d\Omega$ and traversing a surface element dA . As shown

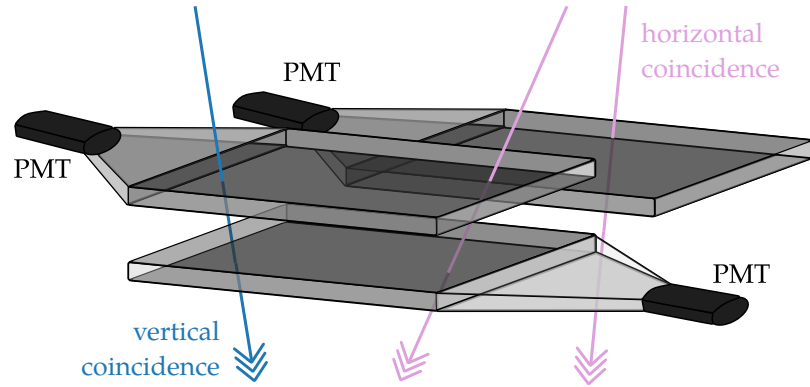


Figure 3.19: Sketch of the muon monitoring system of FUNK.

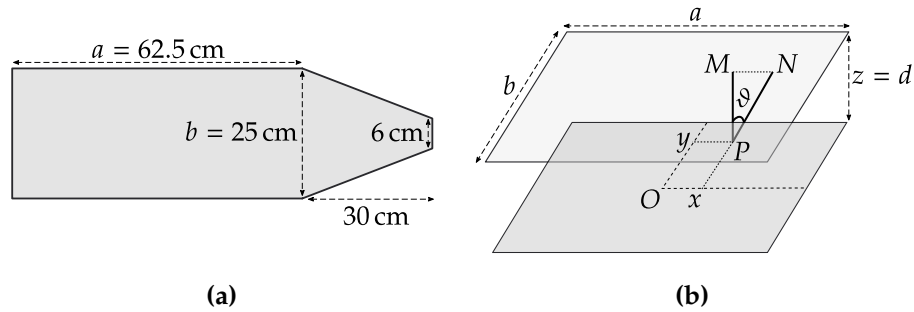


Figure 3.20: (a) Geometry of the scintillator paddles. (b) Geometrical acceptance of a two-fold coincidence telescope separated by a distance $d = 2.5$ cm.

below, we can well estimate $\mathcal{I}_{v,\mu}$ from the measured vertical-coincidence rate.

The first step is to evaluate the geometrical acceptance of the two-fold scintillator paddles, stacked vertically, and separated by a distance $z = d$. This corresponds to the field of view $\int dA d\Omega$, that is geometrically allowed so the particles traverse both paddles. The situation and all relevant dimensions are sketched in Fig. 3.20. We use *primed* coordinates for points located in the plane of the top paddle and *unprimed* coordinates for those in the bottom one. Let us consider a surface element dA' centered around a point N such that $\mathbf{MN} = (x', y', 0)$, where M is the orthogonal projection of a point $P(x, y, 0)$ in the bottom surface, onto the top surface. The solid angle $d\Omega$ subtended by dA' and seen from the point P is given by

$$d\Omega = dA' \frac{\cos \vartheta}{|\mathbf{PN}|^2} = dx' dy' \frac{d}{(x'^2 + y'^2 + d^2)^{3/2}}, \quad (3.9)$$

where $\cos \vartheta = d/|\mathbf{PN}|$. It follows that

$$\int dA d\Omega = \int_{-a/2}^{a/2} dx \int_{-b/2}^{b/2} dy \int_{-(a/2+x)}^{a/2-x} dx' \int_{-(b/2+y)}^{b/2-y} dy' \frac{d}{(x'^2 + y'^2 + d^2)^{3/2}}. \quad (3.10)$$

For our setup, we findⁿ $\int dA d\Omega = 7254 \text{ cm}^2 \text{ sr}$.

Next, we assume that for non-vertical muons, the integral intensity $\mathcal{I}_\mu(\vartheta, \varphi)$ falls as $\cos^2 \vartheta$. This is a valid approximation for zenith angles $\vartheta \lesssim 70^\circ$ and for muons in the GeV range [98]. We note that there are other empirical parametrizations (see e.g. [99]) which describe the full arrival zenith-angles of muons. Nevertheless, that is less relevant for a first estimate. The expected rate of muons ϕ_μ , for horizontal detectors (also see Appendix A), is then given by

ⁿ Without this geometrical consideration, we have $\int dA d\Omega = 9817 \text{ cm}^2 \text{ sr}$.

$$\begin{aligned} \phi_\mu &= \int dA d\Omega \cos \vartheta (\mathcal{I}_{v,\mu} \cos^2 \vartheta) \\ &= \mathcal{I}_{v,\mu} \int dx dy dx' dy' \frac{d^4}{(x'^2 + y'^2 + d^2)^3}. \end{aligned} \quad (3.11)$$

It is now easy to invert the last equation and find $I_{v,\mu}$. Evaluating the muon rate from our 1.5 year data, we obtain

$$\mathcal{I}_{v,\mu} = 8.93 \times 10^{-3} \text{ cm}^{-2} \text{ sr}^{-1} \text{ s}^{-1}. \quad (3.12)$$

We will resume these discussions in Chapter 4.

3.3 A glimpse into FUNK++

Let us now direct our attention to another direction of the FUNK experiment, in the future. We name it FUNK++. As we pointed-out in Section 2.4.4, the experimental setup is not suitable for frequencies beyond far-UV, because of the poor reflectivity of the mirror at these frequencies. Besides, as seen in Fig. 2.1, there are tight bounds coming from astrophysical and cosmological constraints. Other direct detection experiments, in particular involving HPDM ionization, are also providing very competitive limits in this regime [57, 59]. For FUNK++, the natural direction is then towards lower HP masses, and in essence, we just change the detector. As a first step, we may acquire a readily available commercial antenna in the GHz band and perform a broadband scan *in/out*. In the terahertz regime, there exist also excellent detectors with some reaching the quantum limit. In the following, we briefly study these options for FUNK++.

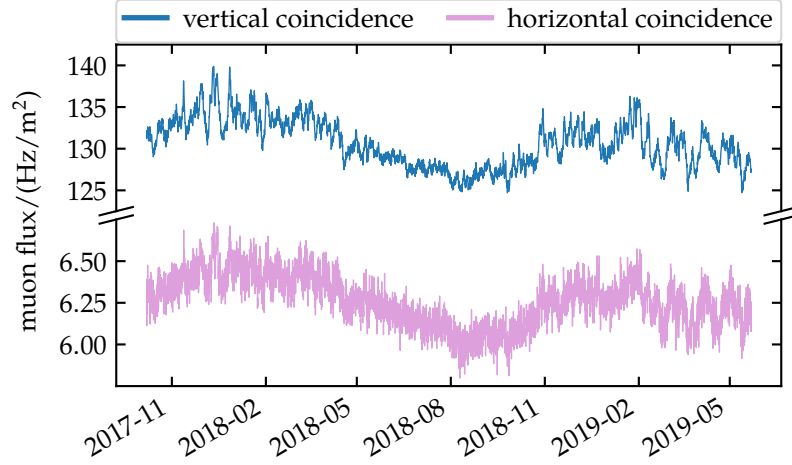


Figure 3.21: Fluxes of muons from “vertical coincidence” (single muons) and “horizontal coincidence” (muon bundles), monitored inside the FUNK experimental facility during roughly 1.5 year. The rates are averaged over 3 h.

3.3.1 Sensitivity equation

The FUNK++ experiment will be setup to search for HPDM with masses in the (sub)-meV ranges, corresponding to microwave frequencies. In the radio and microwave spectrum, the minimum detectable power P_{det} — conveniently defined in units of equivalent noise temperature — is determined by the radiometer equation (see Appendix B.3). This depends on the system temperature of the detector arrangement, the (predetection) bandwidth $\Delta\nu$ and the (postdetection) integration of time τ . In our case, the relevant equation is given in Eq. (B.24), which translates to

$$P_{\text{det}}/W = 1.5 \times 10^{-20} \left(\frac{k_{\text{rec}} T_{\text{rec}}}{100 \text{ K}} \right) \left(\frac{\Delta\nu}{1 \text{ MHz}} \frac{10 \text{ h}}{\Delta t} \right)^{1/2}, \quad (3.13)$$

at a Signal-to-Noise ratio of 1, and where $\Delta t = n\tau$ is the total integration time for n independent averaged measurement. k_{rec} is a $\mathcal{O}(1)$ factor which depends on the details of the receiver and set to 1 for simplicity.

To gain some optimistic sensitivity estimates for FUNK++, we assume that the system temperature is driven by the receiver noise temperature. This means, we assume that the experiment has sufficiently taken care of reducing contributions from external noise sources such as thermal background and

other microwave pollutions. For now, inserting Eq. (3.13) into Eq. (2.53), we obtain our sensitivity to the mixing parameter, such that

$$\chi = 1.3 \times 10^{-12} \left(\frac{k_{\text{rec}} T_{\text{rec}}}{100 \text{ K}} \right)^{1/2} \left(\frac{\Delta\nu}{1 \text{ MHz}} \frac{10 \text{ h}}{\Delta t} \right)^{1/4} \left(\frac{A/|\eta|^2}{\text{m}^2} \right)^{-1/2} \\ \times \left(\frac{\langle \cos^2 \alpha \rangle}{2/3} \right)^{-1/2} \left(\frac{\rho_{\text{CDM}}}{0.3 \text{ GeV cm}^{-3}} \right)^{-1/2}. \quad (3.14)$$

In addition to the requirement of a low T_{rec} that is definitely more important, Eq. (3.13) suggests that smaller bandwidths and longer integration times are needed to measure smaller powers and thus achieve a better sensitivity. Moreover, as seen in Eq. (B.17), the spectral line of the HP signal, with a peak at $m_{\tilde{\gamma}}$, has a narrow broadening of $\sim 280 \text{ kHz}/(m_{\tilde{\gamma}}/\text{meV})$. This is easily within the resolution of most spectrometers, so that a first broadband scan is technically only limited by the full detector bandwidth.

3.3.2 Sensitivity limits

For consideration of the detection technique, one option is to employ a heterodyne receiver, as commonly practiced in radio and microwave detection. The heterodyne principle is explained in Appendix B.3. Basically, the idea consists first of coupling — via a mixer — the signal received by the radio antenna to a reference local oscillator with known frequency. The mixer generates a new signal whose frequency corresponds to the difference between the two inputs. This new signal is then amplified and analyzed. Most importantly, this down-conversion in frequency domain enables the response time of the receivers to adapt with relatively higher input-signal frequencies ($\sim \text{THz}$). Commonly used mixers include Schottky diodes, Superconductor-Insulator-Superconductor (SIS) junction, and Hot Electron Bolometers (HEB). For our estimates, we consider the first two types. Moreover, we suppose that the receiver noise temperature is dominated by contribution from the mixer, which is conceivable in the most optimized configuration of the back-end of the detector setup.

The noise-temperature performance of the double sideband^o mixers, T_{DSB} , are shown in Fig. 3.22. We note that in this figure, the Schottky diodes operate at room temperature while the HEB and SIS are at cryogenic stages (77 K and 4 K, respectively). As a first start, we can use commercially available Schottky diodes as they have minor complexities and wider frequency-band coverage. The projected sensitivities obtained, for the setups described below, are shown in Fig. 3.23. The figure-of-merit of the mixers are taken from Fig. 3.22.

^o This means that both sidebands (difference and sum of input frequencies) are present in the intermediate or transmitted frequency.

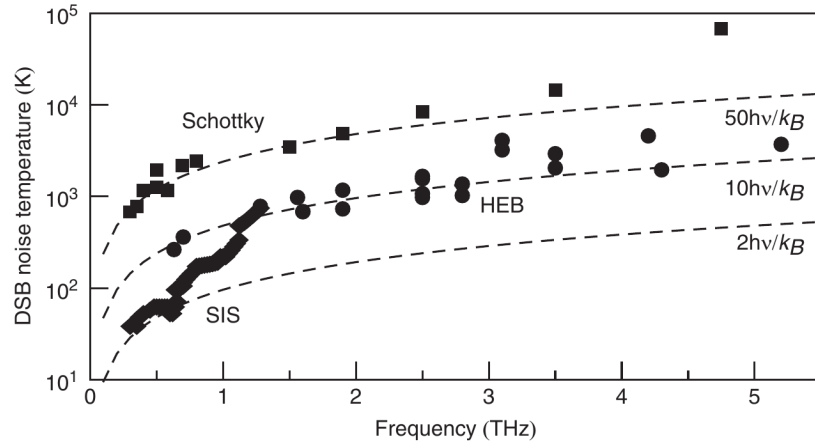


Figure 3.22: Figure-of-merit of the double sideband (DSB) noise temperatures of commonly used front-end mixers in radio and microwave receivers: Schottky diodes (square markers), Supercoductor-Insulator-Superconductor junction (SIS, diamond markers), and Hot Electron Bolometers (HEB, circle markers). Figure was taken from [100].

- Frequency coverage: 0.1 THz – 2.5 THz, with $T_{\text{rec}} \approx T_{\text{DSB}} = 50h\nu/k_B$ (Schottky diode). In this frequency band, the natural width of the HP line is $\gtrsim 120$ kHz. We considered the feasibility of the measurement with a Fast Fourier Transform Spectrometer [101], which offers a total of 2.5 GHz instantaneous bandwidth with a resolution of $\Delta\nu = 88$ kHz per channel. We assumed a total integration time of 3 h, in steps of 1 s. Using these parameters, we obtain the sensitivity limit labeled “Schottky diode” in Fig. 3.23.

A first measurement from an experiment performed in Tokyo, searching for meV HPs with a similar technique, was reported in [62] and plotted in the same figure. The limit from this experiment is clearly 3 to 4 orders of magnitude worse than our current estimate in the same mass range. Besides a certain advantage due to the size of our mirror, this large difference is purely due to the level of noise measured by the Tokyo experiment. Their typical noise power is about 10^{-13} W, whereas our optimistic evaluation leads to a detectable power of about 7 order of magnitude smaller.

Naturally, our sensitivity is also limited from the back-end of the detection chain, which was not considered here. Nevertheless, measuring such a low power is certainly challenging but seems feasible [102]. We also note that the authors of [62] did not report a study on the possible residual noise (after shielding) in their experiment.

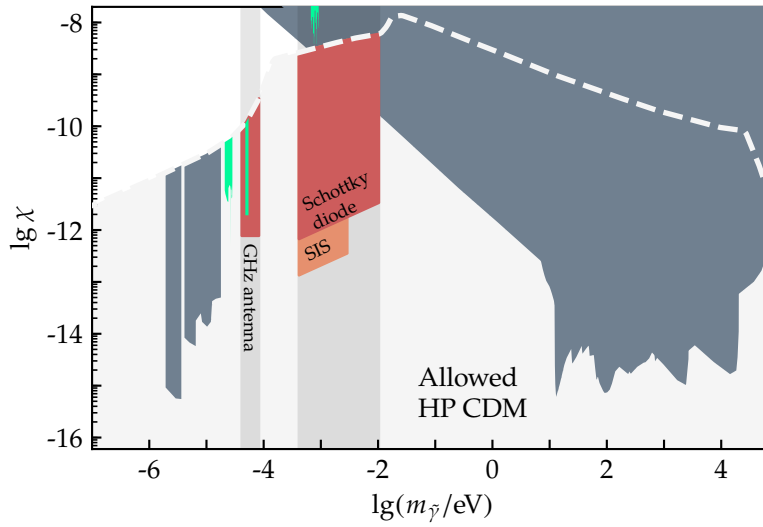


Figure 3.23: Projected sensitivity of the FUNK++ experiment for gigahertz and terahertz detection. The dark-gray area corresponds to the disfavored HP parameter space, by combining observational and experimental constraints. The limits in green shade are from measurements reported in [63], [21] and [62] (from left to right, respectively), which we use for comparisons in the text.

- Frequency coverage: 0.1 THz – 0.7 THz, with $T_{\text{rec}} \approx T_{\text{DSB}} = 2h\nu/k_B$ (SIS junction). Here, the configuration is essentially the same as above, except that the mixer is a SIS junction cooled at 4 K. The resulting sensitivity is labeled “SIS”.
- Frequency coverage: 10 GHz – 20 GHz. For this limit, we simply consider a commercial antenna with a noise temperature of 300 K. Details of the detection are assumed irrelevant. With an integration time of 30 h at a bandwidth 1 MHz, we immediately obtain the limit labeled “GHz antenna”. This result is intended to be a rough estimate of the sensitivity of FUNK++, in comparison with former measurements reported in [21]. However, the authors did not report details of their experiment that would allow us to make a sensible comparison.

Finally, let us remark that rather than describing realistic setups, these estimates purposely serve as a proof of concept, assuming the most optimized way of the detector arrangement.

4

Background photons

Contents

4.1 Internal background	63
4.1.1 Thermionic emission	64
4.1.2 Radioactive trace	65
4.1.3 Afterpulses	66
4.2 Thermal radiation	66
4.3 Cherenkov radiation	68
4.3.1 Atmospheric muons at sea level	68
4.3.2 Muons in laboratory	70
4.3.3 Cherenkov rate	72

After this little detour into `FUNK++`, we shall now return to the current status of the `FUNK` experiment. Our experiment is setup to count single photons resulting from the interaction of the Hidden-Photon Dark Matter (HPDM) field with the metallic surface of a large spherical mirror. These photons come together at the center of curvature of the mirror, where we installed a low-noise Photomultiplier Tube (PMT), sensitive to the visible and far-Ultraviolet (UV) spectra. HP-induced emission in this range corresponds to HP with eV masses. Our goal is to measure or constrain this emission rate over a certain level of background. In this chapter, we are interested in quantifying such a background and identifying the possible sources. These include photons or electrons which could either originate from the internal parts of the PMT — therefore termed internal background — or from external sources. Additionally, the background can be correlated or uncorrelated.

4.1 Internal background

Let us begin with a description of the noise and dark current of the PMT. This depends, to some degree of complexity, upon several parameters which

vary with different models of PMTs (photocathode type, glass, geometry, . . .), their operating mode (high-voltage, gain, . . .), and some environmental factors (temperature, humidity, exposure, . . .). As such, the sources are multiple: electronic noise, thermionic emission, field emission, radioactive trace localized in the envelope glass, Moreover, the typical dark rates may even differ by orders of magnitude for the same variant of the detector. For example, the employed PMT was selected amongst 3 acquired candidates, which exhibited a typical rate of 5 Hz, 15 Hz and 100 Hz during trials. Naturally, the device with the lowest background is preferable. A dedicated measurement of internal background of the selected PMT is described in Section 5.1. In the following, we describe the relevant known sources. Later, we will identify another non-trivial component of the background which appears to be characteristic of these low-noise PMTs.

At room temperature and considering the supplied high-voltage (~ 1 kV), the contribution due to thermionic emission from the photocathode and dynodes, is expected to dominate [103]. Typically, there is also a continuous contribution from leakage currents, due to the surface conductivity of different parts of the PMT. Nevertheless, this effect, alongside with other irreducible (low) noise of the device, are less relevant, as we are targeting the pulse components of the dark counts with a relatively high trigger threshold. Aside from that, the constant electric field applied between the dynodes may liberate electrons from the electrode surfaces, which can then go through the multiplier chain or excite other surfaces and induce scintillation light. This effect is called field or cold emission. In general, it is the predominant effect at higher voltage supply (≥ 2.5 kV).

4.1.1 Thermionic emission

Thermionic emission is due to the random emission of electrons from the photocathode surface, at room temperature, resulting into dark pulses of the single-electron type. Electrons originating from the multiplier chain are less amplified and usually amount less, to the extent that their contribution is often neglected. The expected current density from this effect is described by the Richardson's law. This represents typically between 10 to 1000 electrons/s/cm² for PMTs with good sensitivity in the visible range. For our consideration, the thermionic rate ϕ_{th} is given by

$$\phi_{\text{th}} = AT^2 e^{-W_{\text{th}}/k_{\text{B}}T}, \quad (4.1)$$

^a This is different from the photoemission threshold. where the W_{th} is the effective thermionic work function^a of the photocathode. W_{th} highly depends on the material-specific property. A is a dimensionful constant depending on the photocathode material, its area and other geometrical factor such as the collection efficiency of the PMT.

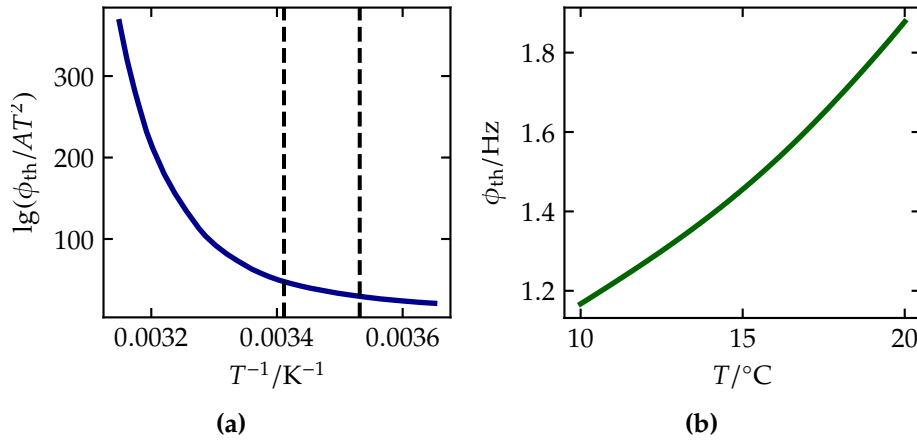


Figure 4.1: (a) Measurement of thermionic emission from a Bialkali photocathode, as reported in [104]. The dashed lines corresponds to temperatures of 10 °C and 20 °C. (b) Estimated temperature dependence of the thermionic rate for the FUNK PMT. The average gradient is evaluated to $0.07 \text{ Hz } ^\circ\text{C}^{-1}$.

The photocathode of the FUNK PMT is made of Bialkali material, whose thermal response is well-studied in the literature (see e.g. [104]). We use an existing measurement, shown in Fig. 4.1(a), to obtain a first estimate on the temperature coefficient of our PMT. This is achieved by rescaling this reported measurement — and thus accounting for the differing factor from the photocathode area and collection efficiency — with the assumption that our measured internal background (see Fig. 5.1) is mostly driven by thermionic emission. Using this procedure, we obtain a linear dependence of the rate on the temperature, with an average gradient of $0.07 \text{ Hz } ^\circ\text{C}^{-1}$, within the range of temperatures encountered during the measurement campaign (10 °C to 20 °C). This is within the typical values of the temperature coefficients of PMTs [105]. In general, a reduction of thermionic noise can be significantly achieved by cooling the PMT. However, we already stated the reasons for not activating the cooling module in Section 3.2.2.

4.1.2 Radioactive trace

Aside from thermionic emission, radioactive impurities (e.g. ^{40}K) localized in the glass envelope of the PMT also contribute to the pulse components of the dark current. The size of this effect depends on the abundance of radioisotopes in the glass, which we did not take into account. Nevertheless, it is instructive to give a qualitative description. The contribution to the dark current may appear in multiple forms [106].

For the ^{40}K isotopes, roughly 90% of the decay mode is via β -decay. The emitted electrons have an average kinetic energy of 0.6 MeV with an

end-point of 1.3 MeV, sufficient enough to cause Cherenkov radiation in the glass. Furthermore, these electrons may deposit most of their energy in the glass, resulting into scintillation light. Interestingly, it is suspected in [107] that the latter phenomenon might be responsible for a substantial correlated Non-Poissonian noise, identified in their measurements. We will find that such a component is also present in our measurement. Alternatively, the electrons from the β -decay may directly reach the dynodes and produce pulse signals. In about 10% of the case, the decay channel goes through an electron capture, which then radiates gamma-ray photons of 1.5 MeV, contributing to the noise on account of pair production in the glass.

4.1.3 Afterpulses

Afterpulses are background correlated to a *true* photoelectron released earlier, and producing another pulse delayed from a few nanoseconds to a few microseconds. There are basically two phenomena in play. First, photons possibly emitted at the stage of electron multiplications, may reach back the photocathode and liberate another photoelectron which will produce a new pulse, typically delayed by 20 ns to 100 ns with respect to the true pulse, depending on the transit times. Alternatively, back-scattered electrons at the first dynode stages and re-accelerated through the multiplier chain can lead to another pulse delayed within a similar time window. Second, the accelerated photoelectron can ionize the residual gas inside the tube. This results into positive ions which are accelerated towards the photocathode, provoking the release of secondary electrons which give rise to pulses delayed from a few 100 ns to a few μ s.

4.2 Thermal radiation

Above 0 K, any object continuously radiates electromagnetic energy due to the random thermal motion of particles. Therefore, such a contribution would rather appear as a constant component of our background rate. This is in contrast to, for instance, the Cherenkov background discussed in the next section which likely induces more variability in the data. Besides some geometrical factors, the amount of thermal radiation mainly depends on the body temperature and its spectral absorptivity. In the ideal case of a black-body^b at an absolute temperature T , the radiated power per wavelength

^b A black-body is simply a perfect absorber and perfect emitter, at all wavelengths.

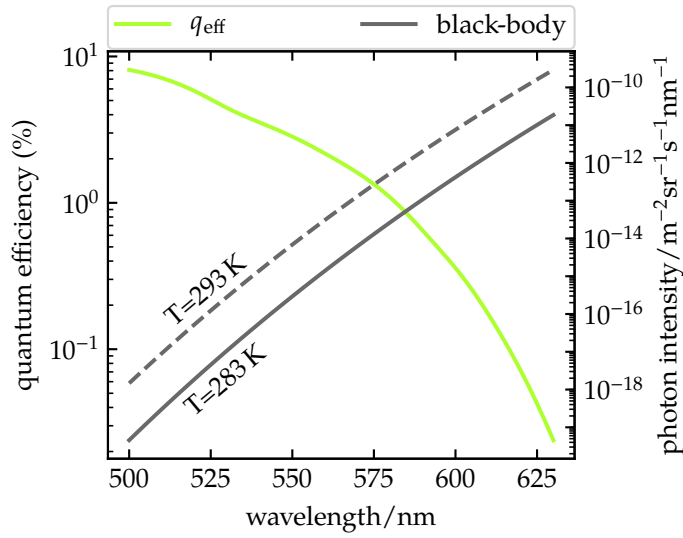


Figure 4.2: Quantum efficiency of the PMT superimposed with the photon intensity per unit wavelength from a black-body at two different temperatures.

interval $d\lambda$ and emitted per unit surface dA , within an unit solid angle $d\Omega$ is specified by the Planck's law

$$\begin{aligned} \mathcal{B}(\lambda, T) &= \frac{dE_\gamma}{dA d\Omega dt d\lambda} = \frac{2hc^2/\lambda^5}{\exp(hc/\lambda kT) - 1} \\ &= \frac{1.19 \times 10^{-16} \text{ W m}^{-2} \text{ sr}^{-1} \text{ m}^{-1} (1 \text{ m}/\lambda)^5}{\exp(1.44 \times 10^{-2} (1 \text{ m}/\lambda)(1 \text{ K}/T)) - 1}. \end{aligned} \quad (4.2)$$

The spectral radiance $\mathcal{B}(\lambda, T)$ rapidly increases at shorter wavelengths till it reaches a peak at $\lambda = \lambda_{\text{peak}}$, then it slowly decreases at larger wavelengths. The emission peak is prescribed by the Wien's displacement law

$$\lambda_{\text{peak}} = \frac{b}{T} = 2.898 \times 10^{-3} \text{ m} \left(\frac{1 \text{ K}}{T} \right). \quad (4.3)$$

At room temperature ($T = 298 \text{ K}$), this corresponds to $\lambda_{\text{peak}} = 10 \mu\text{m}$ which falls into Infrared (IR) and is beyond the sensitive region of the FUNK PMT. Nevertheless, the quantum efficiency q_{eff} of the PMT certainly overlap with the Planck spectrum in the near-IR. Hence it is instructive to quantify this overlap. Let us suppose that the PMT simply sees a black-body which, in our case, represents the whole half-space towards the mirror (hereafter denoted by \subset). The rate of photons ϕ_{bb} radiated by such an isotropic thermal source

and detectable by our PMT can be computed by integrating Eq. (4.2) as follows,

$$\phi_{\text{bb}} = \frac{1}{\langle E_\gamma \rangle} \int_C dA d\Omega \int_{\lambda_1}^{\lambda_2} d\lambda q_{\text{eff}}(\lambda) \mathcal{B}(\lambda, T), \quad (4.4)$$

where the average photon energy is $\langle E_\gamma \rangle = 1/(\lambda_2 - \lambda_1) \int_{\lambda_1}^{\lambda_2} d\lambda h c / \lambda$ and the effective Field of View (FoV) of the PMT reads as $\int_C dA d\Omega = 2\pi A$.

In Fig. 4.2, we plot the photon intensity per unit wavelength $\mathcal{B}(\lambda, T)/\langle E_\gamma \rangle$, together with the quantum efficiency of the PMT. Within the spectral coverage of the latter, 150 nm to 630 nm, we find $\langle E_\gamma \rangle = 3.7$ eV which yields

$$\phi_{\text{bb}}/A = 4.6 \times 10^{-9} \text{ s}^{-1} \text{ m}^{-2}. \quad (4.5)$$

Clearly, such a contribution is irrelevant to our overall background and by definition, the ambient thermal radiation does not exceed that estimated from a black-body.

4.3 Cherenkov radiation

When a charged particle traverses a medium with velocity βc greater than the local speed of light c/n , it emits an electromagnetic radiation whose spectrum is function of the index of refraction n of the medium and the energy E of the charged particle. This is known as the Cherenkov effect. In underground locations, the dominant sources of Cherenkov photons are penetrating Cosmic Ray (CR) muons. CRs are charged particles of galactic or extragalactic origins. When these particles enter the Earth's atmosphere, they interact with the air molecules and produce a cascade of secondary particles, amongst which many are muons. These muons often have enough energy to reach the Earth's surface and even penetrate deeper. Depending on the intensity of these muons at a certain depth, the amount of Cherenkov radiation could contribute significantly to our background. Thus the first step is to estimate the flux of CR muons. And the second step is to evaluate the Cherenkov rate associated with these muons.

4.3.1 Atmospheric muons at sea level

Atmospheric muons come from the decay of the mesonic component of CR air-showers at higher altitudes. The relevant decay channels are

$$\begin{cases} \pi^\pm \longrightarrow \mu^\pm + \nu_\mu/\bar{\nu}_\mu \quad (\sim 0.999) \\ K^\pm \longrightarrow \mu^\pm + \nu_\mu/\bar{\nu}_\mu \quad (\sim 0.635), \end{cases} \quad (4.6)$$

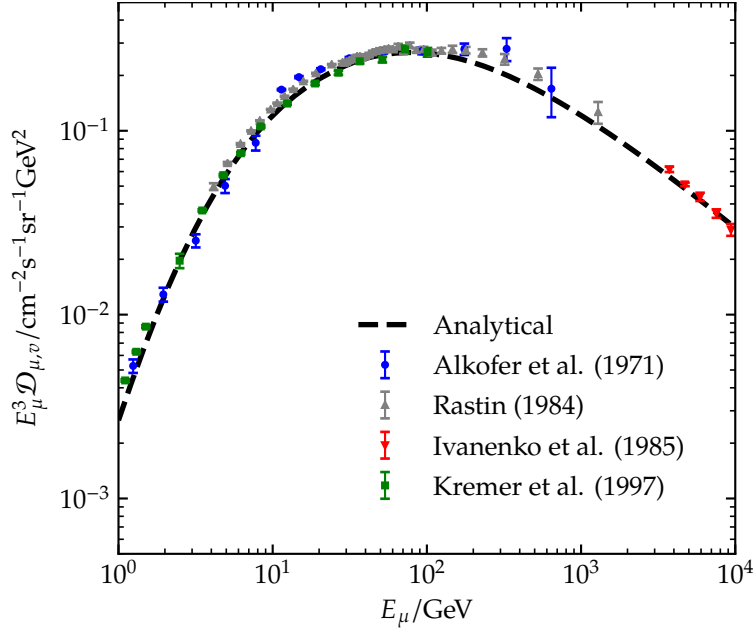


Figure 4.3: Differential intensity $\mathcal{D}_{\mu,v}$ of vertical muons, as function of the muon energy E_μ at sea level. The computation follows the algorithm of [108]. The various error-bars correspond to experimental measurements reported in [109–112]. The spectrum has been multiplied by E_μ^3 to enhance the details.

where their respective branching-ratios are indicated in parenthesis. Because of their relatively long mean lifetime ($\tau_\mu = 2.20 \mu\text{s}$) and their small interaction cross-sections, relativistic muons can traverse the entire thickness of the atmosphere. Hence, they remain largely abundant at ground, with a mean energy of $\sim 4 \text{ GeV}$.

It is convenient to follow the development of the fluxes of secondary particles in the cascade shower in terms of the *slant depth* X , defined as

$$X = \frac{X_v}{\cos \vartheta} = \int_0^\infty dh \rho_{\text{atm}}(h), \quad (4.7)$$

where X_v is the *vertical depth*^c and ϑ the particle zenith-angle. ρ_{atm} denotes the altitude-dependent density of the Earth's atmosphere and the integration is carried-out along the particle height h , from the top of the atmosphere. ^c At sea level, $X_v^{\text{sea}} = 1030 \text{ g cm}^{-2}$.

The linear evolution of the *differential intensity* \mathcal{D}_μ of the muonic component of the air-shower obeys the cascade equation [108, 113]

$$\frac{\partial \mathcal{D}_\mu(E, X)}{\partial X} = -\frac{\mathcal{D}_\mu(E, X)}{\lambda_\mu^{\text{dec}}} - \frac{\partial}{\partial X} (\xi(E) \mathcal{D}_\mu(E, X)) + \mathcal{S}(K, \pi \rightarrow \mu). \quad (4.8)$$

\mathcal{D}_μ is defined as the number of muons N_μ per unit area dA , within an unit solid angle $d\Omega$, per unit time dt , per energy interval dE and at a slant

depth X , such that $\mathcal{D}_\mu(E, X) = dN_\mu/dA d\Omega dt dE$. The first term in the right-hand side of Eq. (4.8) accounts for the muon decay-in-flight with decay length λ_μ^{dec} . The next term describes the muon energy loss^d as a continuous process, where $\xi(E) = dE/dx$. The last term represents the muon source from meson weak-decays and is summed up over all production channels. Under a few assumptions, it is possible to solve the integro-differential Eq. (4.8) analytically^e.

^d Muons typically lose ~ 2 GeV before reaching ground.

^e See Chapters 5 and 6 of [98] for a review.

We followed a semi-numerical treatment and implemented the algorithm given in [108]. The calculations are done in two steps. First, we compute the fluxes of charged pions and kaons from a primary nucleon flux with a power-law spectrum. The meson fluxes contribute into the source term of Eq. (4.8). Second, we compute the flux of muons from the production channels given in Eqs. (4.6), while taking into account the decay and energy loss of muons. The spectrum obtained with these limited considerations is often termed conventional spectrum. It provides a good description of atmospheric muons with energies below ~ 20 TeV [113], that are relevant for our experiment. The result for the differential intensity of vertical muons ($\vartheta = 0$) is shown in Fig. 4.3 together with a compilation of datasets from various experiments. We obtain an approximation of the muon abundance at sea level, such that

$$\begin{aligned} \mathcal{D}_{\mu,v} &= \mathcal{D}_\mu(E_\mu, \vartheta=0) \\ &= 2.863 \times 10^{-3} \text{ cm}^{-2} \text{ sr}^{-1} \text{ s}^{-1} \text{ GeV}^{-1} \\ &\quad \times E_\mu^{-0.589 - 0.384 \ln(E_\mu/\text{GeV}) + 0.016 [\ln(E_\mu/\text{GeV})]^2}, \end{aligned} \quad (4.9)$$

which is compatible with the best-fits commonly found in the literature [114].

4.3.2 Muons in laboratory

Muon energy loss

Muons interact with matter via electromagnetic and weak interactions. The conventional description of energy loss by charged particles assumes a continuous deterministic process. The loss rate within an amount of matter dX can be expressed as

$$-\frac{dE_\mu}{dX} = a(E_\mu) + b(E_\mu)E_\mu, \quad (4.10)$$

where $a(E_\mu)$ corresponds to energy loss by ionization and $b(E_\mu)$ accounts for the combined radiative losses due to bremsstrahlung, pair production, and photonuclear interactions. Both functions a and b vary slowly with energy but also depend on the medium^f. Computed values for standard

^f Tabulated data are available for a wide range of energies and materials, see e.g. [115].

E_μ/GeV	$a/(\text{MeV g}^{-1} \text{cm}^2)$	$b/(10^{-6} \text{g}^{-1} \text{cm}^2) = b_{\text{brems}} + b_{\text{pair}} + b_{\text{nucl}}$
10	2.17	1.90
100	2.44	3.04
1000	2.68	3.92

Table 4.1: Parameters of energy loss for muons in standard rock (adapted from Table 29.2 in [8]).

rock are given in Table 4.1. For numerical estimates and to the extent that energy dependence can be neglected, we use $a \approx 2 \text{ MeV g}^{-1} \text{ cm}^2$ and $b \approx 2.5 \times 10^{-6} \text{ g}^{-1} \text{ cm}^2$, referring to [98]. A useful quantity is the critical energy ϵ which is defined as the energy at which contributions from ionization and radiative losses become comparable, i.e. $\epsilon = a/b$. The solution of Eq. (4.10) can then be written as

$$E_\mu(X) = (E_{\mu,0} + \epsilon)e^{-b(X-X_0)} + \epsilon \quad (4.11)$$

$$\simeq E_{\mu,0} - a(X - X_0), \quad (4.12)$$

with the initial condition $E_{\mu,0} = E_\mu(X=X_0)$. The approximation (4.12) is valid when $b(X - X_0)$ remains small, i.e. at shallow depths.

The FUNK experiment is situated under a thick concrete shielding. In concrete, the critical energy is around $\epsilon_{\text{con}} \approx 500 \text{ GeV}$. Since most muons arriving at ground have energies $E_\mu < \epsilon_{\text{con}}$, we can neglect radiative effects so that underground muons lose their energy at a fairly constant rate. The energy dependence of the muon spectrum at a depth X is then trivial,

$$\frac{d\mathcal{D}_\mu}{dE_\mu^{\text{lab}}} = \frac{d\mathcal{D}_\mu}{dE_\mu^{\text{sea}}} \frac{dE_\mu^{\text{sea}}}{dE_\mu^{\text{lab}}} \quad (4.13)$$

$$\simeq \left. \frac{d\mathcal{D}_\mu}{dE_\mu^{\text{sea}}} \right|_{E_\mu^{\text{sea}} = E_\mu^{\text{lab}} + a(X^{\text{lab}} - X^{\text{sea}})}, \quad (4.14)$$

where E_μ^{sea} and E_μ^{lab} are the muon energies measured at the sea level and in the laboratory, respectively. In the last step, we used Eq. (4.12). In case of FUNK[§], the vertical depth is $X_v^{\text{lab}} - X_v^{\text{sea}} = \rho_{\text{con}} x_{\text{con}} \approx 480 \text{ g cm}^{-2}$ which corresponds to an energy loss of $E_\mu^{\text{sea}} - E_\mu^{\text{lab}} \approx 960 \text{ MeV}$.

[§] We suppose that Karlsruhe is roughly at sea level. The density of concrete is $\rho_{\text{con}} \approx 2.4 \text{ g cm}^{-3}$ and the shielding has $x_{\text{con}} \approx 2 \text{ m}$.

Integral intensity and flux

For definiteness, we only consider muons with energy greater than $E_0 = 1 \text{ GeV}$ at sea level, as being detectable by the muon monitoring system of FUNK described in Section 3.2.6. It is easy to obtain the *integral intensity* $\mathcal{I}_{\mu,v}$ of

vertical muons within the experimental area from Eqs. (4.9) and (4.14), such that

$$\mathcal{I}_{\mu,v} = \int_{E_{\mu} \geq E_0} dE_{\mu} \mathcal{D}_{\mu,v} = 6.76 \times 10^{-3} \text{ cm}^{-2} \text{ sr}^{-1} \text{ s}^{-1}. \quad (4.15)$$

This result is compatible with the standard reference values that experimentalists are familiar with [114]. In addition, our calculation based on an approximate CR propagation is in good agreement within 24 % of the value of $\mathcal{I}_{\mu,v}$ given in Eq. (3.12) and inferred from the muon data.

In the GeV ranges and for $\vartheta \lesssim 70^\circ$, the angular dependence of the integral intensity can be approximated as [98]

$$\mathcal{I}_{\mu}(\vartheta, \phi) = \mathcal{I}_{\mu,v} \cos^2 \vartheta. \quad (4.16)$$

It is of interest to estimate the number of muons crossing the operating area of FUNK. For the geometry of the experimental area (length = 4.98 m, width = 4.35 m, height = 4.30 m, $V_{\text{area}} = 93.15 \text{ m}^3$), the relevant formulas are derived in Appendix A. From Eq. (A.1), the expected flux of downward muons in the laboratory, traversing a horizontal surface from zenith-angles $0 \leq \vartheta \leq \pi/2$ is $J_{\text{H}} \approx 106.2 \text{ m}^{-2} \text{ s}^{-1}$, which is compatible with the overall measured fluxes plotted in Fig. 3.21. Then using Eq. (A.4), we obtain a rate density of

$$\phi_{\mu}/V_{\text{area}} = 47.6 \text{ s}^{-1} \text{ m}^{-3}. \quad (4.17)$$

4.3.3 Cherenkov rate

The number of Cherenkov photons N_{ch} emitted within a spectral range $\Delta\lambda$, per unit path-length dl of a single muon traveling through a medium having an index of refraction $n(\lambda)$ and at velocity $\beta > 1/n$ is given by [8]

$$\frac{dN_{\text{ch}}}{dl} = \int_{\Delta\lambda} d\lambda \frac{2\pi\alpha}{\lambda^2} \left(1 - \frac{1}{\beta^2 n^2(\lambda)} \right), \quad (4.18)$$

where α is the fine structure constant. The particle velocity $v = \beta c$ must exceed the phase-velocity of light $v_p = \omega/k = c/n$ within the medium, which hence constrains^h the spectral range $\Delta\lambda$. On the other hand, the driving term λ^{-2} in the integrand of Eq. (4.18) implies that the emission spectrum is shifted towards shorter wavelengthsⁱ. This specific electromagnetic radiation is emitted within a cone, as illustrated in Fig. 4.4. In the ideal case of non-dispersive medium (i.e $dn/dk = 0$), the geometrical construction implies $\cos \theta_{\text{ch}} = 1/\beta n$. The dispersion effect on the Cherenkov angle is however small for most practical cases.

The velocity-threshold is $\beta_{\text{thres}} = 1/n(\lambda)$ or equivalently, in energy-threshold $E_{\text{thres}} = m_{\mu} \gamma_{\text{thres}}$ for a muon. In order to radiate Cherenkov

^h There is a frequency cut-off corresponding to $n(\lambda) < 1$.

ⁱ Hence glowing blue when it is visible.

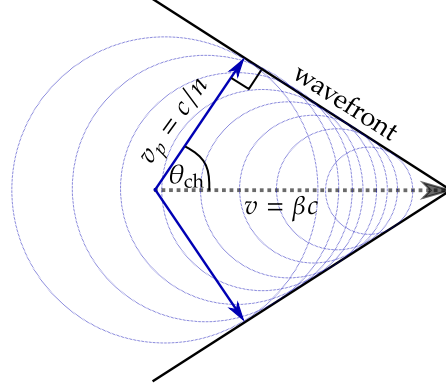


Figure 4.4: Cherenkov emission of a fast-moving particle with velocity v greater than the local phase-velocity v_p of light. In case of a non-dispersive medium, the Cherenkov angle satisfies $\theta_{\text{ch}} = \arccos(v_p/v)$.

photons with wavelengths $\lambda_1 \leq \lambda \leq \lambda_2$, we demand $\beta_{\text{thres}} = \max\{1/n(\lambda)\}$. Therefore the minimum muon energy is given by

$$E_{\text{thres}} = m_\mu \frac{1}{\sqrt{1 - \beta_{\text{thres}}^2}} = m_\mu \frac{\delta_{\text{thres}} + 1}{\sqrt{\delta_{\text{thres}}^2 + 2\delta_{\text{thres}}}}, \quad (4.19)$$

where

$$\delta_{\text{thres}} = \begin{cases} n(\lambda_1) - 1 & \text{if } dn/d\lambda > 0 \\ n(\lambda_2) - 1 & \text{if } dn/d\lambda < 0 \end{cases}. \quad (4.20)$$

To obtain the average Cherenkov rate ϕ_{ch} , we need to integrate over the differential intensity \mathcal{D}_μ of muons such that

$$\phi_{\text{ch}} = \langle L_\mu \rangle \int dA d\Omega \cos \vartheta \int_{E_{\text{thres}} + E_0}^{\infty} dE_\mu \mathcal{D}_\mu(E_\mu) \int_{\lambda_1}^{\lambda_2} d\lambda \frac{2\pi\alpha}{\lambda^2} \sin^2 \theta_{\text{ch}}(E_\mu, \lambda). \quad (4.21)$$

Here $\langle L_\mu \rangle$ denotes the average path-length of muons within the medium of consideration. The spectrum for vertical muons at sea level is estimated from Eq. (4.9), while the angular dependence of the integral intensity follows Eq. (4.16). The additional translation by $E_0 = 1$ GeV is to account for the energy that muons lose before they reach the FUNK experimental hall, as discussed in Section 4.3.2. Finally, we have written $\sin^2 \theta_{\text{ch}} = 1 - 1/\beta^2 n^2$. In principle, we should also include the quantum efficiency $q_{\text{eff}}(\lambda)$ of the photodetector. Nevertheless, it is sufficient to understand this addition from

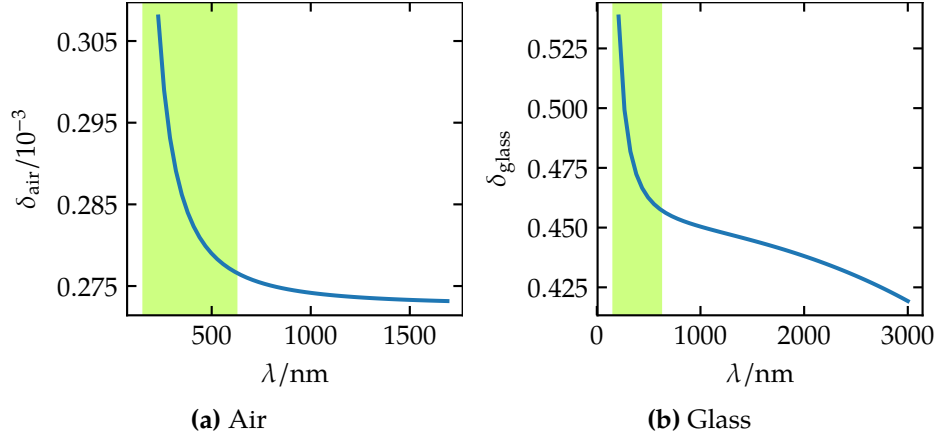


Figure 4.5: Indices of refraction for standard dry air ($P = 1013.25$ hPa, $T = 15$ °C) and glass (fused silica) [68]. We plot $\delta(\lambda) = n(\lambda) - 1$ to follow literature convention. The green-shaded region marks the spectral coverage of our PMT.

a quantitative point of view. Of more importance is the overall efficiency of the detector to actually capture the photons, which rather depends on some geometrical factors. We can write Eq. (4.21) in a more compact form

$$\phi_{\text{ch}} = 2\pi\alpha \left(\frac{1}{\lambda_1} - \frac{1}{\lambda_2} \right) \langle \sin^2 \theta_{\text{ch}} \rangle_{\lambda, E_\mu} \langle L_\mu \rangle \phi_\mu, \quad (4.22)$$

where the expected rate of muons which could produce Cherenkov radiation is

$$\phi_\mu = \int dA d\Omega \cos \vartheta \int_{E_{\text{thres}} + E_0}^{\infty} dE_\mu \mathcal{D}_{\mu, \nu} \cos^2 \vartheta, \quad (4.23)$$

and the averaged Cherenkov angle is obtained from

$$\langle \sin^2 \theta_{\text{ch}} \rangle_{\lambda, E_\mu} = \frac{\int_{E_{\text{thres}} + E_0}^{\infty} dE_\mu \mathcal{D}_{\mu, \nu} \langle \sin \theta_{\text{ch}} \rangle_\lambda}{\int_{E_{\text{thres}} + E_0}^{\infty} dE_\mu \mathcal{D}_{\mu, \nu}}, \quad (4.24)$$

$$\langle \sin^2 \theta_{\text{ch}} \rangle_\lambda = \frac{\int_{\lambda_1}^{\lambda_2} d\lambda \lambda^{-2} \sin^2 \theta_{\text{ch}}(E_\mu, \lambda)}{\int_{\lambda_1}^{\lambda_2} d\lambda \lambda^{-2}}. \quad (4.25)$$

It is worth to remark that while the muon rate varies with the geometry of the medium, the Cherenkov angle is rather determined by its nature. Given the geometry and nature of the propagating medium, it is easy to calculate each quantity in Eq. (4.22). In case of a rectangular volume, we use formulas A.8 and A.4 to estimate $\langle L_\mu \rangle$ and ϕ_μ , respectively. As a result,

Medium	E_{thres} [GeV]	$\langle\theta_{\text{ch}}\rangle_{\lambda, E_{\mu}}$ [°]	$\mathcal{I}_{\mu, v}(E_{\mu} \geq E_{\text{thres}} + E_0)$ [cm ⁻² sr ⁻¹ s ⁻¹]	ϕ_{ch}/V [s ⁻¹ m ⁻³]
Dry Air	4.521	1.15	1.81×10^{-3}	3.57×10^3
Fused Silica	0.145	49.1	6.36×10^{-3}	1.77×10^7

Table 4.2: Cherenkov background calculated from Eq. (4.26). The volumes of the restricted area of FUNK and the PMT isolation window are estimated to $V_{\text{air}} = 4.98 \times 4.35 \times 4.30 \text{ m}^3$ and $V_{\text{glass}} = 0.1 \times 2.5 \times 2.5 \text{ cm}^3$; which translated into absolute photon-rates yield 332.1 kHz and 11.1 Hz, or equivalently $93.9(\langle L_{\mu} \rangle / \text{m})(\phi_{\mu} / \text{s}^{-1})$ and $132.9(\langle L_{\mu} \rangle / \text{mm})(\phi_{\mu} / \text{s}^{-1})$, in both respective media. As comparison, see [116] for an estimation of the Cherenkov background in natural caves.

the total path-length of muons $\langle L_{\mu} \rangle \phi_{\mu}$ only depends on the volume V the medium and we have

$$\phi_{\text{ch}} / \text{s}^{-1} = 4.88 \times 10^6 \langle \sin^2 \theta_{\text{ch}} \rangle_{\lambda, E_{\mu}} \left(\frac{\mathcal{I}_{\mu, v}(E_{\mu} \geq E_{\text{thres}} + E_0)}{10^{-3} \text{ cm}^{-2} \text{ sr}^{-1} \text{ s}^{-1}} \right) \left(\frac{V}{\text{m}^3} \right), \quad (4.26)$$

for photon wavelengths $150 \leq \lambda / \text{nm} \leq 630$. We consider two propagating media, namely standard air (surrounding of the FUNK setup) and fused-silica glass (isolation window of the PMT). Their respective indices of refraction are plotted in Fig. 4.5. The final estimates for the Cherenkov background are summarized in Table 4.2.

Lastly, the index of refraction of the air also slightly varies with the ambient pressure and temperature. This variation can be expressed as follows [117]

$$\delta = \delta_{\text{std}} \left(\frac{1.055 P / P_0}{1 + 0.055 T / T_0} \right), \quad (4.27)$$

where $\delta_{\text{std}} = n_{\text{std}} - 1 = 2.79 \times 10^{-4}$ (at $\lambda = 500 \text{ nm}$) is measured for standard air, that is defined as dry with 450 ppm CO₂ at $P_0 = 1013.25 \text{ hPa}$ and $T_0 = 15 \text{ °C}$. For ambient temperature, this induces a linear dependence of the Cherenkov rate on the air pressure with a gradient of

$$\Delta \phi_{\text{ch}} / \Delta P = 0.508 \text{ kHz hPa}^{-1}, \quad (4.28)$$

within the pressure range $900 \leq P / \text{hPa} \leq 1100$. This represents a $\sim 0.2\%$ effect compared to our overall estimation in Table 4.2 (see caption). The impact on detectable photons is thus negligible.

5

Data analysis

Contents

5.1	Background measurement	78
5.1.1	Dark current	79
5.1.2	Volume effect	81
5.2	Standard measurement	83
5.2.1	Summary of data run	83
5.2.2	Background sources	84
5.2.3	Event selection	87
5.2.4	Correlation study	91
5.3	Deviation from homogeneous Poissonian process	93
5.3.1	Overdispersion	94
5.3.2	Correlated events	96
5.4	Memory effect	101
5.4.1	Characterization of the FUNK PMT	101
5.4.2	Model	103
5.4.3	Fitting	108
5.4.4	Event reconstruction	109
5.4.5	Temperature correlation	111
5.5	Fourier analysis	113
5.5.1	Spectral decomposition	113
5.5.2	Low-frequency detrending	115
5.6	Systematical uncertainties	116
5.6.1	DAQ timing	116
5.6.2	Environmental conditions	116
5.6.3	Mirror reflections	118
5.7	Improved exclusion limit	120

In this chapter, we present a detailed analysis of measurements performed in the middle Ultraviolet (UV) and near spectra with a low-noise Photomultiplier Tube (PMT) sensitive to photon wavelengths from 150 nm to 630 nm. This corresponds to a coverage of Hidden Photon (HP) masses between 2 eV and 8 eV. After an earlier phase conducted with a CCD camera [69], FUNK started taking data again in the beginning of 2017 with the upgraded setup described in Section 3.2. Our basic operation aims at measuring, in extreme darkness, the rate of single-photon events with various configurations of the PMT camera, and then identifying possible HP signal. The data-taking period comprises various testing and calibration runs, followed by background monitoring and standard measurements. The Single Photoelectron (SPE) calibration procedures are already explained in Section 3.2.4. These measurements also provide us with checks and proof of the proper working of the ensemble of the Data Acquisition (DAQ) chain. We shall readily apply the results obtained to our data analysis later. For all measurements presented here, the data taking is split in regular intervals of $\Delta t = 60$ s but performed with modified configurations depending on whether we want to measure background only or also include possible signal. A more comprehensive description of the DAQ hardware and software is given in Section 3.2.3.

Preliminary results were previously published in [60, 61] for which we reported a competitive limit on the HP mixing strength. In light of the discovery a non-negligible memory effect of the FUNK PMT, we reanalyze new data and develop a new reconstruction algorithm of events which will improve this limit by at least a factor of 3. This chapter is structured as follows. Firstly, we present results from our recent measurements. Secondly, we discuss all features of the data which include an interesting deviation from ordinary Poisson statistics. Systematical effects are also evaluated. Lastly, in absence of a significant HP signal, we give an up-to-date upper-bound on the strength of its mixing parameter.

5.1 Background measurement

Our first step is to try to understand the background of the experiment. Besides a good performance from the detector, FUNK operates in extremely low-light conditions (with few photons/s detected) which was achieved, in particular, by confining the main experimental area within a light-proof and conditioned area, as reported in Section 3.1. The natures, origins and relevances of diverse sources of background are discussed in Chapter 4. In the following, we shall make a distinction between internal and exter-

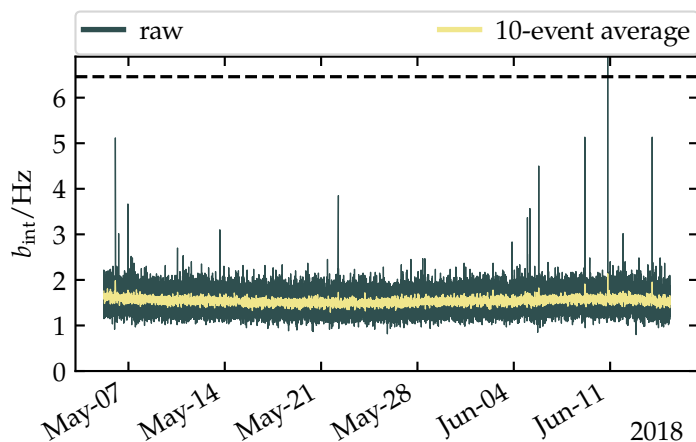


Figure 5.1: Trigger rate recorded with the sealed-FACT50 enclosure, showing the internal background b_{int} of the PMT. The labels *raw* and *10-event average* mean number of triggers in intervals of 60 s and 10 min, respectively. The dashed line indicates the total background $b_{\text{int}} + b_{\text{ext}}$, measured with the configuration *out/open* plotted in Fig. 5.5.

nal nuisances, in line with their origins, and we evaluate their respective contributions to the dark current of the PMT.

5.1.1 Dark current

To begin with, we measured the internal background b_{int} of the PMT. This was executed by attaching a thick metal lid onto the opening of the FACT50 housing (see Section 3.2.2) in such a way that the PMT is totally deprived from any direct light-sources during the entire monitoring. This sealed-FACT50 run is numbered v31 in our measurement campaign. The full run lasted approximately 43 days. Nonetheless, we allow the PMT to relax for roughly 2 days before taking into account the data, in order to avoid contributions due to excitation of the photocathode, inevitably introduced during manipulations. The recorded trigger rates are displayed in Fig. 5.1, where we can observe a very stable background rate with a mean trigger $\langle b_{\text{int}} \rangle = 1.55$ Hz and a standard deviation of 0.20 Hz. The isolated peaks, seen at certain times, are presumably the results of Cosmic Ray (CR) muons directly hitting the glass envelope of the PMT and thus releasing many Cherenkov photons.

Since we prescribe an absolute trigger-threshold of 8 Analog-to-Digital Converter (ADC) units below baseline — the latter being estimated from the truncated mean μ_{trunc} of each individual trace (see explanation in Section 3.2.3) — it is also interesting to check whether these two quantities are correlated in time. It is clear that a movement of the baseline, which could

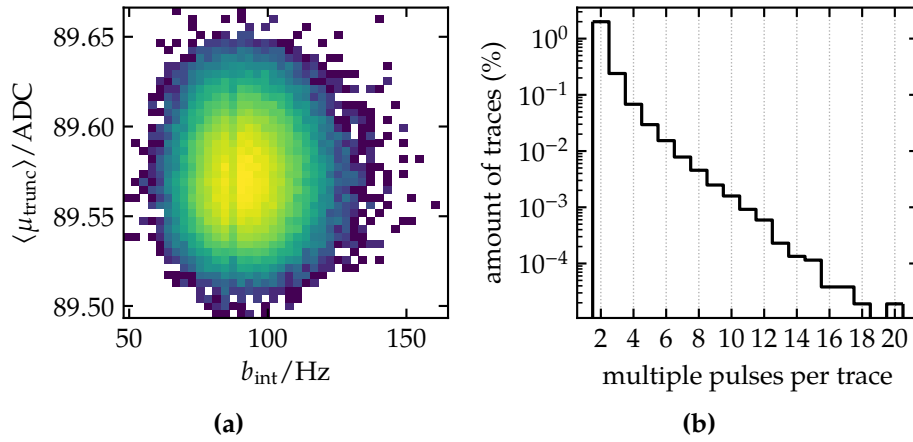


Figure 5.2: (a) 2D density scatter-plot of the average trace-baseline $\langle \mu_{\text{trunc}} \rangle$ and the PMT trigger rate during the sealed-FACT50 run, showing that the two variables are uncorrelated. (b) Fractional amount of traces containing multiple pulses, during the same run.

be easily associated to temperature fluctuations or electronic noise, would influence to some extent the number of triggers registered. The typical variation of the baseline is however estimated to be less than 0.3 % with respect to its nominal value. In addition, we found no significant correlation between the trigger rate and the average baseline per trace. Therefore no additional correction is needed. These statements are illustrated in Fig. 5.2(a), where we plotted the joint distribution of the background rate b_{int} measured with the sealed-FACT50 and the averaged truncated-means $\langle \mu_{\text{trunc}} \rangle$ of traces captured per 60 s interval.

In line with our discussion in Section 4.1, the dominant contribution to the measured background, in the present case, is due to thermionic emission from internal parts of the PMT, and giving rise to SPE like signals. Other causes include afterpulsing and particle-shower hits. By contrast, these effects would most likely leave multiple pulses in the same trace though. As a matter of fact, we are more interested in the number of pulses than the number of triggers or traces only. With the sealed-FACT50 housing, about 2 % of the total captured traces contained multiple pulses. The corresponding fraction of afterpulses is thus certainly small and compatible with the quoted rate of $\sim 1\%$ from the PMT datasheet [73]. This estimation can be seen in Fig. 5.2(b), where we show the distribution of number of multiple pulses per trace, normalized by the total number of traces. Note that for this plot, we use all pulses identified by the pulse-finder algorithm (see description in §. Software of Section 3.2.3) and without any additional quality cuts.

5.1.2 Volume effect

In Fig. 5.1 we already hinted that the contribution of external sources to the background is about 3 times larger, for our standard measurement. We shall further quantify these sources in Section 5.2.2. For the moment, it is instructive to investigate the dependence of the dark currents on the volume directly surrounding the PMT. For this purpose, we devised a series of measurements during which we restricted the detector arrangement around a customized black-box with a volume $\sim 0.2 \text{ m}^3$, which is ~ 500 times smaller than our normal setup. The black-box was installed in such a way that the volume in front of the PMT could be adjusted. A series of gradual improvement were also conducted in order to identify potential nuisances within this more contained environment. In addition, we employed an optical shutter consisting of a wrapped metallic plate operated with a Thorlabs MFF101 flipper [82]. Due to mounting constraints, this shutter did not have a full efficiency, especially because light could leak from sides of the camera window. Data are then taken in cycle of shutter *open/closed*. Each of these control measurements, numbered from v26 to v30 in Fig. 5.3(a), lasted approximately 2 days and the region directly seen by the PMT was gradually reduced from 1/2 to 1/5 of the volume of the black-box. As an immediate effect, we observed a significant reduction of the trigger rates, as compared with a standard measurement numbered v25 in the same figure.

We can do the following exercise to evaluate the amount of external background b_{ext} measured in these conditions and to be distinguished from the internal background b_{int} discussed above. Let us write the count rates registered with the shutter open and closed as

$$\begin{aligned} r_{\text{open}} &= b_{\text{int}} + b_{\text{ext}}, \\ r_{\text{closed}} &= b_{\text{int}} + \varepsilon b_{\text{ext}}, \end{aligned} \quad (5.1)$$

respectively. Here, ε is assumed to be constant and it represents the fractional amount of light which can leak through the shutter. Conversely, $1 - \varepsilon$ denotes the shutter opacity. Knowing b_{int} , it is trivial to solve Eq. (5.1) for the unknowns ε and b_{ext} .

To better understand the situation though, let us evaluate b_{ext} independently. We want to examine the variation of the rate difference $r_{\text{open}} - r_{\text{closed}}$ with respect to the total rate r_{open} . This can be seen from Fig. 5.3(b) where we read a linear dependence. Note that this is not a simple scaling factor, since by construction $r_{\text{open}} \geq b_{\text{int}}$. For now, combining this result with Eq. (5.1), we derive

$$1 - \varepsilon = \frac{1}{b_{\text{ext}}}(r_{\text{open}} - r_{\text{closed}}), \quad (5.2)$$

$$b_{\text{ext}} = m(r_{\text{open}} - r_{\text{closed}}) + n - b_{\text{int}}, \quad (5.3)$$

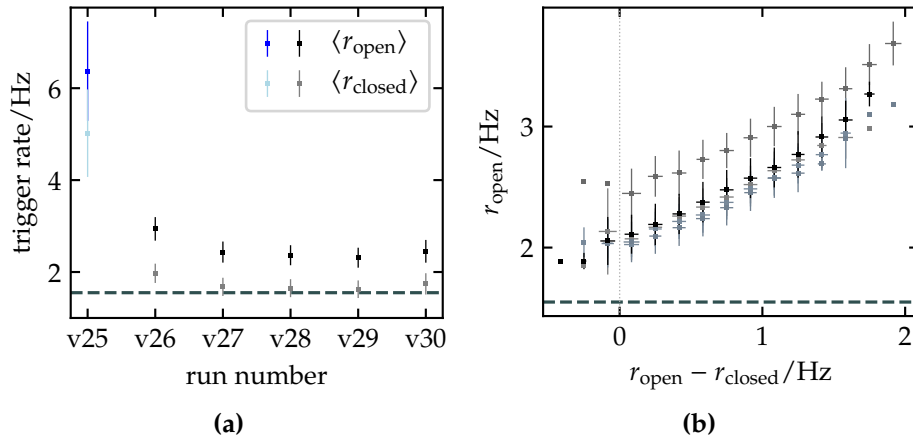


Figure 5.3: (a) Average trigger rate measured inside the black-box (from run v26 to v30) with the shutter open and closed, labeled $\langle r_{\text{open}} \rangle$ and $\langle r_{\text{closed}} \rangle$ respectively. Run v25 is a standard measurement, discussed later, but plotted for reference. (b) Binned scatter-plot of the total rates and the differences between the two modes for the various measurements inside the black-box. In both plots, error bars correspond to standard deviations of the distributions and the dashed line indicates the internal background $\langle b_{\text{int}} \rangle$ plotted in Fig. 5.1.

where m and n denote the slope and intercept of a linear least-squares fit of the unbinned data used in Fig. 5.3(b). Let us make two remarks. Firstly, Eq. (5.2) does not allow negative values of the rate difference. Therefore we momentarily discard these fluctuations in our calculation. Secondly, the model described by Eq. (5.1) predicts $m = 1/(1 - \epsilon)$ and $n = b_{\text{int}}$, i.e. $b_{\text{ext}} \propto r_{\text{open}} - r_{\text{closed}}$ as is clear from Eq. (5.2). Yet, we find that not only the intercept is slightly higher than the typically measured $b_{\text{int}} = 1.55$ Hz, but it also varies between the measurements, with $n \gtrsim 2$ Hz.

The values of $1 - \epsilon$ and b_{ext} are given in Table 5.1 for the measurements v26 to v30 inside the black-box. For these conditions, we conclude that the efficiency of the shutter is not constant but rather slowly increases as the amount of external radiation decreases. In fact, this result should not be very surprising. What is mostly puzzling is that, with a similar approach applied to our standard measurement, we find that the shutter opacity drastically drops to $1 - \epsilon \approx 30\%$ while the background ratio become $\langle b_{\text{ext}} \rangle / \langle b_{\text{int}} \rangle \approx 3.2$.

The reason behind these observations has been found to be an often neglected phenomenon in the PMT itself, which invalidates a simplified model like Eq. (5.1) and makes the notion of shutter opacity less apparent. We address this problem in Section 5.4. On the other hand, it also justifies the need of upgrading the shutter to the Uniblitz NS65B variant [81] which offers a full efficiency as tested by the manufacturer (see Section 3.2.2).

run number	v26	v27	v28	v29	v30
$1 - \varepsilon$	0.70	0.86	0.88	0.91	0.79
$\langle b_{\text{ext}} \rangle / \langle b_{\text{int}} \rangle$	0.90	0.57	0.53	0.49	0.58

Table 5.1: Estimated opacity of the shutter $1 - \varepsilon$ (Eq. (5.2)), and amount of external background b_{ext} (Eq. (5.3)) relative to the internal contribution b_{int} (Fig. 5.1) for the various measurements inside the black-box.

Lastly, the dependence of the measured external background with the volume V seen by the PMT can be modeled such that $b_{\text{ext}} \propto V^\alpha$. For the measurements inside the black-box, we estimate $\alpha \approx 1$. Nevertheless, without more precise datasets we do not conclude such a linear behavior for larger volumes.

5.2 Standard measurement

5.2.1 Summary of data run

Our standard measurement scheme switches between two positions of the PMT camera distant by $d \approx 7$ cm, “in” and “out” of the central spot of the mirror respectively — and between two optical modes at both positions, i.e. shutter “open” and “closed”. This gives a combination of four measurement configurations, as sketched in Fig. 5.4. Data are taken in the following sequence: (i) *out/open*, (ii) *out/closed*, (iii) *in/open*, (iv) *in/closed*. Because of the driving distance and the diverse commands sent by the slow-control system, it takes ≈ 4.4 min to complete one cycle.

Potential HP signal can be captured with the *in/open* mode, while the *out/open* mode allows us to measure the ambient background^a. The two *closed* modalities enable us to cross-check for eventual systematical drift between the two measuring positions. As we shall prove in Section 5.4, this measuring cycle also turns out to be particularly convenient in reducing the exposure of the PMT to the remaining ambient light and thus keeping its background rate smaller.

^a Care is taken to correct for the differing Field of View between “in” and “out”.

Run v35

Our main analysis is focused on the last run of FUNK, numbered v35, which was taken from March 07 to April 04, 2019 (lasting 27.5 days). Although we shall refer to other measurements for comparison, at times. Due to the acquisition procedure described above, run v35 has an effective live-time of 4×145.3 h. In Fig. 5.5, we summarize the quantities of interest: average

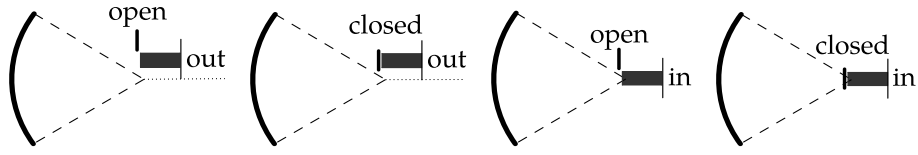


Figure 5.4: Schematics of the four measurement configurations. The data taking cycles from left to right of this figure, with $\Delta t = 60$ s at each mode.

trigger-rate registered with the four configurations of the PMT camera, temperature of the FACT50 housing the PMT, temperature and pressure inside the experimental zone and muon data recorded for the same time span.

A positive difference on the photon rate $\Delta r_{\text{open}} = r_{\text{in/open}} - r_{\text{out/open}}$ would be proxy for a HP signal. Nevertheless, we found that this quantity is uncorrelated with the relative variation of the internal background given by $\Delta r_{\text{closed}} = r_{\text{in/closed}} - r_{\text{out/closed}}$. This implies that the signal detection is mostly limited by external nuisances. Moreover, we already mentioned that typical rates are, here, 3 to 4 times higher than in run v31 (sealed-FACT50).

5.2.2 Background sources

First, it is enlightening to remark that the rates registered with the two *closed* modes, seen in Fig. 5.5, are visibly higher than typical level of the internal background. That is despite the proven full-efficiency of the upgraded optical shutter. As it has been implied, this turns out to be an important systematical effect which we successfully correct for in Section 5.4. Next, we argued in Section 5.1.2 that the background rate depends, to some extent, to the volume directly observed by the PMT. Here, we want to quantify some of the possible sources, although for the moment, we restrict our attention to how they affect the trigger rate.

We consider two main contributors to the measured dark counts, namely originating from thermal and CR induced background, and we provide below conservative estimates of their respective contributions. These sources are described in greater details in Chapter 4. Rather than attempting to give an absolute size to each of them, that is their estimated rates b_{source} , we want to compare their relative variations given by

$$\hat{\sigma}_{\text{source}} = \frac{\sigma(b_{\text{source}})}{\langle b_{\text{source}} \rangle}, \quad (5.4)$$

with the relative variation measured in the data assuming that the data is dominated by the background source in question.

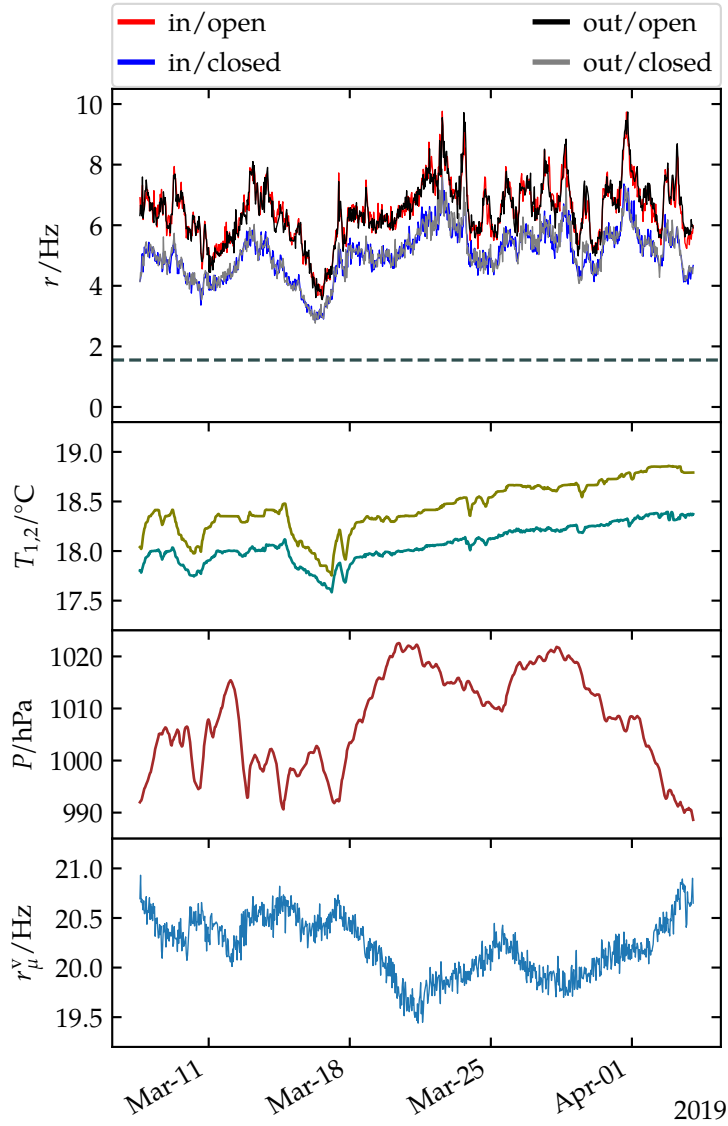


Figure 5.5: From top to bottom: — (i) trigger rate r recorded for each of the configurations drawn in Fig. 5.4, the dashed line indicates the level of internal background b_{int} shown in Fig. 5.1 — (ii) temperatures of the FACT50 housing (T_1 , upper curve) and the experimental hall (T_2 , lower curve) — (iii) atmospheric pressure P — and (iv) rate of vertical muons r_{μ}^v inside the experimental hall. All data are averaged over 10 measurement cycles, i.e. ~ 44 min.

The measured rate r can be written as the sum of several contributions such that

$$r = b_{\text{th}} + b_{\text{ch}} + \dots, \quad (5.5)$$

where b_{th} represents the thermionic emission from the internal parts of the PMT, and b_{ch} arises from the ambient Cherenkov photons. Contributions from time independent or constant components are irrelevant to the following discussion. The assumption that r is dominantly driven by a *single* source means $\langle r \rangle \sim \langle b_{\text{source}} \rangle$. Thus, what we indeed compare is $\hat{\sigma} = \sigma(r)/\langle r \rangle$ with $\hat{\sigma}_{\text{source}} \approx \sigma(b_{\text{source}})/\langle r \rangle$. As reference, we take the two “out” modalities, where no HP signal is expected and for which we observe relative variations of $\hat{\sigma}_{\text{out/open}} = 18\%$ and $\hat{\sigma}_{\text{out/closed}} = 20\%$.

Thermionic emission from the photocathode and dynodes

In Section 4.1, we estimated a linear behavior of the dark counts of thermionic origins with the typical temperatures in the experimental area, and we quoted an average temperature gradient of $m_{\text{th}} = 0.07 \text{ Hz } ^\circ\text{C}^{-1}$. This implies a standard deviation of $\sigma(b_{\text{th}}) = m_{\text{th}}\sigma(T)$ for the associated background rate. We monitored the temperature standard deviation to $\sigma(T) = 0.2 \text{ }^\circ\text{C}$, over the entire duration of run v35, which ultimately yields $\hat{\sigma}_{\text{th}} \lesssim 1\%$.

Cherenkov photons from CR muons

In Section 4.3, we explicitly showed that the rate of CR induced Cherenkov photons is directly proportional to the rate of penetrating muons, implying $\hat{\sigma}_{\text{th}} = \hat{\sigma}_{\text{muon}}$. Here, $\hat{\sigma}_{\text{muon}}$ denotes the relative variation of the muon rate, which we can readily obtain from the available muon data. We find $\hat{\sigma}_{\text{muon}} \approx 2.6\%$, from which we conclude that the background rate cannot be predominantly driven by the present contribution.

Our above estimations lead to relative variations of an order of magnitude smaller for the two considered background components, as compared with the data. In other words, neither of them nor their combination can account for the *variability* in our data and subsequently to our assumption, their fractional contributions to the time varying component of the measured rate are certainly small.

In Section 4.2, we also consider radiations emitted by a black-body like source at room temperature, from the surroundings. However we found that such a thermal source is very unlikely to be our dominant component, in particular because of the very suppressed rate of thermal photons emitted within the range of wavelengths of interest at such temperatures ($\sim 20 \text{ }^\circ\text{C}$). In addition, it is worth noticing that the quantum efficiency of the PMT decreases rapidly in the Infrared (IR) spectrum, where the thermal Planck spectrum actually begin to rise (at room temperature).

Furthermore, thanks to the excellent environmental stability achieved within the experimental area, other possible temperature-dependent sources

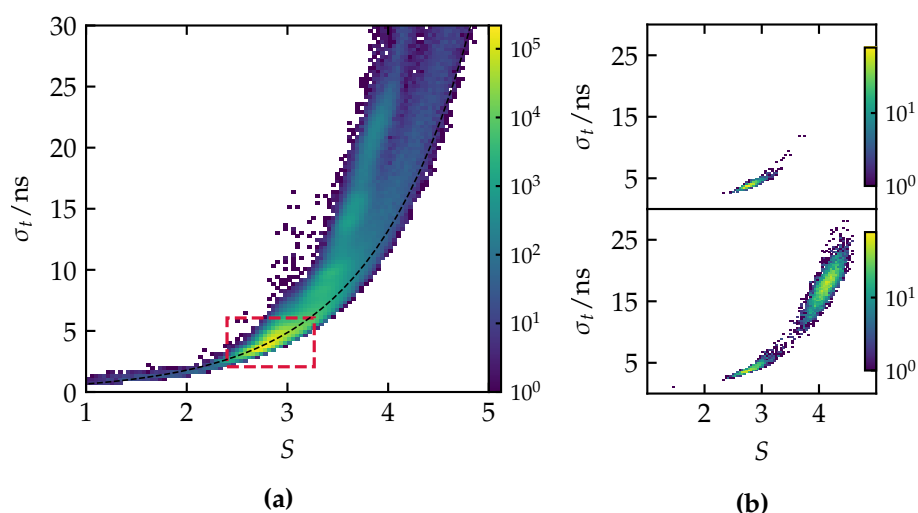


Figure 5.6: (a) 2D distribution of the information entropy S and width σ_t of pulses taken from the measurement *out/open*. The dashed red rectangle corresponds to the formerly defined ROI in Fig. 3.15, which most likely contains SPE signals, and containing $\sim 88.8\%$ of all pulses in this case. The dashed black line is indicative of the expectation for pulses with Gaussian shape in time, as exemplified in Fig. 3.14(b). (b) Same as (a) but for the two settings highlighted in Fig. 3.11, plotted here for visual comparison. The top figure corresponds to the optimal intensity of the LED chosen for SPE study, while the bottom one illustrates a higher setting already presented in Fig. 3.16.

would rather appear stationary over time. That is for instance the case of the internal background presented in Fig. 5.1, which exhibits a stable rate with only 10% fluctuation, since it is dominated by thermionic effect.

On a different matter, we also checked for eventual correlations between the trigger rates, dust particles in the air and potential reflecting surfaces (other than the mirror) but we found no significant connection. Hence at this point, we can only speculate about other possible sources, e.g. residual Radon in the air, etc.

5.2.3 Event selection

So far, we mainly discussed about trigger rates. Let us however recall that our objective is to count single-photon events and that demands a powerful SPE pulse discrimination. In Section 3.2.4, we developed a model independent approach to identify individual SPE events based on the calibration data run. By contrast to generic model or template fits, this method allows us estimate the full SPE statistics without having to apply hard cuts on the pulse charges or amplitudes. Our technique consists of parameterizing all pulses

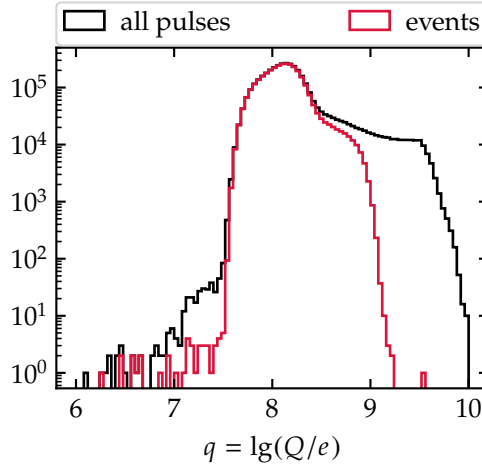


Figure 5.7: Distribution of the anode charge Q before and after event selection, as explained in Fig. 5.6(a) and again applied to the measurement *out/open*.

with respect to their time distributional widths σ_t and their information entropies S , defined in Eqs. (3.6) and (3.7) respectively. As argued, these combined parametrization results into a powerful pulse-shape discriminator. The final SPE phase space was obtained in Fig. 3.15 after dedicated SPE study with a faint flashing LED source. This phase space defines our ROI.

The result is shown in Fig. 5.6(a) where we applied the ROI to the *out/open* data as an example. For all four measuring modalities, the selection efficiency is close to 90%. We note that the preliminary cut based on pulse rise-times t_{rise} , presented in Fig. 3.12 and aimed at suppressing specious triggers, is also applied prior to the ROI. However, no pre-selection is imposed with respect to their trigger-times. That is, we consider all pulses to the extent that they are identified as SPE signals, as we shall argued in a moment. From now on, we shall refer to the selected pulses as *events*.

Finally, we also show in Fig. 5.7 the distribution of the collected anode charge Q before and after event selection, where as promised, we observe a smooth truncation on the charge. Both low and high-charge events associated to poorly and optimally amplified SPE, respectively, are thereby taken into account while low-charge pulses due to electronic noises and high-charge pulses likely due to particle showers are being discarded.

“All-event” counting

Our discussion in Section 5.2.2 led us to conclude that the dominant component of the background is yet to be understood. In all cases, without the presence of active background-vetoes^b, our potential for signal detection remains mostly limited by background statistical fluctuations. In Section 5.6,

^b E.g. Muon shield, Cryogenic temperature, etc.

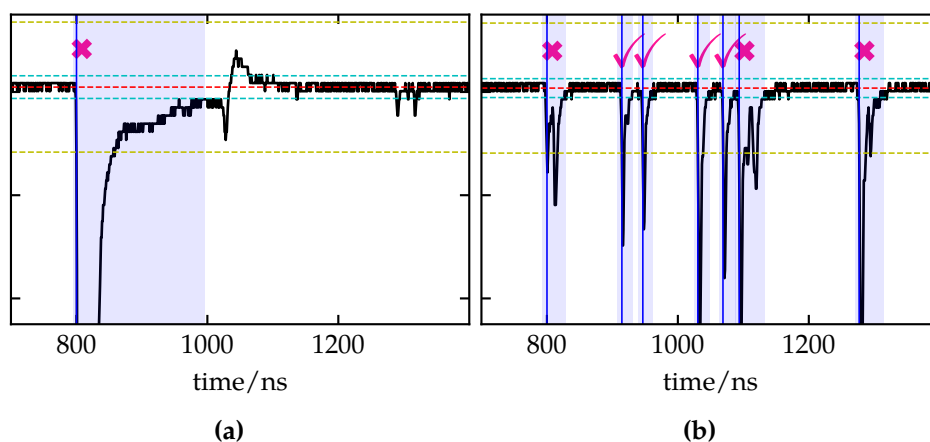


Figure 5.8: (a) Example of a huge pulse caused by coincidental photon hits and rejected by the ROI, as indicated by the pink cross-mark. (b) Example of multiple pulses captured within a the same trace window and likely the result of shower event, but would also include afterpulses and potential reflections by the mirror. Accepted events are tagged by the pink check-marks. The other elements of the plots are the same as in in Fig. 3.9.

we will address systematical uncertainties. However for the same reason, we shall consider all selected pulses or events regardless of their origins (afterpulsing, ambient background or uncorrected systematical effect) because we cannot make distinction between them apart from the SPE criteria. Then ultimately, our limit is evaluated from the total statistical fluctuations measured in the data. On the other hand, in case we find excess of events, it is possible to verify its Dark Matter (DM) nature by observing a seasonal movement in the signal spot^c. This can be achieved thanks to the directional sensitivity of a dish setup (see Section 2.4.2).

^c Although not in the signal rate.

Let us recall that for each trigger the Picoscope digitizer capture a trace of $1.6 \mu\text{s}$. Such a trace is long enough to contain multiple pulses, as it has already been implied. In Fig. 5.8, we show examples of traces to illustrate our above statement on an “all-event” selection. There are however at least two alternatives to this choice. One would be to only consider the number of triggers but this is obviously insensitive to any SPE arguments. The other one would be to only account for traces which contain a single event. Although by doing so, we would artificially and blindly remove events associated to afterpulses, reflected photons from the mirror (see Section 5.6.3), delayed photons from the PMT memory (see Section 5.4) or from other correlated background, and most importantly, alongside with possible HP signal, which would all leave the same event signature in the output trace of the PMT. In addition, as we shall reveal in Section 5.3 the data exhibits a strong non-Poissonian component.

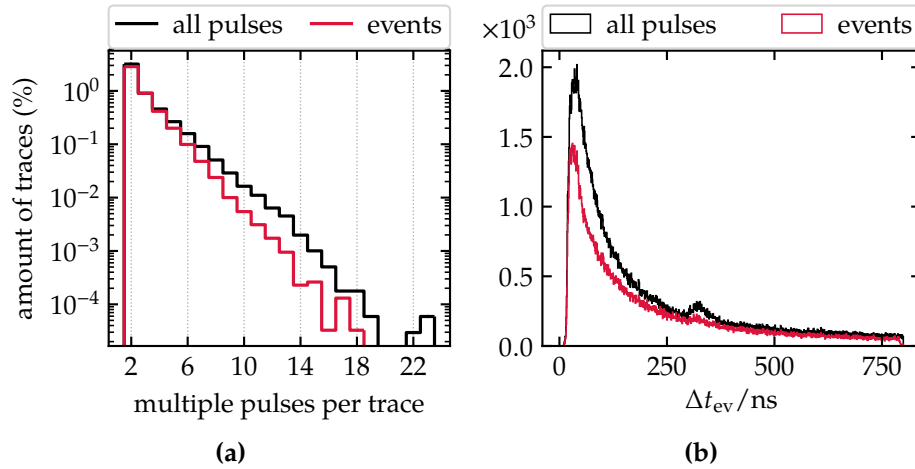


Figure 5.9: (a) Fractional amount of traces containing multiple pulses. Data is taken from the *out/open* configuration of run v35. (b) Distributions of timings between consecutive events within the same trace, for the same dataset.

The number of traces which contain multiple events is estimated between 4% and 6% for all four measurement configurations, suggesting that they are mostly of background origins. For the data *out/open*, the distribution of such traces is plotted in Fig. 5.9(a). Moreover, we notice that these percentage ratios are slightly higher compared to the sealed-FACT50 result shown in Fig. 5.2(b). The reason for this is that we indeed observe more events per trace and not only more triggers. It also suggests that these multiples events are not only caused by direct hits of CR muons — in which case we might have discarded them — but also by the ambient background, the increased number of afterpulses, and other non-trivial systematical effects such as the mirror reflections or the PMT memory, mentioned earlier. That is again to say that we should not readily remove them.

^d Event times are relative to the beginning of each individual trace.

In Fig. 5.9(b), we plot the distribution of time differences^d between two consecutive events Δt_{ev} within the same trace window, before and after event selection. This is again to illustrate the removal of (time-correlated) non-SPE pulses seen in the same trace (see example of quality cuts in Fig. 5.8). The event selection is more effective at shorter scale of Δt_{ev} , which we would expect from the removal of shower-like events. In particular, the peak at $\Delta t_{ev} \sim 280$ ns is relatively smoothed-out after the cuts. This peak fits the time frame of afterpulses due ionization of the residual gases in tube, as explained in Section 4.1. When the ionized molecules bombard the photocathode, multiple secondary electrons may get released and produce a signal which does not fulfill our SPE criteria. We will return with a close-look analysis of this distribution in Section 5.6.3.

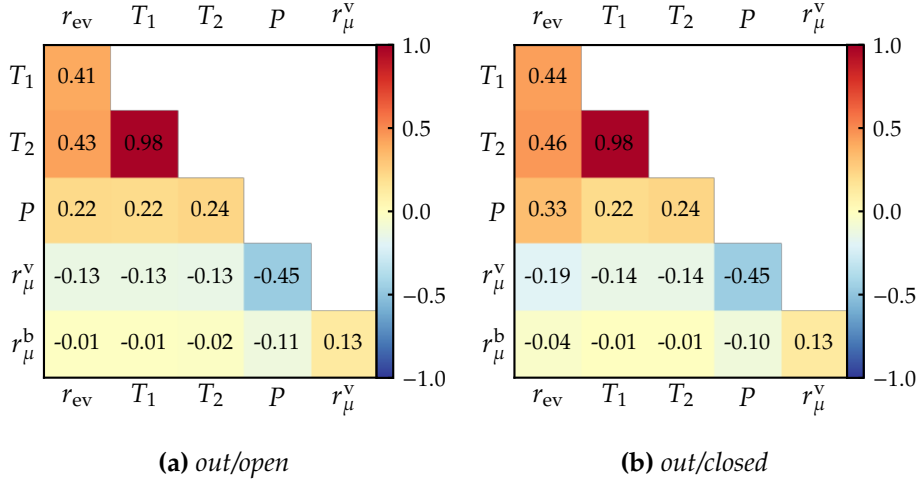


Figure 5.10: Correlation coefficients between all measured quantities during run v35: rate of events r_{ev} , temperature of the FACT50 housing T_1 , temperature of the experimental hall T_2 , rate of vertical muons r_{μ}^v and rate of muon bundles r_{μ}^b . The color-map is used to visualize the strength and sign of the correlations.

5.2.4 Correlation study

For completeness, we evaluate the Pearson correlation coefficient κ given by

$$\kappa(x, y) = \frac{\sum_i (x_i - \langle x \rangle)(y_i - \langle y \rangle)}{\sqrt{\sum_i (x_i - \langle x \rangle)^2} \sqrt{\sum_i (y_i - \langle y \rangle)^2}}, \quad (5.6)$$

for each pair of observables (x, y) plotted in Fig. 5.5. The result is displayed in Fig. 5.10 for the two *out* modalities which measure the background of the experiment. Notice that we used unbinned dataset, i.e. sampled every one-full cycle (~ 4.4 min). The event rate r_{ev} , the two temperatures $T_{1,2}$ and the pressure P are averaged over each 60 s acquisition window. Otherwise, the rate of downward muons r_{μ}^v (vertical coincidence) and muon bundles r_{μ}^b (horizontal coincidence) are interpolated at appropriate timestamps to match the FUNK DAQ sampling time, since they are provided independently by the FUNK MUON monitoring system. Let us comment on the relevant aspects of these correlations.

- (i) The event rate is slightly correlated with the temperature. Later we find that this correlation can be, in part, associated with the PMT memory.
- (ii) There is a feeble correlation between the event rate and the pressure, which could follow from a non-linear dependence of the speculated ambient background with the local pressure.

- (iii) The event rate seems to be anti-correlated with the muon rate. Yet, on top of the curious negative sign which could result from the unavoidable interpolation of the muon data, we retain any physical meaning of such an anti-correlation, in particular because we already rejected background process induced by CR muons as the driving component of the temporal variation of the measured background.
- (iv) It is also interesting to notice that the muon rate is slightly anti-correlated with the local pressure^e. This effect is well-known for GeV muons (see for e.g. [96]) and is mainly attributed to atmospheric conditions traced back at the production point of muons (at ~ 15 km altitude). Higher pressure means increase in the air density, which for charged kaons and pions translates into a higher interaction probability and therefore a lower decay probability [97]. For the muons^f, it implies that they are created with less energy and thus a reduced survival probability to reach ground.
- (v) A similar argument goes for the temperature dependence of the muon rate, although it is strictly not applicable to the temperature measured in our laboratory. As explained in Section 3.2.6, the temperature effect rather involves an effective temperature evaluated from the top and along varying depths of the atmosphere. That is to say, the apparent anti-correlation observed between the muon rate and the temperature data should not be misinterpreted in this way.
- (vi) Temperature and pressure also exhibit a slight correlation. Although, we note that the experimental hall is continuously air-conditioned making such correlation less meaningful.
- (vii) The two temperatures are strongly correlated, as expected, and it is simply reflecting a good cross-calibration of the two sensors.

^e Similar anti-correlation were, for instance, measured by the Katrin experiment (with $\kappa = -0.6$ [118]), which is located at the same campus site as FUNK.

^f The production channels are given in Eq. (4.6)

Moreover, we also correlated the event rate with external environmental parameters, generously provided by IMK[§], such atmospheric temperature and pressure at 200 m, global solar radiation and radiation reflected by ground surface. Nevertheless, apart from the aforementioned anti-correlation with the pressure, we did not find any significant correlation between these variables and measured event rate. On the other hand, these are just evidences of the very good isolation of the experimental hall.

Finally, it is instructive to check for an eventual day/night effect. For this purpose, we consider the relevant differences of event rate between the four measurement configurations, i.e. between the two measuring positions $\Delta r_{\text{open}} = r_{\text{in/open}} - r_{\text{out/open}}$, $\Delta r_{\text{closed}} = r_{\text{in/closed}} - r_{\text{out/closed}}$, and between the

[§] Institut für Meteorologie und Klimaforschung, KIT.

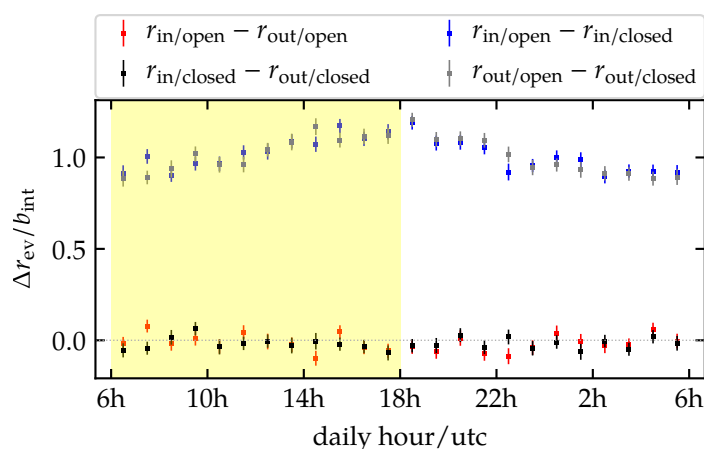


Figure 5.11: Differences of event rate Δr_{ev} between the four measurement configurations and relative to the internal background b_{int} . Data are split daily and binned hourly. Error-bar corresponds to standard error of the mean, σ/\sqrt{n} , where σ is taken from the standard deviation per bin of size n . The shaded region indicates a simplified approximation of daytime.

two optical modes $\Delta r_{\text{in}} = r_{\text{in}/\text{open}} - r_{\text{in}/\text{closed}}$, $\Delta r_{\text{out}} = r_{\text{out}/\text{open}} - r_{\text{out}/\text{closed}}$. The result is displayed in Fig. 5.11, where we split the data into daily intervals and then binned them hourly. Since we do not observe a significant diurnal effect, we discard once for all any hypothesis of light leak through the shielding structure of the experimental zone. We will perform a more detailed frequency analysis in Section 5.5.

For the differences Δr_{open} and Δr_{closed} between “in” and “out”, contributions from the internal background and other constant components are expected to cancel out. As seen from Fig. 5.11, both of them appear to be compatible with zero within statistical uncertainties, indicating a good control of systematical effects. This can be confirmed by observing that the differences between “open” and “closed” are compatible with each other, $\Delta r_{\text{in}} \sim \Delta r_{\text{out}}$. Lastly, we reiterate that the HP signal shall be resolved from the difference Δr_{open} where systematical effects are appreciable and we may also expect an average cancellation of the speculated ambient background.

5.3 Deviation from homogeneous Poissonian process

From now on, unless otherwise stated and for all relevant quantities, we always talk about *events*. Those are pulses which has been cleared by the SPE-like filters presented in Section 5.2.3. In Fig. 5.3(a), we already hinted that the width of the count distribution with our standard measurement is sensibly larger compared to the measurements inside the small black-box, and we

attributed this observation to a volume effect. Such a feature is known as overdispersion in the literature. For run v35, we observe a variance-to-mean ratio of $\sigma^2/\mu \sim 14$ for the number of events per minute recorded with all four measuring modalities.

The recorded events also exhibit another non-Poissonian feature, which relates to correlations on short-time scale. Let us insist that we are referring here to correlations between events themselves, i.e. on the basis of their arrival times, and not to correlations of counts between the measurement configurations nor with other parameters such as those described in Section 5.2.4. While the overdispersion can be explained by admitting a nonhomogeneity in the traditional Poisson distribution, the arrival times of events still depend on the actual stochastic process in play. We discuss these two distinctive features in this section.

5.3.1 Overdispersion

The Negative Binomial distribution

The Negative Binomial is a discrete probability distribution, frequently used as an alternative to the Poisson distribution to describe counting statistics in case where the sample variance is larger than its mean [119]. We briefly review the basic properties of this distribution. There are number of ways to formally derive and interpret the Negative Binomial [120]. For instance, as the sum of N independent, identically and logarithmically distributed random variables X_i where N is also random and follows a Poisson distribution^h.

^h Such a distribution is known as Compound Poisson.

From a phenomenological consideration, it might be more insightful to view the Negative Binomial as a Poisson distribution $\text{Poi}(\gamma)$ with some heterogeneityⁱ in its rate parameter γ such that $\gamma \sim \text{Gamma}(a, \theta)$ where a and θ are the shape and scale parameters of the Gamma distribution, respectively. Concretely, the resulting marginal distribution P , for a discrete random variable X , is given by

ⁱ For homogeneous Poisson, the parameter γ is a constant.

$$\begin{aligned}
 P(X=k) &= \int_0^\infty d\gamma \text{Poi}(k; \gamma) \text{Gamma}(\gamma; a, \theta) \\
 &= \int_0^\infty d\gamma \left(\frac{\gamma^k e^{-\gamma}}{k!} \right) \left(\frac{\gamma^{a-1} e^{-\gamma/\theta}}{\Gamma(a)\theta^a} \right) \\
 &= \frac{1}{k! \Gamma(a)} \left(\frac{1}{\theta} \right)^a \left(\frac{\theta}{1+\theta} \right)^{k+a-1} \int_0^\infty d\gamma \left(\frac{\gamma(1+\theta)}{\theta} \right)^{k+a-1} e^{-\gamma(1+\theta)/\theta} \\
 &= \frac{\Gamma(k+a)}{k! \Gamma(a)} \left(\frac{1}{\theta} \right)^a \left(\frac{\theta}{1+\theta} \right)^{k+a}, \tag{5.7}
 \end{aligned}$$

where in the last step, we used the Gamma function $\Gamma(z) = \int_0^\infty dx x^{z-1} e^{-x}$. By redefining $a \equiv n$ and $\theta \equiv (1-p)/p$, we obtain the Negative Binomial Distribution $\text{NB}(n, p)$, in its canonical form such that

$$\text{NB}(X=k; n, p) = \frac{\Gamma(k+n)}{k! \Gamma(n)} p^n (1-p)^k, \quad (5.8)$$

where $n > 0$ and $0 < p < 1$. It is often instructive to reparametrize the above distribution in terms of its mean μ and variance σ^2 given by

$$n = \frac{\mu^2}{\sigma^2 - \mu}, \quad (5.9)$$

$$p = \frac{n}{n + \mu}. \quad (5.10)$$

Eq. (5.9) guarantees that $\sigma^2 = \mu + \mu^2/n > \mu$. Subsequently, the distribution has also longer tail compared to the Poissonian version, making it suitable to describe the overdispersion. It is easy to see that for large n , we recover the Poisson distribution. On the other hand, Eq. (5.10) can be written as $p = \mu/\sigma^2$. Thus, its inverse quantifies the variance-to-mean ratio, also called index of dispersion.

Fitting the data

We use Eq. (5.8) to fit event counts k_i registered per one-minute interval, by using an unbinned maximum likelihood method, i.e. by minimizing $-\sum_i \lg \text{NB}(k_i; n, p)$. As an example, let us consider events from the measurement *out/open*. The result is given in Fig. 5.12(a), where the parameter estimates are $n = 28.7$ and $p = 0.07$. These correspond to a mean and variance count of $\mu = 379$ and $\sigma^2 = 5375$, respectively. For comparison, we also plot in the same figure the expected Poisson distribution with the measured mean number of events. Notice that the latter is also the maximum likelihood estimate in this case. We apply the same procedure to the sealed-FACT50 measurements, as seen in Fig. 5.12(b). The fitted parameters are $n = 156.9$ and $p = 0.66$, or equivalently $\mu = 83$ and $\sigma^2 = 126$. Thus, there appears to be remnant of non-Poissonian events even in internal background.

There are studies which associate non-Poissonian behavior to particle showers, for example in the form of muon bundles [121]. As seen in Fig. 3.21, the flux of muon bundles monitored inside the FUNK area is rather suppressed, making them unlikely as a sole explanation of the observed overdispersion.

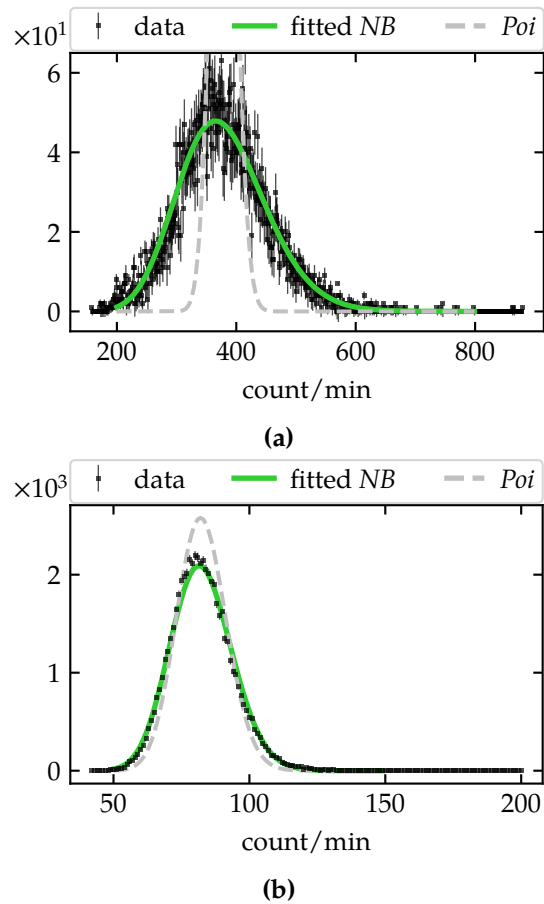


Figure 5.12: (a) Distribution of event counts registered during run v35 with the PMT camera *out/open*, fitted with the Negative Binomial $NB(n, p)$ defined in Eq. (5.8) and superimposed with a Poisson distribution $Poi(\gamma)$ to emphasize on the observed deviation. (b) Same as above but for run v31 with the sealed-FACT50 condition. Here, the Negative Binomial distribution is only marginally better compared to the Poisson one.

5.3.2 Correlated events

It might be tempting to think of a stochastic process leading to a Negative Binomial (marginal) distribution. In fact, there are numerous such processes in the literature (see for e.g. [120] and the references therein), including generalized models which account for correlated counts [119]. However, due to our lack of understanding of the actual physical processes in play, we investigated them independently of any models.

We devised special runs during which the Picoscope oscilloscope was replaced by a Caen DT571 digitizer, calibrated to the same threshold levels (more description in §. Hardware of Section 3.2.3). The advantage with using

this device is that it is relatively easy to retrieve the absolute arrival times of events within the $\Delta t = 60$ s data-taking. In addition, since we are only interested in background processes, the PMT was positioned “out” of the center of curvature of the mirror and the shutter was always kept “open”. For the data used in the following analysis, the measurement lasted overall 10 days. The recorded sample contains $\sim 4.95 \times 10^6$ pulses were tagged, then processed off-line. About 87.4 % of them were identified as events according to our SPE criteria.

For an homogeneous Poisson process, with known rate γ , the interarrival time or waiting time t between two successive events follows an exponential distribution such that $f(t) = \gamma e^{-\gamma t}$. A suitable transformation^j can be achieved with

$$\tilde{t}(t) = 1 - e^{-\gamma t}, \quad (5.11)$$

which maps shorter and longer waiting times towards 0 and 1, respectively. Noting that the inverse transformation is given by $\tilde{t}^{-1}(u) = -\lg(1 - u)/\gamma$, the distribution g of the transformed variable \tilde{t} is

$$\begin{aligned} g(\tilde{t}) &= \frac{dt}{d\tilde{t}} f(t) \\ &= \frac{d}{d\tilde{t}} (\tilde{t}^{-1}(\tilde{t})) f(\tilde{t}^{-1}(\tilde{t})) \\ &= \frac{1}{\gamma(1 - \tilde{t})} \gamma e^{-\gamma \tilde{t}^{-1}(\tilde{t})} = 1, \end{aligned} \quad (5.12)$$

where we recognize a uniform distribution $\text{Unif}(0, 1)$.

Hence, we can use this property to observe eventual deviations in the distribution of the measured waiting times, transformed under Eq. (5.11). We apply such a transformation to the collected dataset, as presented in Fig. 5.13. From this figure, it is clear that there is a substantial clustering of correlated events at short timescale, thereby confirming that a non-Poissonian process is taking place.

Such observations have been formerly reported by other experiments employing different variants of low-noise PMTs assembled into more complex optical modules, for e.g in deep ice [107] or in deep ocean [122]. Although the behavior has been clearly associated correlated dark noises, the main physical origin remains ambiguous. For instance, scintillation of the glass envelope, induced by decaying traces of radioisotopes present in glass, have been suggested in [106, 123] (also see Section 4.1). Alternatively, there is also an argument about electron bursts due to unconventional non-thermal effect which has been observed, in particular, for PMTs at cryogenic temperatures [124]. Naturally, there are known effects such as afterpulses or CR induced photon bursts, which contribute in part to the observed correlated

^j Known as Probability Integral Transform.

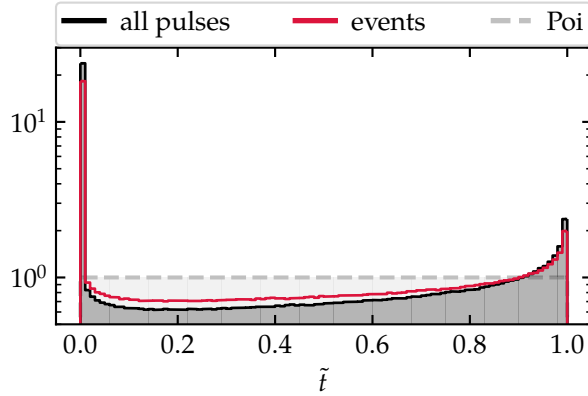


Figure 5.13: Distribution of event waiting-times transformed under the cumulative exponential distribution function, as defined in Eq. (5.11). Both distributions before and after event selection are shown. The dashed grey line is the expectation for an homogeneous Poisson process.

events. However, we have argued that they do not contribute significantly to our background. Additionally, those which do not fulfill the SPE criteria are immediately suppressed after event selection. This suppression was illustrated in Fig. 5.9(b), where we used the relative interarrival times between events captured in the same trace.

The next step is to investigate the timescale at which the clusterings occur. We may be able recover the Poissonian nature of the counting process by applying a selective dead-time on consecutive events. A classical way to achieve that consists of imposing a fixed or non-paralyzable dead time t_{dead} . This means we do not count the next event if it occurs within a time $t < t_{\text{dead}}$. In terms of probability, it means $f(t) = \gamma e^{-\gamma(t-t_{\text{dead}})}$ for Poissonian waiting times $t \geq t_{\text{dead}}$ and with a rate γ yet to be determined. Using this distribution, the expected event rate γ' estimated from the dead-time corrected dataset is given by $1/\gamma' = \int_{t_{\text{dead}}}^{\infty} dt t f(t) = 1/\gamma + t_{\text{dead}}$. In other words, the underlying Poisson process has a rate of

$$\gamma = \frac{\gamma'}{1 - \gamma' t_{\text{dead}}}. \quad (5.13)$$

A suitable transformation can then be applied such that

$$\tilde{t}(t) = 1 - e^{-\gamma(t-t_{\text{dead}})}. \quad (5.14)$$

It is easy to prove, in a similar manner as before, that the transformed waiting times under Eq. (5.14) is uniformly distributed between 0 and 1, if they stem from a Poisson process.

In order to quantify the deviation from an uniform distribution $\text{Unif}(0, 1)$, we compute the mean-squared deviation MSD, defined as

$$\text{MSD} = \frac{1}{n_{\text{bins}}} \sum_i^{n_{\text{bins}}} (1 - y_i)^2, \quad (5.15)$$

where y_i is the value of the probability distribution of the \tilde{t} -transformed waiting times at the bin i , and as function of the applied dead time t_{dead} . This metric was chosen for the convenience that the expected deviation, in case where events were generated by a Poisson process, is $\text{MSD} = 0$. Furthermore, we normalize the values so that the maximal measured deviation gives $\text{MSD} = 1$. The result is shown in Fig. 5.14(a), where we progressively applied a dead time from 1 ns to 1 s. The same procedure is applied to the registered pulses, before and after event selection. There appear to be two distinct timescales at which visible departures from the Poissonian expectations kick off. In Fig. 5.14(b), we also plot the fractional amount of events remaining after each t_{dead} -cut, and normalized by the total number of pulses collected.

Before going into details, let us notice that by imposing longer t_{dead} , i.e. requiring longer waiting times, we successful recover the Poisson statistics. Of course, this is expected since we are the tail of arrival-time distribution where late-time correlated events are rather unlikely. Then, starting this point on and knowing the total duration T of the measurement, we can infer the actual number of events $N = \gamma T$ (i.e. without dead time) that would indeed reproduces the observed number of events $N' = \gamma' T$ for each dead time correction applied. If the events were generated by a Poisson process with rate γ , it is easy to obtain γ' by inverting Eq. (5.13). These give the two dashed gray lines in Fig. 5.14(b) which correspond to the Poissonian expectation for both datasets before and after event selection.

Figs. 5.14(a) and 5.14(b) exhibit two significant departures from the Poissonian reference, at millisecond and microsecond timescales, respectively. The first break is likely related to CR-shower induced background (causing ionization or scintillation), possible luminescence of the glass envelope of the PMT induced by radioactive sources [107] as mentioned earlier, or also from environmental γ -rays [125]. We note that these events appear in separate traces since the Caen digitizer captures a window of 1.6 μs , to conform with the Picoscope. The second break includes presumably Cherenkov radiation (from single muons) and afterpulses due to ionization of residual gases in the tube. Nevertheless for the latter, we mentioned that they normally amount to less than 1 % of the event rate, for our PMT. It also appears that the SPE selection is mostly efficient below the microsecond pulses. In fact, this is because of the removal of non-Poissonian arrival times such as bursts

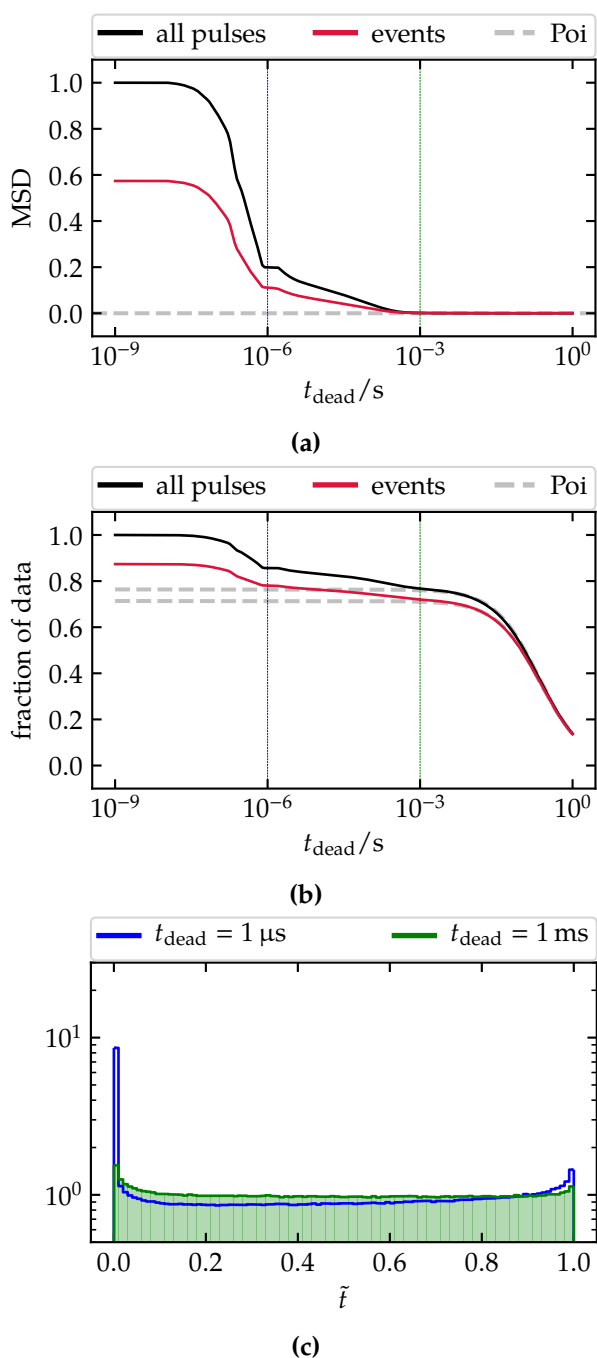


Figure 5.14: (a) Mean-squared deviation, defined in Eq. (5.15), between a uniform distribution and the distribution of the \tilde{t} -transformed waiting times according to Eq. (5.14). (b) Efficiency of the dead time selection, normalized by total number of pulses. In both plots, the dashed gray lines indicate the expectation for an homogeneous Poisson process. (c) Similar to Fig. 5.13 and with the same axis scale, illustrating the millisecond and microsecond breaking scales from a Poisson process. More details in the text.

of photon as illustrated in Fig. 5.8. There is also a third break, less visible and between 10-100 ns, which matches the timescale of afterpulses due to secondary emissions and possible reflections from the mirror. In addition, the historical background of the PMT, addressed in the next section, would to some extent contribute to these correlated backgrounds. Although, the most probable timescale is rather uncertain. Lastly, let us note that roughly 23% and 14% of events are clustered on scales below ~ 1 ms and ~ 1 μ s, respectively.

Ultimately, we do not expect HPs to induce such correlated events. Nonetheless, in order to provide a conservative limit on the mixing parameter, we do not apply a dead time selection nor any other other rejection based on the arrival time of pulses.

5.4 Memory effect

As we often mentioned, the typical rate registered with the *closed* camera is clearly higher than its typical internal background b_{int} , which were independently monitored during the sealed-FACT50 run (v31). On one hand, it should be noted that such a behavior were also observed with other measurements, and it is not a defining feature of the analyzed run (v35). On the other, we also know from extensive test runs that the upgraded Teflon-coated blades of the optical shutter offer the same performance as the thick metal lid, formerly used to seal the FACT50 housing of the PMT. Additionally, as seen in Fig. 5.5, the evolution of the *closed* rates over time follows remarkably the *open* ones, indicating a non-negligible correlation between the two modes.

5.4.1 Characterization of the FUNK PMT

For run v35, the average event rates are evaluated to $\langle r_{\text{open}} \rangle \sim 4.5 \langle b_{\text{int}} \rangle$ and $\langle r_{\text{closed}} \rangle \sim 3.5 \langle b_{\text{int}} \rangle$, for both positions “in” and “out” of the central spot of the mirror. The differences between the four measuring modalities are shown in Fig. 5.11. These numbers suggest that there are some residual background seen by PMT, which indubitably remains even after we completely close the shutter, and is intimately related to level of illumination when the shutter was open. For future reference, we will refer to this residual light as historical background.

In fact, this is a known intrinsic feature of PMTs [126], which we call *memory effect*. It relates to the level of excitation of the photocathode and glass envelope of the PMT, in the past. Hence, the effect is usually noticeable in case of high illumination. That is the case if the PMT has been irradiated by a strong light source, either suddenly or for a prolonged period, resulting in a rapid increase of its dark current. Then, after deprivation from any

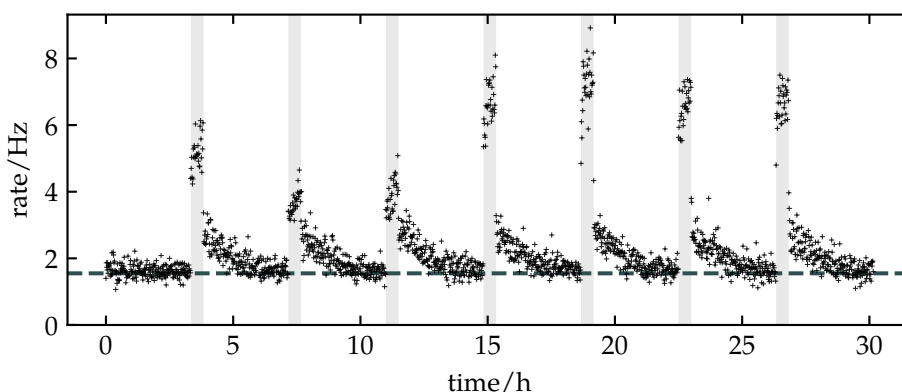


Figure 5.15: Example of trigger rates measured with the camera *closed* for 200 min and *open* for 30 min (corresponding to the gray shaded zone). The dashed line indicates the nominal level of dark counts, measured from run v31.

external light sources, it may take from a few hours to a few days [103], to reach again the nominal level of dark current, depending on the intensity and duration of the exposure. For instance, we noted that after each visit of the experimental area, which inevitably brings a certain level of illumination, the FUNK PMT needed several hours to reduce and stabilize the rate.

What is mostly astounding in the present case is that, we seem to observe the same effect even though the exposure to external background, not only amounts to a few photons/s, but is also intermittently limited to intervals of $\Delta t = 60$ s during our standard measurement^k.

^k The measuring sequence is sketched in Fig. 5.4.

Measurement

To clarify the actual extent of the historical background, we devised an independent measurement during which we initially kept the shutter *closed* for 200 min, then it was switched *open* for 30 min. The camera was always positioned “out” of the central spot of the mirror. This measuring sequence was repeated several times, continuously, and we recorded the number of triggers in the same intervals of 60 s, to conform with the standard run.

The outcome of this measurement is plotted in Fig. 5.15, where we observe an initial fast jump of the rate, upon opening the shutter, after which the rate continues to increase slowly, as the photocathode is left exposed to the ambient background light. Then after closing the shutter, it takes on a timescale of an hour for the rate to decay back to the nominal value of the internal background of the PMT. From this experiment, we conclude that the FUNK PMT memorizes remarkably well the past illumination. Moreover, it is striking that the historical background extends over such long periods,

even with our particularly low-noise detector and despite the very faint and limited exposure. Although such a property might find utility in other applications, it is definitely a pitfall for the purpose of instantaneous photon counting.

5.4.2 Model

Based on these findings, we propose the following model to describe the response rate $r(t)$ of the PMT to an instantaneous input signal $s(t)$,

$$r(t) = s(t) + \alpha \int_{-\infty}^t dt' K(t', t) s(t'). \quad (5.16)$$

Here, in addition to the instantaneous rate, we folded an historical component described by the memory kernel $K(t', t)$ to account for the detector response to past illumination. α is called the memory efficiency. As a memory kernel, we choose an exponentially decaying function with an average decay-time τ , such that

$$K(t', t) = \frac{1}{\tau} \exp\left(-\frac{t-t'}{\tau}\right). \quad (5.17)$$

The parameters α and τ , both positives, are characteristics of the PMT which we determine later. To get feel of this model, let us study the detector response to various forms of the input signal.

Steady input

Let us first consider a steady illumination s_{DC} , i.e. constant and continuous, which we assume the PMT has been observing for a long enough duration. In this case, the output rate given by Eq. (5.16) is also constant at all time, with a value

$$r_{\text{DC}} = (1 + \alpha)s_{\text{DC}}. \quad (5.18)$$

This means that each detected photon leaves an historical rate of size α . The measured rate is directly increased by the same amount. For instance, if we regard the internal background as a steady illumination, it implies that the instantaneous contribution of the noise and dark current is indeed suppressed by a factor of $1/(1 + \alpha)$.

Periodic input. *open/close*

Let us now consider, aside from the stationary component above, an external illumination, with constant intensity, but periodically blocked by the shutter mechanism. We suppose that the measurement begins at $t = t_0$, i.e. we do not know the amount of illumination before t_0 . We split the acquisition time

in regular interval $[t_i, t_{i+1})$, where $t_{i+1} = t_i + \Delta t$ for $i = 0, 1, \dots$ and following a sequence *open/closed* shutter. Then, the instantaneous input signal can be written as follows,

$$s(t) = \begin{cases} s_{\text{neg}} & \text{if } t < t_0 \\ s_{\text{open}} & \text{if } t_{2i} \leq t < t_{2i+1} \quad (\text{shutter open}) \\ s_{\text{closed}} & \text{if } t_{2i+1} \leq t < t_{2i+2} \quad (\text{shutter closed}) \end{cases} \quad (5.19)$$

s_{neg} represents the unknown state of the signal prior to the beginning of the measurement^l, and for simplicity, it is taken as constant. s_{open} and s_{closed} are the measured external inputs with the shutter *open* and *closed*, respectively. A full blocking efficiency means $s_{\text{closed}} = 0$. Nevertheless, let us keep the expression general for the moment.

^l For instance, the PMT could have been irradiated by direct light-source before the measurement.

In this model, the time dependence of the memory kernel only influences the output rate of the detector up to a period of the order of the decay time τ . We are interested in finding a suitable expression for the convoluted part of Eq. (5.16) — let us denote by $h(t)$ — for large time $t \gg \tau$. Using the signal given in Eq. (5.19), the integral response at some time $t_m \in [t_i, t_{i+1})$ reads

$$\begin{aligned} h(t_m) &= \frac{1}{\tau} \left[\int_{-\infty}^{t_0} dt' + \int_{t_0}^{t_i} dt' + \int_{t_i}^{t_m} dt' \right] s(t') e^{-(t_m-t')/\tau} \\ &= h_{\text{neg}} + h_i + h_m, \end{aligned} \quad (5.20)$$

where

$$\begin{aligned} h_{\text{neg}} &= \frac{1}{\tau} \int_{-\infty}^{t_0} dt' s(t') e^{-(t_m-t')/\tau} \\ &= s_{\text{neg}} e^{-(t_m-t_0)/\tau}, \end{aligned} \quad (5.21)$$

$$\begin{aligned} h_i &= \frac{1}{\tau} \sum_{j=0}^{i-1} \int_{t_j}^{t_{j+1}} dt' s(t') e^{-(t_m-t')/\tau} \\ &= e^{-t_m/\tau} \sum_{j=0}^{i-1} s_j (e^{t_{j+1}/\tau} - e^{t_j/\tau}), \end{aligned} \quad (5.22)$$

$$\begin{aligned} h_m &= \frac{1}{\tau} \int_{t_i}^{t_m} dt' s(t') e^{-(t_m-t')/\tau} \\ &= s_i (1 - e^{-(t_m-t_i)/\tau}). \end{aligned} \quad (5.23)$$

Here, $s_j = s(t_j)$ denotes the constant input over the interval $[t_j, t_{j+1})$ and taking values s_{open} or s_{closed} , depending on the shutter status.

Let us consider a particular time $t_m = t_i = t_0 + i\Delta t$, where there are exactly $i/2$ cycles of *open/closed* measurements. First, notice that Eq. (5.23) then vanishes. For large time $t_i \gg \tau$, the contribution from Eq. (5.21) prior to the measurement can also be neglected. The historical contribution comes from all the $i/2$ complete cycles, which we compute from Eq. (5.22) as,

$$h_i = e^{-t_i/\tau}(e^{\Delta t/\tau} - 1) \sum_{j=i}^{j=i-1} s_j e^{t_j/\tau}. \quad (5.24)$$

The last summation term reduces to the sum of a geometrical series,

$$\begin{aligned} \sum_{j=i}^{j=i-1} s_j e^{t_j/\tau} &= e^{t_0/\tau} (s_{\text{open}} + s_{\text{closed}} e^{\Delta t/\tau} + s_{\text{open}} e^{2\Delta t/\tau} + s_{\text{closed}} e^{3\Delta t/\tau} + \dots) \\ &= e^{t_0/\tau} \underbrace{(1 + e^{2\Delta t/\tau} + e^{4\Delta t/\tau} + \dots)}_{i/2 \text{ terms}} (s_{\text{open}} + s_{\text{closed}} e^{\Delta t/\tau}) \\ &= \frac{e^{t_i/\tau} - e^{t_0/\tau}}{e^{2\Delta t/\tau} - 1} (s_{\text{open}} + s_{\text{closed}} e^{\Delta t/\tau}). \end{aligned} \quad (5.25)$$

Plugging the last expression into Eq. (5.24) and taking again the limit of large time t_i , the integral response from H evaluated at the end of $i/2$ complete cycles is constant and given by

$$H = \frac{s_{\text{open}} e^{-\Delta t/\tau} + s_{\text{closed}}}{1 + e^{-\Delta t/\tau}}. \quad (5.26)$$

Let us note that when $s_{\text{open}} = s_{\text{closed}}$, i.e. a constant illumination not periodically blocked by the shutter, we have $H = 1$ and we successfully recover the result for a steady input given in Eq. (5.18). Considering now a measurement on the next interval, at some time $t_m \in [t_i, t_{i+1})$, Eq. (5.20) can be written as

$$h(t_m) = e^{-(t_m - t_i)/\tau} H + s_i (1 - e^{-(t_m - t_i)/\tau}), \quad (5.27)$$

where we have expressed Eq. (5.22) in terms of Eq. (5.26). To get the full response $r(t_m)$ of the PMT, we add the instantaneous part and account for the memory efficiency α , such that

$$r(t_m) = s(t_m) + \alpha h(t_m). \quad (5.28)$$

From now on, we focus on the case where $s_{\text{closed}} = 0$, i.e. the shutter is fully light-tight. We want the limiting values of the average response rates r_{open} and r_{closed} . Those are easily obtained by computing the average rates over the next intervals $[t_i, t_{i+1})$ and $[t_{i+1}, t_{i+2})$, respectively. Assuming that the decay time τ of the PMT is large compared to the sampling interval Δt , the average rates can be estimated, to a good approximation, at the middle of each respective intervals such that $\bar{t}_i = (t_i + t_{i+1})/2$ and $\bar{t}_{i+1} = (t_{i+1} + t_{i+2})/2$.

- Interval $[t_i, t_{i+1})$, shutter *open*. At the middle of the interval, we have $t_m = \bar{t}_i = t_i + \Delta t/2$. The response rate is given by

$$\begin{aligned}
 r_{\text{open}} &= s_{\text{open}} + \alpha e^{-\Delta t/2\tau} H + \alpha s_{\text{open}} (1 - e^{-\Delta t/2\tau}) \\
 &= s_{\text{open}} + \alpha s_{\text{open}} \left(\frac{e^{-\Delta t/2\tau} e^{-\Delta t/\tau}}{1 + e^{-\Delta t/\tau}} + 1 - e^{-\Delta t/2\tau} \right) \\
 &= s_{\text{open}} \left[1 + \alpha \left(1 - \frac{e^{-\Delta t/2\tau}}{1 + e^{-\Delta t/\tau}} \right) \right]. \tag{5.29}
 \end{aligned}$$

- Interval $[t_{i+1}, t_{i+2})$, shutter *closed*. At the middle of the interval, we have $t_m = \bar{t}_{i+1} = t_i + 3\Delta t/2$. Since $s_{\text{closed}} = 0$, we only have the historical decay of the past $i + 1$ intervals, so that

$$\begin{aligned}
 r_{\text{closed}} &= \alpha e^{-3\Delta t/2\tau} H + \alpha s_{\text{open}} e^{-\Delta t/2\tau} (1 - e^{-\Delta t/\tau}) \\
 &= \alpha s_{\text{open}} \left(\frac{e^{-3\Delta t/2\tau} e^{-\Delta t/\tau}}{1 + e^{-\Delta t/\tau}} + e^{-\Delta t/2\tau} - e^{-3\Delta t/2\tau} \right) \\
 &= \alpha s_{\text{open}} \left(\frac{e^{-\Delta t/2\tau}}{1 + e^{-\Delta t/\tau}} \right). \tag{5.30}
 \end{aligned}$$

Finally, let us make three remarks. Firstly, as clear from Eq. (5.30) the rate does not immediately go to 0, upon closing the shutter. This is because the PMT still observes the decay of the previous rate. Secondly, comparing Eq. (5.18) with Eq. (5.29) and given the same source of illumination, we find that $r_{\text{open}} < r_{\text{DC}}$. This refers back to our statement at the beginning of Section 5.2, that the shutter effectively reduces the background rate of the PMT by limiting its exposure to the ambient light. Thirdly, this suppression is mostly efficient when $\Delta t \ll \tau$, with $r_{\text{open}} \approx s_{\text{open}}(1 + \alpha/2)$ and $r_{\text{closed}} \approx \alpha s_{\text{open}}/2$. The difference between the two is constant and gives directly the instantaneous input signal s_{open}^m . In the converse case where $\Delta t \gg \tau$, the decay would happen almost instantaneously, resulting into $r_{\text{open}} \approx r_{\text{DC}}$ and $r_{\text{closed}} \approx 0$.

^m This is indeed the behavior observed in Figs. 5.5 and 5.11.

Periodic input. *out/open – out/closed – in/open – in/closed*

As a last example, it is instructive to study the more general case which corresponds to our standard measurement scheme (see Fig. 5.4). We consider again some external illumination, periodically blocked by the shutter, with different intensities “in” and “out” of the central spot of the mirror. In addition, we include internal illumination from the PMT noise and dark

current, also assumed to be different at the two measuring positions. The input signal can be written as

$$s(t) = \begin{cases} s_0 & \text{if } t_{4i} \leq t < t_{4i+1} & \text{out/open} \\ s_1 & \text{if } t_{4i+1} \leq t < t_{4i+2} & \text{out/closed} \\ s_2 & \text{if } t_{4i+2} \leq t < t_{4i+3} & \text{in/open} \\ s_3 & \text{if } t_{4i+3} \leq t < t_{4i+4} & \text{in/closed} \end{cases}, \quad (5.31)$$

where $t_{i+1} - t_i = \Delta t$ and i takes integer values. In this consideration, the inputs s_i 's represent the overall instantaneous component of the background, internal or external. They are assumed to be constant but different for all four measurement configurations. Otherwise, we have neglected other possible irradiations before t_0 , since we are interested in the long run behavior.

We want to find the limiting values of the response rates of the PMT, denoted as $r_0 = r_{\text{out/open}}$, $r_1 = r_{\text{out/closed}}$, $r_2 = r_{\text{in/open}}$ and $r_3 = r_{\text{in/closed}}$. Following a similar approach as in the former example, we can show that

$$\begin{aligned} r_0 &= s_0 K + \alpha f^{1/2} H, \\ r_1 &= s_1 K + \alpha f^{1/2} [fH + s_0(1 - f)], \\ r_2 &= s_2 K + \alpha f^{1/2} [f^2 H + (s_0 f + s_1)(1 - f)], \\ r_3 &= s_3 K + \alpha f^{1/2} [f^3 H + (s_0 f^2 + s_1 f + s_2)(1 - f)], \end{aligned} \quad (5.32)$$

where

$$\begin{aligned} f &= e^{-\Delta t/\tau}, \\ K &= 1 + \alpha(1 - f^{1/2}), \\ H &= (s_0 f^3 + s_1 f^2 + s_2 f + s_3) \left(\frac{1 - f}{1 - f^4} \right). \end{aligned} \quad (5.33)$$

Let us consider appropriateness of these equations. When $s_0 = s_2$ and $s_1 = s_3$, i.e. identical signal "in" and "out", we have $H = (s_0 f + s_1)/(1 + f)$ which is identical to Eq. (5.26). In addition, if $s_1 = 0$, it is easy to check that we correctly reproduce Eqs. (5.29) and (5.30).

In the limit of $\tau \ll \Delta t$, the response rates can be simplified at first order as follows,

$$\begin{aligned} r_0 &= c_0 s_0 + c_1 s_1 + c_2 s_2 + c_3 s_3, \\ r_1 &= c_3 s_0 + c_0 s_1 + c_1 s_2 + c_2 s_3, \\ r_2 &= c_2 s_0 + c_3 s_1 + c_0 s_2 + c_1 s_3, \\ r_3 &= c_1 s_0 + c_2 s_1 + c_3 s_2 + c_0 s_3. \end{aligned} \quad (5.34)$$

The values of the coefficients are $c_0 = 1 + \alpha/4$, $c_1 = \alpha(1 - \Delta t/\tau)/4$, $c_2 = \alpha/4$ and $c_3 = \alpha(1 + \Delta t/\tau)/4$. The difference Δr_{open} between the two “open” modes is

$$\Delta r_{\text{open}} = r_2 - r_0 = (s_2 - s_0) - \frac{\alpha}{2\tau}(s_3 - s_1). \quad (5.35)$$

We will use these results in Section 5.6.3.

5.4.3 Fitting

We estimate the memory efficiency α and decay time τ of the FUNK PMT from the measurement described in Section 5.4.1, during which the camera was repeatedly closed for 200 min, then open for 30 min (see Fig. 5.15). We refer to these periods as “closed-bin” and “open-bin”, respectively, to distinguish them from the one-minute sampling interval. The procedure consists of fitting the number of counts k_i registered over the i -th interval $[t_{i-1}, t_i]$ with the number of counts $r(t_i)$ predicted by the response model given in Eq. (5.16). The instantaneous input $s(t_i)$ is split into two components such that

$$s(t_i) = b + \begin{cases} s_{n,i} & \text{if } t_i \text{ in the } n\text{-th open-bin} \\ 0 & \text{if } t_i \text{ in closed-bins} \end{cases}. \quad (5.36)$$

b represents a constant baseline from internal contributions. Since b is present at all times, the response of the PMT would simply shift-up the baseline, according to Eq. (5.18). We absorb such a shift into our notation and thus just add b to the response $r(t_i)$. On other hand, the external inputs $s_{n,i}$ are taken as constant over all intervals of the n -th open-bin, i.e. $s_{n,1} = s_{n,2} = \dots \equiv s_n$, whereas it is always 0 on the closed ones. Let us rewrite in a more compact form, $\mathbf{s} = (s_1, s_2, \dots, s_k)$. Hence for instance, if there are two cycles of *open/closed* measurements, the fitting parameters are $\mathbf{s} = (s_1, s_2)$, b , α and τ . The last three characterize the PMT.

The predicted number of counts is then given by

$$r(t_i, \mathbf{s}, b, \alpha, \tau) = b + s_{n,i} + \alpha(1 - e^{-\Delta t/\tau}) \sum_{j=0}^{j=i-1} s_{n,j} e^{-(t_i - t_{j+1})/\tau}, \quad (5.37)$$

where we used Eq. (5.22) for the integral response. Let us notice that the summation is actually only carried on the open-bins, where the periodic inputs do not vanish. For clarity, the notation $s_{n,i}$ really means that we have to associate the i -th interval $[t_{i-1}, t_i]$ with the n -th open-bin it belongs to. Then, the fitting procedure is achieved by minimizing the residual

$$y^2 = \sum_i \left(\frac{r_i - k_i}{\sigma_i} \right)^2. \quad (5.38)$$

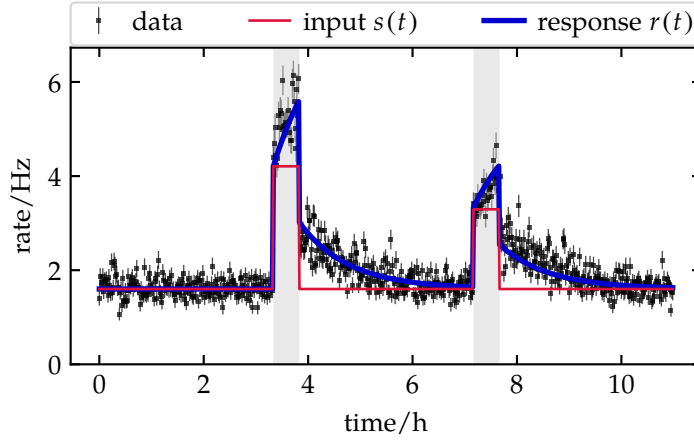


Figure 5.16: Example of measured rates (black markers) fitted with the detector response $r(t)$, according to Eq. (5.37), as result of an input illumination $s(t)$.

The errors σ_i 's are taken as the observed errors on the counts k_i 's assuming Poisson statistics. Inconveniently, we may in this way underestimate the parameter errors because of the overdispersion of counts discussed in Section 5.3.1. Alternatively, we can assume a constant variance. Nevertheless, we find that the difference is marginal for the parameter values.

An example of such a fit is shown in Fig. 5.16. The parameters of the PMT are determined by fitting several repeating measurements. We obtain

$$\begin{aligned}\alpha &= 0.922 \pm 0.015, \\ \tau/\text{min} &= 54.124 \pm 1.115, \\ b/\text{min} &= 96.600 \pm 0.394.\end{aligned}\tag{5.39}$$

Of more importance are α and τ . We argue that in our model, they are independent of the intensity or duration of the exposure since Eq. (5.16) is linear with respect to the input signal $s(t)$. The last parameter b is nothing but the internal background of the PMT (see Fig. 5.1).

5.4.4 Event reconstruction

The next step is to disentangle the memory effect from our standard measurement, and reconstruct the instantaneous component of the measured rate. In fact, we have already written the integral response of the PMT to past illumination in a convenient form, see Eqs. (5.20) to (5.23). Let us suppose that the run begins at $t_0 = 0$. The measured rate $r(t_m)$ at some given time $t_m \in [t_i, t_{i+1})$ can be expressed as

$$r(t_m) = b + \alpha s_{\text{neg}} e^{-t_m/\tau} + \alpha h_i + s_i [1 + \alpha(1 - e^{-(t_m-t_i)/\tau})].\tag{5.40}$$

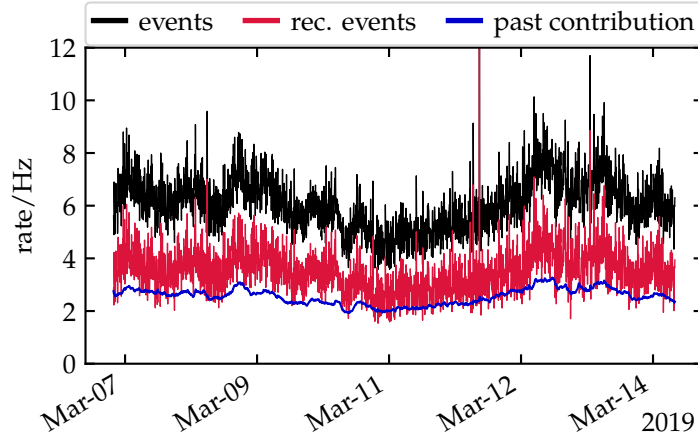


Figure 5.17: Example of signal reconstruction, showing one-week of events taken from the measurement *out/open* and without averaging. Here, past reconstruction means the residual rate after subtracting the reconstructed events.

Here, b is a constant count baseline, common to all four measuring modalities. s_{neg} represents the unknown illumination for negative times. h_i , given in Eq. (5.22), is the decay rate from the past i complete intervals elapsed since t_0 . The last terms sums the average instantaneous rate $s_i = s(t_i)$ over the current measuring interval $[t_i, t_{i+1})$, and its historical contribution up to the measurement time t_m .

It is now easy to invert Eq. (5.40) and recover the input signal. Furthermore, since the decay time τ of our PMT is one order of magnitude longer compared to the sampling duration Δt , we can evaluate the average rate as in the middle of the measuring interval such that $t_m = \bar{t}_i = t_i + \Delta t/2$. The last ingredient that we need is an algorithmic way to compute h_i . Let us consider the next $i + 1$ iteration, i.e. at $t_m = \bar{t}_{i+1} = \bar{t}_i + \Delta t$. We have

$$\begin{aligned} h_{i+1} &= e^{-\bar{t}_{i+1}/\tau} \sum_{j=0}^{j=i-1} s_j (e^{t_{j+1}/\tau} - e^{t_j/\tau}) + s_i e^{-\bar{t}_{i+1}/\tau} (e^{t_{i+1}/\tau} - e^{t_i/\tau}) \\ &= h_i e^{-\Delta t/\tau} + s_i e^{-\Delta t/2\tau} (1 - e^{-\Delta t/\tau}). \end{aligned} \quad (5.41)$$

Summarizing, the reconstruction algorithm is proceeded iteratively as follows,

$$s_i = \frac{r_i - b - \alpha (s_{\text{neg}} e^{-\bar{t}_i/\tau} + h_i)}{1 + \alpha(1 - f^{1/2})}, \quad i \geq 0, \quad (5.42)$$

with $f = e^{-\Delta t/\tau}$ and

$$h_0 = 0, \quad (5.43)$$

$$h_i = h_{i-1}f + s_{i-1}f^{1/2}(1 - f), \quad i \geq 1. \quad (5.44)$$

The values of α and τ are given in Eq. (5.39). The best estimate for the unknown state s_{neg} can be obtained by fitting first few hours of the response data of the PMT to Eq. (5.40), in a similar procedure as before. Nonetheless, looking at Eq. (5.42), we can avoid any bias related to the exact value of s_{neg} by simply discarding the first few hours of the reconstructed data. Thereafter, the event reconstruction is close to exact. Moreover, the baseline subtraction is not necessarily relevant since it also cancels-out in any signal differences between the four measuring modalities. Thus, we set $b = 0$ in such manner that it is included in the reconstructed signal. Lastly, let us remark that we did not account for the few seconds of discontinuities introduced between changes of the measurement configurations. Such an effect should be negligible since the decay rate of the PMT is slow and thus the data-taking can be approximated as continuous. An example of signal reconstruction is presented in Fig. 5.17.

5.4.5 Temperature correlation

In the beginning of Section 5.4.1, we stated that the memory effect is connected, to some degree, to the level of excitation of the photocathode and glass envelope of the PMT. A priori, direct irradiation by a strong light-source could leave the PMT in a certain excited state which can cause cascades of secondary emissions extended over long periods. In view of our relatively low and limited exposure rate, what actually triggers the mechanism, in the present case, is not completely understood. For instance, it could be indication of some late-correlated effect due to scintillation of the glass materialⁿ induced by external factors such as radioactive decays or particle showers.

In order not to largely speculate, we investigate possible correlation of the observed memory effect with other measured quantities. Of particular interest is the temperature. This is motivated from the former evaluation of the Pearson correlation coefficients between different pairs of observables, presented in Fig. 5.10. In Fig. 5.18, we plotted the rate of historical events^o denoted here $\tilde{r}(t)$, together with the monitored temperature T_2 of the experimental area. Both quantities are taken from averaging over one-full measurement cycle (see Fig. 5.4). The overlay suggests a non-negligible correlation between the two quantities, over time, although the main peaks of the two curves appear to be best aligned only at partial times. We evaluate the corresponding Pearson correlation to $\kappa(\tilde{r}, T_2) = 0.58$. Evidently,

ⁿ In Section 5.3.2, we mentioned that scintillation could also be responsible for short-time correlated events.

^o That is the residual rate after subtraction of the reconstructed event rate.

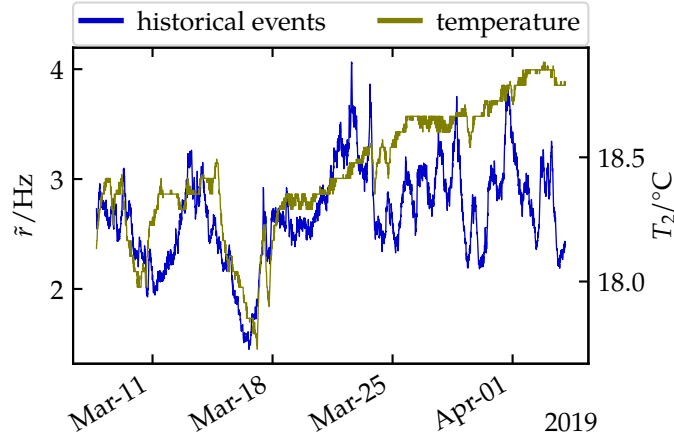


Figure 5.18: Rate of historical events $\tilde{r}(t)$ overlaid with the temperature T_2 of the experimental area, both averaged over one measuring cycle.

the correlation coefficient with temperature T_1 of the PMT housing is very similar.

For definiteness, we compute the normalized cross-correlation function $\kappa_{\tilde{r}, T_2}(t_{\text{lag}})$ between the historical rate $\tilde{r}(t)$ and the temperature T_2 per completed cycle, as function of some time lag t_{lag} . This is intended to identify eventual lagged-correlation between these two quantities. The cross-correlation is defined as follows,

$$\kappa_{\tilde{r}, T_2}(t_{\text{lag}}) = \frac{1}{(N-1)\sigma_{\tilde{r}}\sigma_{T_2}} \sum_j [\tilde{r}(t_j) - \langle \tilde{r} \rangle] [T_2(t_j + t_{\text{lag}}) - \langle T_2 \rangle]. \quad (5.45)$$

Here, N is the number of measurement cycles. $\sigma_{\tilde{r}}$ and σ_{T_2} denote the sample standard deviations of each respective variable. The index j runs over all cycles with a sampling time such that $t_{j+1} - t_j = \Delta t_{\text{cycle}}$, where $\Delta t_{\text{cycle}} \approx 4.4$ min is the duration of one cycle. This also represents a natural unit-step for t_{lag} . The normalization of the cross-correlation is chosen so as when $t_{\text{lag}} = 0$, Eq. (5.45) coincide with the Pearson correlation coefficient given in Eq. (5.6)^p. With a non-zero value of t_{lag} , the coefficient κ evaluates the overlap between the rate and the temperature data, after shifting the later linearly in time by t_{lag} (past or future). The overlap is maximum or minimum when \tilde{r} and the time-lagged T_2 are maximally correlated or anti-correlated.

The result from this cross-correlation analysis is shown in Fig. 5.19, where we progressively applied a time lag to the temperature data, in step of Δt_{cycle} and up to roughly 30 h in the past and future of the zero-lag reference. Let us make a few comments on this plot. First, we observe that the time shift has no significant effect on the correlation strength for t_{lag} less than a few hours. The best cross-correlation values are indeed obtained within such a time

^p This is not the case for non-zero t_{lag} , since the number of overlapping data points is less than N . In addition, the summation in Eq. (5.45) is extrapolated to 0 on non-overlapping points.

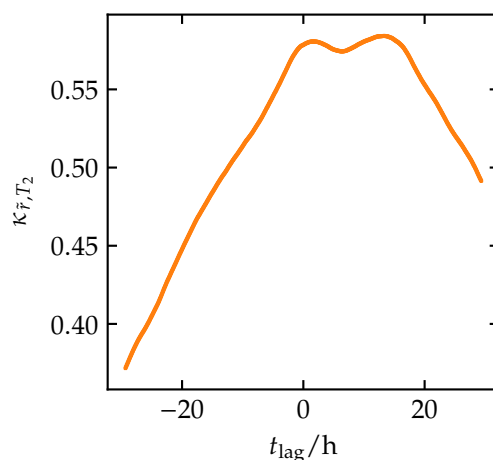


Figure 5.19: Normalized cross-correlation function of the historical rate $\tilde{r}(t)$ with the room temperature T_2 , as computed from Eq. (5.45).

scale. In fact, this is desirable. For longer negative t_{lag} , the cross-correlation function slowly decreases, disfavoring very delayed correlations between the two observables. On the contrary, the correlation of the historical rate seems to slightly improve with temperature data in the future. However, this is likely a bias due to noise in the data and boundary effects from the increasing number of non-overlapping samples, when evaluating Eq. (5.45). Therefore, it has no physical meaning.

From these observations, it is believed that the ambient temperature, also possibly the temperature of the physical body of the PMT, has some influence on the main mechanism which triggers this memory effect during the FUNK measurement. An unambiguous physical explanation still needs to be confirmed.

5.5 Fourier analysis

5.5.1 Spectral decomposition

We perform a spectral Fourier decomposition of the reconstructed rate $r(t)$, in order to investigate possible time modulation. For this purpose, we consider a sequence of measurements taken from fixed configuration, e.g. $r_{\text{out open}} = \{r_0, r_1, \dots, r_N\}$, where $r_i = r(t_i)$ and N is the number of measuring cycles in the reconstructed dataset. Thus the sampling frequency is $F_s = 1/\Delta t_{\text{cycle}} \approx 0.225 \text{ min}^{-1}$.

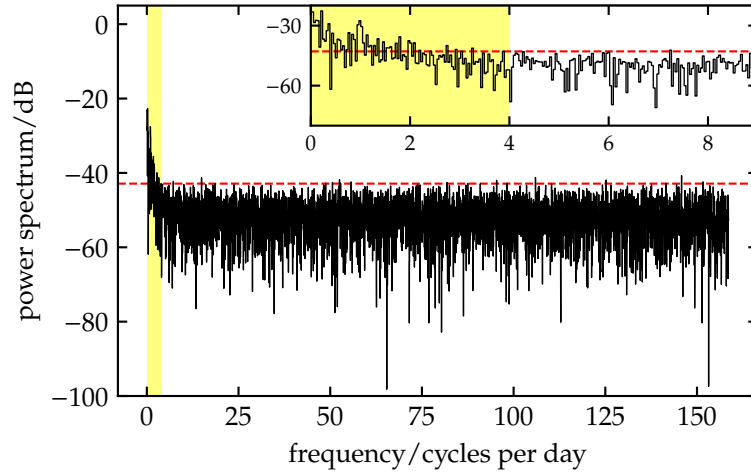


Figure 5.20: Power spectrum of the reconstructed rate calculated according to Eq. (5.46) and using the *out/open* dataset. The inset is a zoom on the yellow-shaded area which is used for the detrending procedure explained in Section 5.5.2. The red dashed line indicates a significance threshold of the frequency powers.

Next, we compute the normalized power spectrum P_k associated to a frequency mode $f_k = F_s(k/N)$, defined as

$$P_k = 10 \lg \left| \frac{A_k}{A_0} \right|^2, \quad (5.46)$$

where A_k is the complex coefficient obtained from a discrete Fourier decomposition of the rate given by

$$A_k = \sum_{n=0}^{N-1} e^{-2\pi jk(n/N)} r_n. \quad (5.47)$$

As an example, we apply such an analysis to the dataset *out/open*. The result is presented in Fig. 5.20 where we showed an one-sided^q decomposition. Frequencies are plotted from the first harmonic up to the Nyquist limit $f_{\text{Nyq}} = F_s/2$. The frequency resolution is set by the maximum possible periodicity in the sample, i.e. F_s/N .

As an immediate observation, the rate exhibits a relatively large stationary component, with $P_k \lesssim -30$ dB for all harmonics. This implies that the amplitudes $|A_k|$ of the Fourier modulations are suppressed by at least one order of magnitude compared to DC component $|A_0|$. Besides, we find that the modulations are more substantial at lower frequencies (few cycles per day). The dashed red line in Fig. 5.20 represents an arbitrary level of

^q For the two-sided spectrum of a real signal, the power is equally distributed between negative and positive frequencies, except for the DC and Nyquist components.

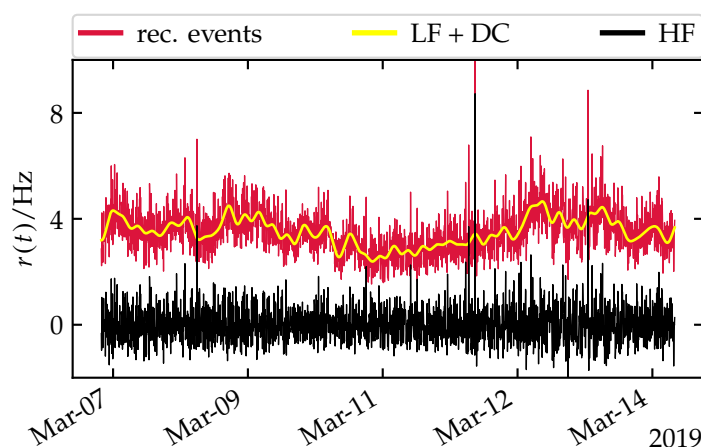


Figure 5.21: Detrending of the reconstructed rate, illustrated with the *out/open* data (see text for explanation). The rate can be decomposed such that $r(t) = \text{DC} + \text{LF}(t) + \text{HF}(t)$, with $\text{DC} = \langle r \rangle$. Only for plotting purpose, the LF harmonics have been shifted-up by DC.

significance, set to 2 standard deviations from the mean of a truncated distribution of the power spectrum. Since these low-frequency harmonics are also observed across all measurement configurations, in particular with the “closed” modes, we conclude that they essentially stem from background processes.

5.5.2 Low-frequency detrending

Modulations of the rate on long time scales are presumably related to modulations in cosmic-ray flux, which in turns are, for instance, connected to variations in atmospheric pressures, as explained in Section 5.2.4. Moreover, for our aimed level of sensitivity, that is $\sim 10^{-3}$ Hz or 1 detectable HP-to-photon conversion every ~ 15 min, we do not expect any substantial modulation of the HP signal.

Therefore in our analysis, we detrend the reconstructed rate by removing low-frequency (LF) oscillations up to a certain threshold. This frequency threshold is chosen such that it does not affect the distribution of the residual high-frequency (HF) rate, after applying the inverse Fourier transform. Such a procedure is illustrated in Fig. 5.21, where we removed components of the Fourier spectrum with frequencies less than 4 cycles per day, which were marked by the yellow-shaded area in Fig. 5.20.

5.6 Systematical uncertainties

Systematical uncertainties arise because the conditions in which the measurements were performed might slightly differ between four measuring modalities. These include uncertainties on the DAQ up-time, variations of the environmental conditions, differing imaging conditions due to potential reflections when the camera is the center of curvature of the mirror. In the following, we examine each of these contributions.

5.6.1 DAQ timing

In Section 3.2.3, we mentioned that the one minute up-time of the DAQ, for each configuration, is typically monitored to 1 ms accuracy. This was achieved by implementing two timers in the software, before and after the begin and stop commands of the DAQ, in such a manner that the true timing of the measurement can be estimated from the average of both timers, whereas the uncertainty is estimated from their difference [77]. For run v35, we obtain an average up-time of

$$\Delta t/s = 60.00138 \pm 0.00237. \quad (5.48)$$

Let us denote by t_{tot} the total duration of one measuring mode. This means, the entire run has an effective duration of $4 \times t_{\text{tot}}$. We write $t_{\text{tot}} = \sum_{i=1}^N \Delta t_i = N \Delta t$, where N is the number of measuring intervals for each configuration. A systematical shift on the order of the timing uncertainty $\sigma_{\Delta t}$ quoted in Eq. (5.48), for each sequence of measurement, would result in a systematical bias^r such that $\sigma_{t_{\text{tot}}}^2 = (\sigma_{\Delta t_1} + \dots + \sigma_{\Delta t_N})^2 = (N \sigma_{\Delta t})^2$. This corresponds to a relative uncertainty of $\sigma_{t_{\text{tot}}}/t_{\text{tot}} = 0.004\%$. Ignoring for a moment other systematical effects, the total uncertainty on the measured rate r is given by

^r Correlated errors add linearly.

$$\sigma_r^2 = \sigma_{\text{stat}}^2 + r^2 \left(\frac{\sigma_{t_{\text{tot}}}}{t_{\text{tot}}} \right)^2, \quad (5.49)$$

^s The observed statistical uncertainty is between a factor of 3 to 4 larger, due to the featured overdispersion addressed in Section 5.3.1.

where $\sigma_{\text{stat}} = \sqrt{r/t_{\text{tot}}}$ for Poissonian statistics^s. Let us plug in some numbers. Considering a month-worth of data taking ($N = 10000$) with a typical rate of $r = 4$ Hz, we find $\sigma_{\text{stat}} = 0.02$ Hz. The latter is more two orders of magnitude larger than the corresponding timing uncertainty.

5.6.2 Environmental conditions

Temperature drift between two measurement configurations

In Section 3.2.5, we demonstrate that the FUNK experiment operates in environmental conditions which provides excellent temperature stability.

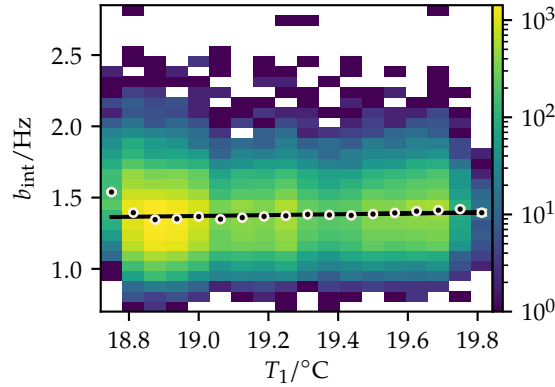


Figure 5.22: 2D density scatter-plot of the internal background-event b_{int} of the PMT and the temperature T_1 of its housing. The white markers indicate the average rate per temperature bin and the black line is linear fit.

This is ensured by continuous monitoring before, during, and after each complete run. Systematical uncertainty can arise from fluctuations occurring between changes of the measuring mode. For run v35, the typical variation of the temperature-difference measured between the “in” and “out” positions is evaluated to $0.02\text{ }^\circ\text{C}$.

In Fig. 4.1, we estimated a temperature coefficient of $\sim 0.07\text{ Hz }^\circ\text{C}^{-1}$ for the FUNK PMT, on the basis of some general properties of its bialkali photocathode. For definiteness, we measure this coefficient from the internal background-event b_{int} of the PMT, under the sealed-FACT50 condition (see Section 4.1). Given the expected linear behavior of the dark current with room temperature, we fit the joint distribution of b_{int} and the monitored temperature T_1 of the PMT housing accordingly. The result is presented in Fig. 5.22. A linear fit yields a slope of

$$m_T/(\text{Hz }^\circ\text{C}^{-1}) = 0.030 \pm 0.014, \quad (5.50)$$

which is compatible with our first estimate. Over the whole run, this temperature dependence induces a systematical uncertainty of $6 \times 10^{-4}\text{ Hz}$ in count rate or roughly 3% of the difference *in* – *out* in rate.

Pressure dependence of the Cherenkov rate

Likewise, we provided in Table 4.2 an estimation of the amount of Cherenkov photons, produced by CR muons passing in the air surrounding the setup, and falling within the spectral sensitivity of the PMT. This corresponds to roughly 300 kHz photons roaming around. By comparison, the typical rate measured with the open shutter is 5 Hz, which represents 0.002% of the ambient Cherenkov rate.

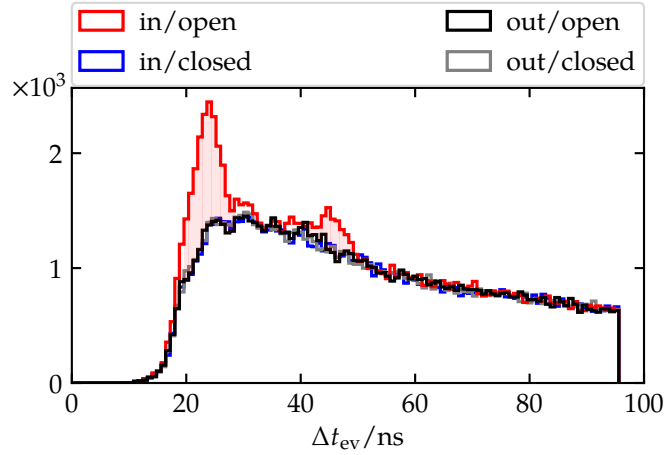


Figure 5.23: Distribution of timings Δt_{ev} between consecutive events and for all four measurement configurations. The shaded regions indicate the event excess due to reflections from the mirror (see text for explanation).

On consideration of the variation of the atmospheric refractive index, and thus the Cherenkov rate, with the atmospheric pressure, we quoted a pressure gradient of 0.5 kHz hPa^{-1} in Eq. (4.28). On the other hand, the monitoring of the pressure difference between the “in” and “out” measurements, yields a standard deviation of about 6 Pa. This corresponds to a variation of 30 Hz or 0.01 % in the Cherenkov rate. Clearly, such a variation is too small to induce a meaningful systematical effect on the detected rate.

5.6.3 Mirror reflections

When the PMT is positioned at the center of curvature of the mirror with the shutter open, some photons (e.g. from muon hits) could be refracted towards the mirror and then get reflected back to the PMT. Later, we identify these reflections as our largest source of systematical uncertainties. In order to evaluate the magnitude of this effect, we study the timing differences Δt_{ev} between consecutive events captured in the same trace window. We already plotted the overall distribution in Fig. 5.9(b), for values of Δt_{ev} up to half of the trace length ($\sim 800 \text{ ns}$).

Here, we analyze the time scale which matches the duration that a single photon needs to cover the radial distance to the mirror and back. That is $2 \times 3.4 \text{ m}/c \approx 22 \text{ ns}$. This zoomed-in distribution^t of Δt_{ev} is shown in Fig. 5.23 for all four measuring modalities. The two clear excesses of events, with peaks at the 24 ns and 44.8 ns bins and only observed with *in/open* configuration, conform to the hypothesis of single and double reflections of photons, respectively.

^t The bin resolution is set to 0.8 ns which equals the DAQ sampling period.

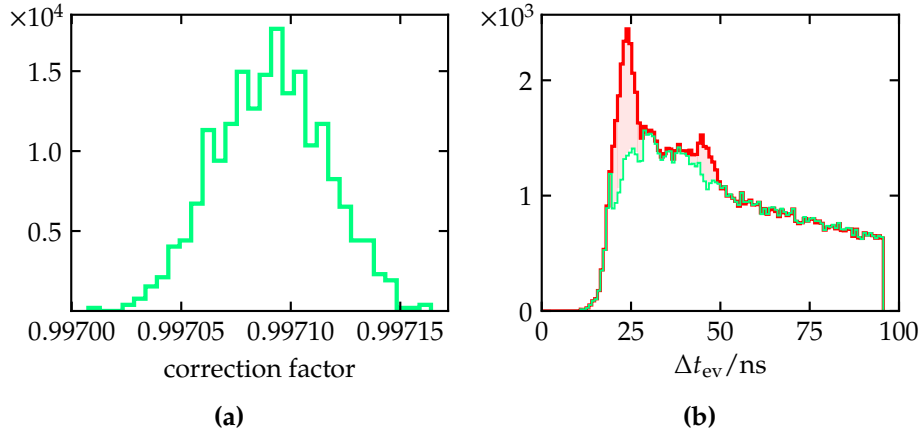


Figure 5.24: (a) Distribution of the correction factor to be applied to the *in/open* dataset. (b) Same as Fig. 5.23 but showing the distribution of Δt_{ev} for the *in/open* configuration only. The green line is the realization of one Monte-Carlo which produces a reflection-corrected dataset.

Monte-Carlo simulation

We estimate the overall size of the mirror reflections with a Monte-Carlo simulation. This can be achieved by randomly selecting events which successively occur on a time scale of the reflection with a probability p_i given by

$$p_i = \begin{cases} \frac{k_i^{\text{out/open}}}{k_i^{\text{in/open}}} & \text{for the } i\text{-th reflection bins} \\ 1 & \text{otherwise} \end{cases}, \quad (5.51)$$

where the reflection bins are defined as spanning ± 5.5 bin widths around the main observed excess-peaks. Those correspond to the red shaded regions in Fig. 5.23. $k_i^{\text{out/open}}$ and $k_i^{\text{in/open}}$ are the bin counts for both respective configurations. Thus p_i defines the probability that the next detected-event is *not* from reflection.

We repeated this procedure sufficient times to estimate the correction factor that should be applied to the *in/open* dataset, in order to account for the reflected events. The distribution of the correction factor is plotted in Fig. 5.24(a), where we obtain a mean of 99.7% with a standard deviation of 0.002%. The outcome of such a Monte-Carlo correction is illustrated in Fig. 5.24(b).

Correction method

The difficulty of this task lies in the fact that the estimated 0.3% relative excess in the *in/open* configuration, is not solely due to reflection. It does also

contain some historical background as has been discussed Section 5.4, as well as possible HPs. To facilitate our understanding of the problem, let us ignore for a moment any contribution from HP signal. In the model of the memory effect proposed in Eq. (5.16), the integral response of the memory kernel of the PMT scales linearly with the instantaneous input signal. In other terms, the observed excess should not be readily removed before we apply the reconstruction algorithm in Section 5.4.4. If we measure some background excess in the data, the correct approach is to first run the event reconstruction, and second remove the instantaneous component of that excess.

Let us focus on the rate measured with the shutter open, and as such, we suppress this label in the following notation. Furthermore, we only consider an average correction, i.e assuming constant rates on all four measuring modalities. Such a scenario was studied in the last example of Section 5.4.2. Let us write the instantaneous event rates as $s_{\text{in}} + s_{\text{refl}}$ at the position “in”, and s_{out} at the position “out”. Here, s_{refl} denotes the contribution from reflected photons. Inserting these terms into Eq. (5.34) and with the index replacements “0 \rightarrow out” and “2 \rightarrow in”, we find that the response rates of the PMT can be expressed such that,

$$\begin{aligned} r_{\text{out}} &= \frac{\alpha}{4} s_{\text{refl}} + r'_{\text{out}}, \\ r_{\text{in}} &= \left(1 + \frac{\alpha}{4}\right) s_{\text{refl}} + r'_{\text{in}}, \end{aligned} \quad (5.52)$$

where the primed rates correspond to the expected measurements if there were no reflections. Taking the difference, it follows

$$(r_{\text{in}} - r_{\text{out}}) - (r'_{\text{in}} - r'_{\text{out}}) = s_{\text{refl}}. \quad (5.53)$$

What we actually measure as an excess is given by the first term $r_{\text{in}} - r_{\text{out}}$. In absence of HP signal and assuming an uniform background at the two measuring positions, the difference $r'_{\text{in}} - r'_{\text{out}}$ cancels out in Eq. (5.53). Therefore, the measured 0.3 % relative excess is indeed an overly conservative estimate of the actual correction s_{refl} . Its overall size is on the same order of magnitude as our statistical uncertainty.

Ultimately, it is nice to have such a correction. However, it is obvious that the above choice of method is totally insensitive to an eventual HP signal. As it is deemed necessary not to weaken the strength of a potential signal, we choose not to apply any correction on the mirror reflections.

5.7 Improved exclusion limit

At this stage, it is appropriate to summarize the different steps of the data taking and event selection:

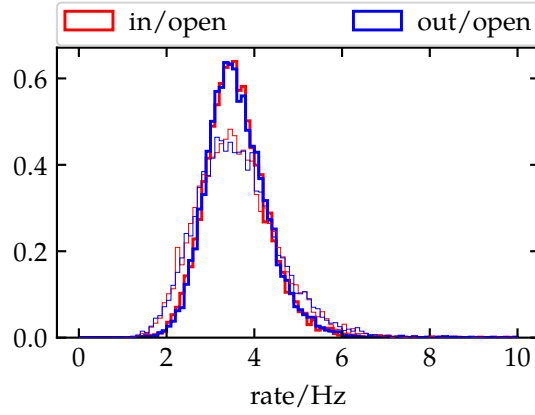


Figure 5.25: Distribution of the reconstructed rates *in* and *out* of the radius point with the shutter open. The light and thicker lines correspond to the dataset before and after the detrending, respectively.

- (i) the data are captured in self-triggered mode, then individual pulses are identified off-line, analyzed and selected according to the SPE-like filters based on their time distributional widths and information entropies (Sections 3.2.4 and 5.2.3),
- (ii) the event counts during the 60 s intervals are reconstructed in order to correct for the PMT memory effect and the first 50 measuring cycles (~ 3.5 h) are discarded to avoid potential bias (Section 5.4.4),
- (iii) the reconstructed rate is detrended in frequency domain by removing their Fourier components with frequencies less than a 4 cycles/day (Section 5.5.2).

The resulting rates after these procedures are shown in Fig. 5.25. For the difference of single-photon counts “in” and “out” of the center of curvature with the shutter *open*, we find

$$\Delta r_{\text{open}}/\text{Hz} = (r_{\text{in/open}} - r_{\text{out/open}})/\text{Hz} = -0.0229 \pm 0.0108. \quad (5.54)$$

Nonetheless, it is worth to mention that this negative rate is compatible with the difference observed in the background-only measurement with the shutter *closed* (and without detrending),

$$\Delta r_{\text{closed}}/\text{Hz} = (r_{\text{in/closed}} - r_{\text{out/closed}})/\text{Hz} = -0.0267 \pm 0.0109. \quad (5.55)$$

The relevant sensitivity equation, which relates to strength of the mixing parameter, is given in Eq. (3.3). It is assumed that HPs make up the whole Cold DM and we take the standard energy density of local DM. Furthermore,

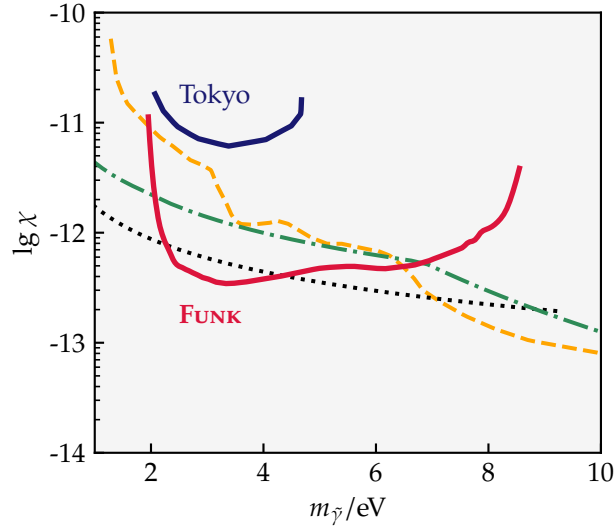


Figure 5.26: A 95 % C.L. upper limit on the magnitude of the kinetic mixing χ . The region shown is within the allowed parameter space for HPs to be cold DM. The limit labeled Tokyo [22] is from another dish antenna experiment, using a smaller mirror. The dashed orange line is a constraint from DAMIC [58], searching for HP ionization signal in the detector targets. The dot-dashed green corresponds to astrophysical bound from the solar lifetime and the dotted black line is a limit from Xenon10 [59] for solar HPs.

we suppose that the HPs have no preferred polarization. The potential HP signal is resolved from the difference Δr_{open} . To deal with the negative signal, we apply the Feldman and Cousins construction for Gaussian signal with a boundary at origin [127]. This method gives the correct coverage for a certain C.L. upper limit, when we measure an unphysical negative value of the signal estimate. Our final result is presented in Fig. 5.26. We obtain an upper bound on the magnitude mixing parameter such that $\chi \lesssim 3.44 \times 10^{-13}$ at a 95 % C.L. for HPDM with masses $1.95 \leq m_{\tilde{\gamma}}/\text{eV} \leq 8.55$.

6

Summary and conclusions

In this work, we presented the outcome of three years of quest for Hidden-Photon Dark Matter (HPDM) in the eV mass range at the FUNK experiment.

After a general overview on HP physics, we reviewed the basis of the direct-detection principle operating at the FUNK experiment, which exploits the natural kinetic mixing between HP and ordinary photons. The idea was to use a $\sim 14 \text{ m}^2$ spherical metallic mirror to generate, in the presence of an homogeneous HPDM field, a tiny flux of real detectable photons that can be measured at the center of curvature of the mirror. The energy of these photons is directly given by the mass of the HPs and their intensity relates to the magnitude of the mixing parameter and the energy density of local Dark Matter (DM). In particular, the consequent sensitivity equation has been improved by properly accounting for the non-ideal reflectivity of the mirror.

Our experiment was setup to scan for HP signal in the visible and near-UV spectrum by using a dedicated low-noise Photomultiplier Tube (PMT), aiming at counting single-photon events at the rate of few photons/s and with a potentially resolvable signal of 10^{-2} Hz to 10^{-3} Hz . This level of sensitivity can only be achieved with an effective background reduction and an excellent environmental stability, which were guaranteed. To this end, we also carried-out a detailed estimation of the known limiting background. To identify the single-photon events reliably, we developed a new method of event selection, which analyzes individual pulse signals at output of the PMT based on their time width and information entropy. This provided us with a model-independent event-by-event discrimination, solely based on the calibration data.

A large part of this work was devoted to a detailed analysis of the completed measurements, with an emphasis to our latest data-acquisition runs. The most important aspects are the following. First, we determined that a large fraction of the background processes in play exhibited a relatively strong non-Poissonian nature, including an overdispersion in counts and a correlation in time. This is of great importance when considering a statistical

limit. Next, we identified a peculiar memory effect distinctive to low-noise PMTs in the form of an historical background contributing to the measured photon rate. It is suspected that such an effect is often neglected or unreported by many low-background experiments. We were able to successfully model this feature and establish a new algorithm for event reconstruction. Furthermore, we discovered an important systematical effect which was attributed to reflections from the mirror, when the detector is positioned at of the expected signal. We estimated that the size of these reflections is of the same order of magnitude as the statistical uncertainties. However, we did not correct for this effect as it could remove at the same time a potential HP signal.

In the final result, no HP signal was found and we set a 95 % C.L. upper bound on $\chi \lesssim 10^{-13}$ for HPs with masses between 2 eV and 8 eV. This limit is compatible with the existing constraints from other direct-detection experiments in the same mass range and from the model-dependent astrophysical bounds, in particular the lifetime of the sun. The main achievement is summarized in Fig. 6.1.

We also briefly examined the prospective future of the FUNK experiment, in targeting HPDM in the (sub)-meV mass range. With a simple proof of concept, we argued that it is conceivable to probe values of the kinetic mixing in this region down to $\chi \sim 10^{-13}$, where no other experiments are competitive.

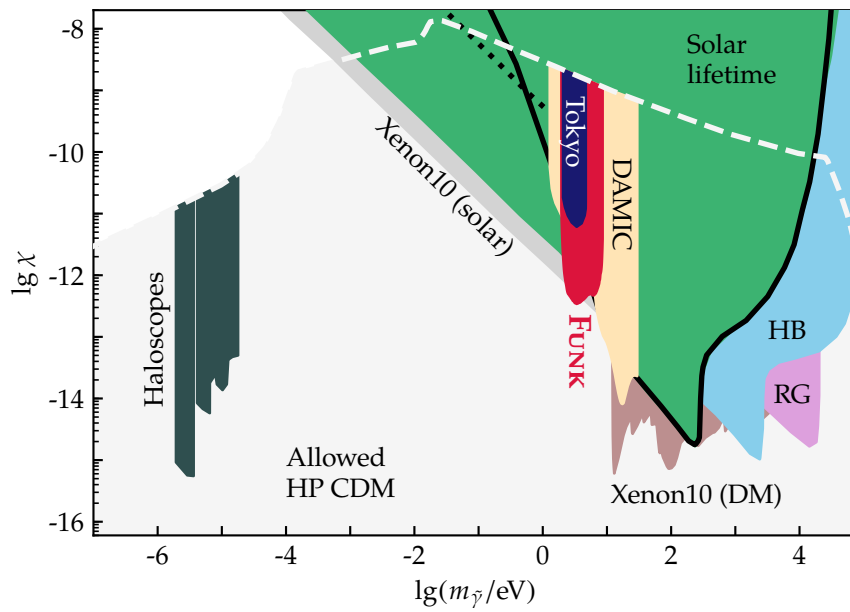


Figure 6.1: FUNK exclusion limit at a 95% C.L. (red-shaded region). The Tokyo limit was obtained by a similar setup but with a smaller mirror [22]. HP bounds from other direct-detection experiments are also shown in comparison: DM haloscopes [19], DAMIC [58], and Xenon10 [59] (both as DM and as dark radiation emitted by the sun). The regions labeled Solar lifetime, HB (horizontal-branch stars) and RB (red giants) are indirect constraints derived from astrophysical considerations [28]. The physics related to these various limits are further explained in Sections 2.1.2 and 2.3.3. Finally, the grey-shaded region corresponds to the allowed parameter-space for HP to act as CDM [18, 19].

A

Flux of particles entering a box

The dependence on zenith and azimuth angles (ϑ, φ) of the muon intensity $\mathcal{I} = dN/dA d\Omega dt$ is described by Eq. (4.16). To estimate the total flux of muons entering the confining area of the FUNK setup, we need to calculate the fluxes of particles crossing both horizontal and vertical surfaces. Additionally, we shall only consider muons going in downward directions.

A.1 Downward muons crossing a horizontal surface

For horizontal surfaces, we simply integrate the intensity over the projected solid angle. If each surface element dA equally sees the entire upper-hemisphere (hereafter denoted by \cap), i.e $d\Omega$ is independent of the patch coordinates, then the horizontal flux J_H is given by

$$\begin{aligned} J_H &= \int_{\cap} d\Omega \cos \vartheta \mathcal{I}(\vartheta, \varphi) \\ &= \mathcal{I}_v \int_0^{\pi/2} d\vartheta \sin \vartheta \cos^3 \vartheta \int_0^{2\pi} d\varphi \\ &= \frac{\pi}{2} \mathcal{I}_v \text{ [cm}^{-2} \text{ s}^{-1}\text{]}. \end{aligned} \tag{A.1}$$

A.2 Downward muons crossing one side of a vertical surface

First, it should be noted that Eq. (4.16) implies horizontal detectors. For vertical surfaces, it is convenient to rotate the coordinate axes in such a way that the normal to the surface is along the “z-axis”. Particles traversing a vertical surface element dA_V must have equally traversed a horizontal surface element dA_H , as illustrated in Fig. A.1. In the primed coordinates,

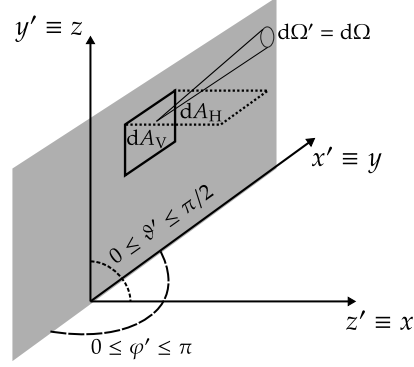


Figure A.1: Coordinate transformation for vertical surfaces. The meaning of the various labels are given in the text.

let us define $\tan \alpha' \equiv dy'/dz' = \sin \vartheta' \sin \varphi' / \cos \vartheta'$. Then, the following relation holds

$$dA_V = dx' dy' = \tan \alpha' dx' dz' = \tan \alpha' dA_H. \quad (\text{A.2})$$

It is now easy derive the flux of particles J_V crossing a vertical surface from one side (i.e half of the upper-hemisphere $\cap_{1/2}$ corresponding to $z \geq 0$),

$$\begin{aligned} J_V &= \int_{\cap_{1/2}} d\Omega' \cos \vartheta' \left(\frac{I_v \sin^2 \vartheta' \sin^2 \varphi'}{\tan \alpha'} \right) \\ &= I_v \int_0^{\pi/2} d\vartheta' \cos^2 \vartheta' \sin^2 \vartheta' \int_0^{\pi} d\varphi' \sin \varphi' \\ &= \frac{\pi}{8} I_v = \frac{J_H}{4} \quad [\text{cm}^{-2} \text{s}^{-1}]. \end{aligned} \quad (\text{A.3})$$

In case of a rectangular box, muons can enter the volume through all faces except from the bottom, i.e one horizontal surface (top) and 4 vertical surfaces (sides). With this construction, it is trivial to calculate the total rate of muons ϕ_Σ entering a box of dimensions $a \times b \times c$,

$$\begin{aligned} \phi_\Sigma &= ab J_H + 2(ac + ab) J_V \\ &= \left(ab + \frac{c}{2}(a + b) \right) J_H \equiv A_{\text{eff}} I_v, \end{aligned} \quad (\text{A.4})$$

where in a general way, A_{eff} contains all geometrical terms.

A.3 Average path-length

Let us consider a rectangular box of dimensions $a \times b \times c$ and let us subdivide it into thin horizontal lamina with surface $A_H = ab$ and thickness $\delta c \ll a, b, c$. In the same spirit as before, we suppose that there are no muons entering the box from below. A single muon with incident zenith-angle ϑ traverses a distance of $\delta l = \delta c / \cos \vartheta$ within one lamina. Then given a measured intensity $\mathcal{I}(\vartheta, \varphi)$, the total path-length δl_Σ of these muons within one lamina, per unit time, reads

$$\begin{aligned} \delta l_\Sigma &= \int_{\Omega} dA_H d\Omega \cos \vartheta (\mathcal{I}(\vartheta, \varphi) \delta l) \\ &= \langle \delta l \rangle A_H J_H, \end{aligned} \quad (\text{A.5})$$

where the average path-length $\langle \delta l \rangle$ is

$$\langle \delta l \rangle = \frac{\int_{\Omega} d\Omega \cos \vartheta (\mathcal{I}(\vartheta, \varphi) \delta l)}{\int_{\Omega} d\Omega \cos \vartheta \mathcal{I}(\vartheta, \varphi)} = \frac{4}{3} \delta c. \quad (\text{A.6})$$

The total path-length L_Σ of muons, per unit time, within the entire volume of the box is obtained by summing over all lamina as

$$L_\Sigma = \sum_{\text{lamina}} \delta l_\Sigma = \frac{4}{3} V_{\text{box}} J_H, \quad (\text{A.7})$$

with $V_{\text{box}} = A_H \sum_{\text{lamina}} \delta c = abc$ denoting the volume of the box. The average path-length $\langle L \rangle$ is given by

$$\langle L \rangle = \frac{L_\Sigma}{\phi_\Sigma} = \frac{4}{3} \frac{abc}{ab + (a+b)c/2}, \quad (\text{A.8})$$

where the total rate of muons ϕ_Σ is given by Eq. (A.4).

B

Miscellaneous

B.1 Average Signal power

Averaging

In the following, we give details on the different averaging which leads to to Eq. (2.51). First, for the time average we can use the following result

$$\overline{\left[\cos(m_{\tilde{\gamma}}t + a) \cos(m_{\tilde{\gamma}}t + b) \right]}_t = \frac{1}{2} \cos(a - b), \quad (\text{B.1})$$

for some phases a, b and with a period $2\pi/m_{\tilde{\gamma}}$. Let us now worry a bit about the average along the propagating direction. We only need to care about the case where the term inside the absolute value might change sign. For some $-1 \leq y \leq 1$ and $x_0 = \arccos(y)/a$, we have

$$\begin{aligned} \overline{|y - \cos(b - ax)|}_x &= \overline{|y - \cos(ax)|}_x \\ &= \frac{|a|}{2\pi} \left(- \int_0^{x_0} + \int_{x_0}^{\frac{2\pi}{|a|} - x_0} - \int_{\frac{2\pi}{|a|} - x_0}^{\frac{2\pi}{|a|}} \right) dx (y - \cos(ax)) \\ &= y \left(\frac{1}{2} - \frac{1}{\pi} \arccos y + \frac{1}{\pi} \arcsin y \right) + \frac{2}{\pi} \sqrt{1 - y^2} \\ &\approx y, \text{ when } y \rightarrow 1. \end{aligned} \quad (\text{B.2})$$

The last approximation is valid for our consideration where medium (1) is vacuum and medium (2) is a good reflector, i.e $y = n_1 = 1$, $a_1 = 0 = \delta_1$ and $1/|\eta| = |n_2 - 1|/|n_2| \approx 1$.

Turning now to the direction of the incoming Dark Matter (DM) field, we want to average over the angle^a α , defined in Eq. (2.45), between the \mathbf{E}_{DM} and the interface plane. Let \mathbf{v} be a unit vector along \mathbf{E}_{DM} . Its parallel component lies along the vector $\mathbf{v}_{\parallel} = -\mathbf{n} \times (\mathbf{n} \times \mathbf{v})$, where \mathbf{n} is a unit normal to the interface. In spherical coordinates, the angle α is given by

$$\cos \alpha = \frac{\mathbf{u} \cdot \mathbf{u}_{\parallel}}{|\mathbf{u}_{\parallel}|} = \pm \sqrt{1 - \sin^2 \vartheta \cos^2 \varphi}, \quad (\text{B.3})$$

^a Naturally, the average only makes sense when we assume random polarization.

where ϑ and φ are the zenith and azimuth coordinates of \mathbf{E}_{DM} , respectively. Assuming an isotropic distribution over a unit sphere, we obtain $\langle \cos^2 \alpha \rangle = 2/3$.

Reflectivity

We have now almost all ingredients to express the signal power in Eq. (2.50) in a convenient way. The last bit is to write the parameter $1/\eta$ in terms of the reflectivity of the interface. The reflectivity R defined for ordinary electromagnetic wave with normal incidence is given by

$$R = \left| \frac{n_2 \epsilon_1 - n_1 \epsilon_2}{n_2 \epsilon_1 + n_1 \epsilon_2} \right|^2. \quad (\text{B.4})$$

To simplify, we again focus on the case where $n_1 = 1$ and $1/\eta = 1 - 1/n_2$. In this case, Eq. (B.4) can be written as

$$\begin{aligned} R &= \left| \frac{1 - n_2}{1 + n_2} \right|^2 = \left| \frac{1/\eta}{2 - 1/\eta} \right|^2 \\ &= \frac{1/|\eta|}{4 - 4 \cos \phi / |\eta| + 1/|\eta|^2}, \end{aligned} \quad (\text{B.5})$$

where we recall that $\phi = \arg(\eta)$. For a good conductor, n_2 is *mostly* imaginary^b, the complex phase ϕ is small, so that $\cos \phi = 1 - \phi^2/2$. Eq. (B.5) is quadratic in $1/|\eta|$, whose positive root is

$$\frac{1}{|\eta|} = \frac{2(\sqrt{R} - R)}{1 - R} + \mathcal{O}(\phi^2). \quad (\text{B.6})$$

^b E.g. for Aluminum, $n_2 = 0.8 - 6i$ at wavelength 500 nm. This yields $\phi = 9^\circ$.

B.2 Width of the Signal

In this section, we estimate the linewidth of a HP signal in frequency domain, assuming a Maxwellian distribution of the DM velocity. The result is useful for spectroscopy analysis. From energy conservation, the emitted electromagnetic wave from a HP-to-photon conversion oscillate at frequency ν such that

$$2\pi\nu = \omega \simeq m_{\tilde{\nu}}(1 + v_{\text{DM}}^2/2), \quad (\text{B.7})$$

where v_{DM} is distributed according to

$$f(v_{\text{DM}}) = A v_{\text{DM}}^2 \exp(-v_{\text{DM}}^2/v_0^2). \quad (\text{B.8})$$

A is a normalization constant and $v_0 = 10^{-3}$ is the typical velocity of local DM. The mode of this distribution corresponds to $f(v_0) = A v_0^2/e$. Thus at half-maximum, we have

$$A v_0^2/2e = A v_{\text{DM}}^2 \exp(-v_{\text{DM}}^2/v_0^2). \quad (\text{B.9})$$

Defining $x = v_{\text{DM}}/v_0$, the above equation can be written as

$$\ln x^2 - x^2 + \ln 2e = 0. \quad (\text{B.10})$$

Let $y = \ln x^2$ and $c = -\ln 2e$. Then, from Eq. (B.10) it follows

$$\begin{aligned} e^y - y + c &= 0 \\ e^{e^y} e^{-y} e^c &= 1 \\ -e^c &= -e^y e^{-e^y}. \end{aligned} \quad (\text{B.11})$$

Introducing the Lambert function W , which is defined as the inverse of the function $g(W) = We^W$, Eq. (B.11) becomes

$$\begin{aligned} W(-e^c) &= W(-e^y e^{-e^y}) \\ &= -e^y \\ &= -y + c, \end{aligned} \quad (\text{B.12})$$

where the last step follows from Eq. (B.10). Let us note that for some real variable z , the function $W(z)$ is defined for $z \geq -1/e$. So the above equations are consistent. From Eq. (B.12), it follows

$$y = c - W(-e^c). \quad (\text{B.13})$$

The latter gives the two solutions of Eq. (B.9) such that

$$\begin{aligned} v_{\text{DM},1} &\equiv v_1 = v_0 e^{(c - W_0(-e^c))/2}, \\ v_{\text{DM},2} &\equiv v_2 = v_0 e^{(c - W_{-1}(-e^c))/2}, \end{aligned} \quad (\text{B.14})$$

where W_0 and W_{-1} are the upper and lower real branches of the Lambert function, respectively. Let us remark that by making the substitution $x \rightarrow \ln e$, we obtain $v_1 = v_2 = v_0$ which indeed corresponds to the mode of the Maxwell distribution. Hence, the full width of the velocity distribution at half-maximum is given by

$$\Delta v_{\text{DM}} = |v_2 - v_1| = 1.15v_0. \quad (\text{B.15})$$

Finally, from Eq. (B.7) we derive

$$\begin{aligned} \Delta v_{\text{FWHM}} &= v(v_2) - v(v_1) \\ &= \frac{m_{\tilde{\gamma}}}{2\pi} \frac{v_1 + v_2}{2} \Delta v_{\text{DM}} \\ &\simeq \frac{m_{\tilde{\gamma}}}{2\pi} v_0 \Delta v_{\text{DM}}. \end{aligned} \quad (\text{B.16})$$

Numerically, this gives

$$\Delta v_{\text{FWHM}} = 1.2 \text{ MHz} \left(\frac{v}{\text{THz}} \right) = 280 \text{ Hz} \left(\frac{m_{\tilde{\gamma}}}{\mu\text{eV}} \right). \quad (\text{B.17})$$

B.3 Microwave techniques

The FUNK++ experiment will be setup to probe HPs with (sub)-meV masses or microwave frequencies (GHz and THz). Luckily, there are plenty of excellent detectors in this regime and which have been ironed-out by radio astronomy. In this section, we briefly review the sensitivity equation conventionally applied in radio technology, and we describe the basics of a detection technique applicable for microwave detection with FUNK++. References and additional materials can be found in [100, 128, 129].

Radiometer equation

In the radio or microwave regime, we usually talk about signal power or noise power and express them, conveniently, in terms of temperatures. Considering that we deal with low energy photons, the noise power P of a radio antenna is typically described as the power delivered at the terminal of a noiseless antenna fed by a black-body radiator at temperature T , and whose spectrum can be approximated by the Rayleigh-Jeans law. In this case, the noise power in the bandwidth $\Delta\nu$ is given by

$$P = k_B T \Delta\nu, \quad (\text{B.18})$$

where k_B is the Boltzmann constant. In other terms, the temperature T can be interpreted as the power per unit bandwidth.

^c The voltage is a random variable, because of the random nature of noises.

In practice, we measure the voltage^c V_L delivered at the antenna load, and in general, we want to estimate some input voltage V from the measurement of V_L . For *square-law* detectors the delivered voltage is squared, such that

$$V_L \propto V^2 \propto P \propto T. \quad (\text{B.19})$$

Typically, V_L is also averaged (integrated over time) by an integrator circuit in the back-end post detection. Hence, during an integration time τ , we essentially average over $N \approx \tau \Delta\nu$ independent samples of V_L . The uncertainty over the average $\langle V_L \rangle$ is then given by

$$\sigma_{\langle V_L \rangle} \approx \frac{\sigma_{V_L}}{\sqrt{N}} \approx \frac{\langle V_L \rangle}{\sqrt{\tau \Delta\nu}}. \quad (\text{B.20})$$

The last step follows from an exponential distribution of V_L , generally observed for square-law detectors. In terms of temperature and using Eq. (B.19), we have

$$\sigma_{\langle T \rangle} \propto \frac{\langle T \rangle}{\sqrt{\tau \Delta\nu}}. \quad (\text{B.21})$$

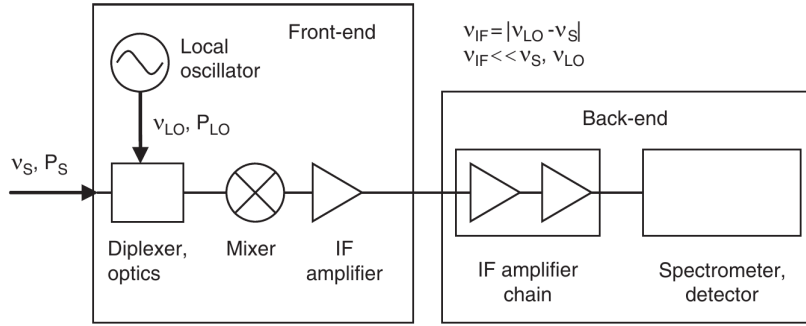


Figure B.1: Scheme of a heterodyne receiver. Figure was taken from [100].

For a given detector arrangement, the system temperature T_{sys} (further explained later) is defined as the overall measured noise-power, and can be written as

$$T_{\text{sys}} = T_a + T_{\text{rec}}. \quad (\text{B.22})$$

T_a is called the antenna temperature and it refers to the temperature due to external sources (signal and or background) observed by the antenna. T_{rec} is the receiver noise temperature, introduced at various stages of the detection chain (mixer, amplifiers, filters, ...). T_{rec} can be understood as the increase of signal seen by a noiseless receiver, transferring to its load the equivalent output power as generated by a noisy receiver. Then, Eq. (B.21) is often written as

$$\sigma_{\langle T \rangle} = \frac{k_{\text{rec}} T_{\text{sys}}}{\sqrt{\tau \Delta \nu}}. \quad (\text{B.23})$$

This is known as the radiometer equation and it represents the minimum detectable temperature fluctuation, for a detector setup with a system temperature T_{sys} . k_{rec} is constant but depending on the receiver (typically around 1 or 2). Finally, the minimum detectable power P_{det} at the antenna terminal is given by

$$\begin{aligned} P_{\text{det}} &= k_B \sigma_{\langle T \rangle} \Delta \nu \\ &= k_B k_{\text{rec}} T_{\text{sys}} \sqrt{\frac{\Delta \nu}{\Delta t}}, \end{aligned} \quad (\text{B.24})$$

where $\Delta t = n\tau$, for n independent sample integrations.

Heterodyne detection

The heterodyne principle is legitimately the standard technique for radio and microwave detections. The basic setup consists of two stages, as illustrated in Fig. B.1. First a front-end receiver, generally consisting of a local oscillator

(LO) at fixed reference frequency ν_{LO} , a diplexer to couple the input-signal frequency ν_{S} with the LO, a mixer which delivers the so-called intermediate frequency (IF), and a preamplifier for the IF signal. In the back-end, this is followed by a series of amplifiers and a spectrometer or detector to measure the IF.

The essence of the heterodyne detection lies in the mixer. The latter is specifically designed to deliver a down-converted or intermediate frequency $\nu_{\text{IF}} = \nu_{\text{LO}} - \nu_{\text{S}}$, and auxiliary, a higher mode $\nu_{\text{LO}} + \nu_{\text{S}}$. The difference of frequencies is called the lower sideband, and their sum is the upper sideband. These are somewhat relevant for the noise temperature of the mixer (single sideband or double sideband). Most importantly, the down-conversion allows the use of receivers with relatively slow response-time, to cope with higher frequency input-signals.

Let us consider a typical front-end receiver, as shown in Fig. B.1. We denote by T_{S} the signal noise temperature (this is the antenna temperature), T_{M} the temperature of the mixer^d with some conversion loss factor L_{M} . We suppose that the transferred IF passes then through two amplifiers with gain $G_{\text{IF},i}$ and noise temperature T_i ($i = 1, 2$) before being delivered to the load. In this case, the noise power P_{L} measured at the receiver load, withing a bandwidth $\Delta\nu$ set prior to the detection, is given by

^d Likewise, T_{M} can be interpreted as the noise temperature feeding a noiseless mixer, which generates the same output power as a noisy mixer.

$$\begin{aligned} P_{\text{L}} &= k_{\text{B}} \left(G_{\text{IF},1} G_{\text{IF},2} \frac{T_{\text{S}} + T_{\text{M}}}{L_{\text{M}}} + G_{\text{IF},1} G_{\text{IF},2} T_1 + G_{\text{IF},2} T_2 \right) \Delta\nu \\ &= k_{\text{B}} \underbrace{\frac{G_{\text{IF},1} G_{\text{IF},2}}{L_{\text{M}}}}_G \left(T_{\text{S}} + T_{\text{M}} + \underbrace{L_{\text{M}} T_1 + \frac{L_{\text{M}} T_2}{G_{\text{IF},1}}}_{T_{\text{rec}}} \right) \Delta\nu, \end{aligned} \quad (\text{B.25})$$

where G is the effective gain of the amplifier cascade. In general, the system temperature can then be written as

$$T_{\text{sys}} = T_{\text{a}} + T_{\text{rec}} = T_{\text{a}} + l_1 T_1 + \frac{l_2 T_2}{G_1} + \frac{l_3 T_3}{G_1 G_2} + \dots \quad (\text{B.26})$$

Here, the antenna temperature T_{a} includes the noise temperature due the observed sources and the all components of the antenna transmission line. Therefore, for a good receiver we generally need to worry that the first stage of the detection chain has a low-noise temperature and a large gain G_1 . The noise contribution from the subsequent stage is suppressed by G_1^{-1} , and so forth, as seen in Eq. (B.26).

Finally, let us not that in most cases, the noise temperature does not refer to the physical temperature of the source. However, for components such as resistors and transmission lines, the noise temperature is equivalent

to their physical temperature. In this case, special care should be taken to reduce the noise. On the other hand, it is also conceivable to reduce the noise temperature seen at the antenna terminal, for instance, by lining the setup with a Faraday shield. For estimating the sensitivity of $F_{\text{UNK++}}$, we assume that the background reduction is achievable to the point that the system temperature is mostly dominated by the temperature of a double sideband mixer. Examples of commonly used mixer devices are Schottky diodes, Hot Electron Bolometers and SIS junctions.

Acknowledgments

To begin with, I am most grateful to Prof. Ralph Engel and Prof. Thomas Schwetz for giving me the opportunity to embark on this PhD adventure three years ago and for agreeing to supervise and evaluate this thesis. Alongside, I address my warmest thanks to Dr. Darko Veberič for co-supervising and for the enormous support in many aspects of this work.

I also wish to thank Dr. Babette Döbrich for pointing me in the direction of this fantastic topic. Special thanks to all the FUNK collaborators, without whom, this experiment would not have been possible. I am particularly thankful to my colleague Christoph Schaefer for all the help at the beginning of my PhD. Further, I thank Dr. Michael Unger for providing correction on the Zusammenfassung of this thesis.

Next, I would like to thank Sabine Bucher, Doris Wochele, Barbara Lepold, Anna Friedrich, and Hartmut Speck for making my stay at IKP and in Karlsruhe rather smooth. Many thanks to all *Auger* and *Icecube people* for the good moments at the institute. On this note, I also thank Joachim Debatin with whom I had the pleasure to share office with, in the last three years.

Turning now to my “brudili frudili totetili brownie” Alvaro and Alvaro, or in short Alvaros, thank you for the friendship and for sharing this meloco-journey with me. Not to forget, friends from the world, Zoe Wyatt, Kotryna Stupnianek (many that I would forget to mention actually). . . and friends from Madagascar (they all have very long names and I would rather keep this to one-page so let’s wrap up).

Lastly, my heartfelt gratitude goes to my family for their unconditional support throughout this journey.

Danke. Tschüss!

Acronyms

List of acronyms sorted alphabetically according to the short version.

ADC	Analog-to-Digital Converter
BBN	Big Bang Nucleosynthesis
CMB	Cosmic Microwave Background
CR	Cosmic Ray
DAQ	Data Acquisition
DM	Dark Matter
FoV	Field of View
HP	Hidden Photon
HPDM	Hidden-Photon Dark Matter
IR	Infrared
LED	Light-Emitting Diode
LSW	Light-Shinning through a Wall
PMT	Photomultiplier Tube
ROI	Region Of Interest
SM	Standard Model
SPE	Single Photoelectron
UV	Ultraviolet
WIMP	Weakly Interacting Massive Particle
WISP	Weakly Interacting Slim Particle

Bibliography

- [1] F. Zwicky, Die Rotverschiebung von extragalaktischen Nebeln, *Helvetica Physica Acta* 6 (1933) 110–127.
- [2] T. S. van Albada, J. N. Bahcall, K. Begeman, R. Sancisi, Distribution of dark matter in the spiral galaxy NGC 3198., *Astrophys. J.* 295 (1985) 305–313. doi:[10.1086/163375](https://doi.org/10.1086/163375).
- [3] S. W. Allen, R. W. Schmidt, A. C. Fabian, Cosmological constraints from the x-ray gas mass fraction in relaxed lensing clusters observed with Chandra, *Mon. Not. Roy. Astron. Soc.* 334 (2002) L11. arXiv:[astro-ph/0205007](https://arxiv.org/abs/astro-ph/0205007), doi:[10.1046/j.1365-8711.2002.05601.x](https://doi.org/10.1046/j.1365-8711.2002.05601.x).
- [4] A. Refregier, Weak gravitational lensing by large scale structure, *Ann. Rev. Astron. Astrophys.* 41 (2003) 645–668. arXiv:[astro-ph/0307212](https://arxiv.org/abs/astro-ph/0307212), doi:[10.1146/annurev.astro.41.111302.102207](https://doi.org/10.1146/annurev.astro.41.111302.102207).
- [5] D. Clowe, M. Bradac, A. H. Gonzalez, M. Markevitch, S. W. Randall, C. Jones, D. Zaritsky, A direct empirical proof of the existence of dark matter, *Astrophys. J.* 648 (2006) L109–L113. arXiv:[astro-ph/0608407](https://arxiv.org/abs/astro-ph/0608407), doi:[10.1086/508162](https://doi.org/10.1086/508162).
- [6] G. R. Blumenthal, S. M. Faber, J. R. Primack, M. J. Rees, Formation of Galaxies and Large Scale Structure with Cold Dark Matter, *Nature* 311 (1984) 517–525, [96(1984)]. doi:[10.1038/311517a0](https://doi.org/10.1038/311517a0).
- [7] D. N. Spergel, et al., WMAP, Wilkinson Microwave Anisotropy Probe (WMAP) three year results: implications for cosmology, *Astrophys. J. Suppl.* 170 (2007) 377. arXiv:[astro-ph/0603449](https://arxiv.org/abs/astro-ph/0603449), doi:[10.1086/513700](https://doi.org/10.1086/513700).
- [8] M. Tanabashi, et al., Particle Data Group, Review of Particle Physics, *Phys. Rev. D* 98 (3) (2018) 030001. doi:[10.1103/PhysRevD.98.030001](https://doi.org/10.1103/PhysRevD.98.030001).
- [9] M. Milgrom, MOND theory, *Can. J. Phys.* 93 (2) (2015) 107–118. arXiv:[1404.7661](https://arxiv.org/abs/1404.7661), doi:[10.1139/cjp-2014-0211](https://doi.org/10.1139/cjp-2014-0211).
- [10] L. Wyrzykowski, et al., The ogle view of microlensing towards the magellanic clouds - iv. ogle-iii smc data and final conclusions on

- machos, *Monthly Notices of the Royal Astronomical Society* 416 (4) (2011) 2949–2961. doi:[10.1111/j.1365-2966.2011.19243.x](https://doi.org/10.1111/j.1365-2966.2011.19243.x).
- [11] N. Aghanim, et al., Planck, Planck 2018 results. VI. Cosmological parameters (2018) [arXiv:1807.06209](https://arxiv.org/abs/1807.06209).
- [12] S. P. Martin, A Supersymmetry primer (1997) 1–98[Adv. Ser. Direct. High Energy Phys.18,1(1998)]. [arXiv:hep-ph/9709356](https://arxiv.org/abs/hep-ph/9709356), doi:[10.1142/9789812839657_0001](https://doi.org/10.1142/9789812839657_0001), [10.1142/9789814307505_0001](https://doi.org/10.1142/9789814307505_0001).
- [13] E. Aprile, et al., XENON, Dark Matter Search Results from a One Ton-Year Exposure of XENON1T, *Phys. Rev. Lett.* 121 (11) (2018) 111302. [arXiv:1805.12562](https://arxiv.org/abs/1805.12562), doi:[10.1103/PhysRevLett.121.111302](https://doi.org/10.1103/PhysRevLett.121.111302).
- [14] J. Jaeckel, A. Ringwald, The Low-Energy Frontier of Particle Physics, *Ann. Rev. Nucl. Part. Sci.* 60 (2010) 405–437. [arXiv:1002.0329](https://arxiv.org/abs/1002.0329), doi:[10.1146/annurev.nucl.012809.104433](https://doi.org/10.1146/annurev.nucl.012809.104433).
- [15] M. Goodsell, J. Jaeckel, J. Redondo, A. Ringwald, Naturally Light Hidden Photons in LARGE Volume String Compactifications, *JHEP* 11 (2009) 027. [arXiv:0909.0515](https://arxiv.org/abs/0909.0515), doi:[10.1088/1126-6708/2009/11/027](https://doi.org/10.1088/1126-6708/2009/11/027).
- [16] B. Holdom, Two U(1)'s and Epsilon Charge Shifts, *Phys. Lett.* 166B (1986) 196–198. doi:[10.1016/0370-2693\(86\)91377-8](https://doi.org/10.1016/0370-2693(86)91377-8).
- [17] J. Jaeckel, A force beyond the Standard Model - Status of the quest for hidden photons, *Frascati Phys. Ser.* 56 (2012) 172–192. [arXiv:1303.1821](https://arxiv.org/abs/1303.1821).
- [18] A. E. Nelson, J. Scholtz, Dark Light, Dark Matter and the Misalignment Mechanism, *Phys. Rev. D* 84 (2011) 103501. [arXiv:1105.2812](https://arxiv.org/abs/1105.2812), doi:[10.1103/PhysRevD.84.103501](https://doi.org/10.1103/PhysRevD.84.103501).
- [19] P. Arias, D. Cadamuro, M. Goodsell, J. Jaeckel, J. Redondo, A. Ringwald, WISPy Cold Dark Matter, *JCAP* 1206 (2012) 013. [arXiv:1201.5902](https://arxiv.org/abs/1201.5902), doi:[10.1088/1475-7516/2012/06/013](https://doi.org/10.1088/1475-7516/2012/06/013).
- [20] D. Horns, J. Jaeckel, A. Lindner, A. Lobanov, J. Redondo, A. Ringwald, Searching for WISPy Cold Dark Matter with a Dish Antenna, *JCAP* 1304 (2013) 016. [arXiv:1212.2970](https://arxiv.org/abs/1212.2970), doi:[10.1088/1475-7516/2013/04/016](https://doi.org/10.1088/1475-7516/2013/04/016).
- [21] J. Suzuki, Y. Inoue, T. Horie, M. Minowa, Hidden photon CDM search at Tokyo, in: Proceedings, 11th Patras Workshop on Axions, WIMPs and WISPs (Axion-WIMP 2015): Zaragoza, Spain, June 22-26, 2015, 2015,

- pp. 145–148. [arXiv:1509.00785](#), [doi:10.3204/DESY-PROC-2015-02/junya_suzuki](#).
- [22] J. Suzuki, T. Horie, Y. Inoue, M. Minowa, Experimental Search for Hidden Photon CDM in the eV mass range with a Dish Antenna, JCAP 1509 (09) (2015) 042. [arXiv:1504.00118](#), [doi:10.1088/1475-7516/2015/09/042](#), [10.1088/1475-7516/2015/9/042](#).
- [23] P. W. Graham, J. Mardon, S. Rajendran, Vector Dark Matter from Inflationary Fluctuations, Phys. Rev. D93 (10) (2016) 103520. [arXiv:1504.02102](#), [doi:10.1103/PhysRevD.93.103520](#).
- [24] A. S. Goldhaber, M. M. Nieto, New geomagnetic limit on the mass of the photon, Phys. Rev. Lett. 21 (1968) 567–569. [doi:10.1103/PhysRevLett.21.567](#).
- [25] A. S. GOLDHABER, M. M. NIETO, Terrestrial and extraterrestrial limits on the photon mass, Rev. Mod. Phys. 43 (1971) 277–296. [doi:10.1103/RevModPhys.43.277](#).
- [26] J. Redondo, Helioscope Bounds on Hidden Sector Photons, JCAP 0807 (2008) 008. [arXiv:0801.1527](#), [doi:10.1088/1475-7516/2008/07/008](#).
- [27] H. An, M. Pospelov, J. Pradler, New stellar constraints on dark photons, Phys. Lett. B725 (2013) 190–195. [arXiv:1302.3884](#), [doi:10.1016/j.physletb.2013.07.008](#).
- [28] J. Redondo, G. Raffelt, Solar constraints on hidden photons re-visited, JCAP 1308 (2013) 034. [arXiv:1305.2920](#), [doi:10.1088/1475-7516/2013/08/034](#).
- [29] A. Mirizzi, J. Redondo, G. Sigl, Microwave Background Constraints on Mixing of Photons with Hidden Photons, JCAP 0903 (2009) 026. [arXiv:0901.0014](#), [doi:10.1088/1475-7516/2009/03/026](#).
- [30] J. Redondo, M. Postma, Massive hidden photons as lukewarm dark matter, JCAP 0902 (2009) 005. [arXiv:0811.0326](#), [doi:10.1088/1475-7516/2009/02/005](#).
- [31] J. Jaeckel, J. Redondo, A. Ringwald, Signatures of a hidden cosmic microwave background, Phys. Rev. Lett. 101 (2008) 131801. [arXiv:0804.4157](#), [doi:10.1103/PhysRevLett.101.131801](#).
- [32] L. B. Okun, Limits of Electrodynamics: Paraphotons?, Sov. Phys. JETP 56 (1982) 502, [Zh. Eksp. Teor. Fiz.83,892(1982)].

- [33] D. F. Bartlett, P. E. Goldhagen, E. A. Phillips, Experimental test of coulomb's law, *Phys. Rev. D* 2 (1970) 483–487. doi:[10.1103/PhysRevD.2.483](https://doi.org/10.1103/PhysRevD.2.483).
- [34] D. F. Bartlett, S. Lög, Limits on an electromagnetic fifth force, *Phys. Rev. Lett.* 61 (1988) 2285–2287. doi:[10.1103/PhysRevLett.61.2285](https://doi.org/10.1103/PhysRevLett.61.2285).
- [35] S. G. Karshenboim, Constraints on a long-range spin-independent interaction from precision atomic physics, *Phys. Rev. D* 82 (2010) 073003. arXiv:[1005.4872](https://arxiv.org/abs/1005.4872), doi:[10.1103/PhysRevD.82.073003](https://doi.org/10.1103/PhysRevD.82.073003).
- [36] J. Jaeckel, S. Roy, Spectroscopy as a test of Coulomb's law: A Probe of the hidden sector, *Phys. Rev. D* 82 (2010) 125020. arXiv:[1008.3536](https://arxiv.org/abs/1008.3536), doi:[10.1103/PhysRevD.82.125020](https://doi.org/10.1103/PhysRevD.82.125020).
- [37] M. Pospelov, Secluded U(1) below the weak scale, *Phys. Rev. D* 80 (2009) 095002. arXiv:[0811.1030](https://arxiv.org/abs/0811.1030), doi:[10.1103/PhysRevD.80.095002](https://doi.org/10.1103/PhysRevD.80.095002).
- [38] J. R. Batley, et al., NA48/2, Search for the dark photon in π^0 decays, *Phys. Lett. B* 746 (2015) 178–185. arXiv:[1504.00607](https://arxiv.org/abs/1504.00607), doi:[10.1016/j.physletb.2015.04.068](https://doi.org/10.1016/j.physletb.2015.04.068).
- [39] D. Banerjee, et al., NA64 Collaboration, Search for invisible decays of sub-gev dark photons in missing-energy events at the cern sps, *Phys. Rev. Lett.* 118 (2017) 011802. doi:[10.1103/PhysRevLett.118.011802](https://doi.org/10.1103/PhysRevLett.118.011802).
- [40] J. P. Lees, et al., BaBar Collaboration, Search for invisible decays of a dark photon produced in e^+e^- collisions at babar, *Phys. Rev. Lett.* 119 (2017) 131804. doi:[10.1103/PhysRevLett.119.131804](https://doi.org/10.1103/PhysRevLett.119.131804).
- [41] M. Bauer, P. Foldenauer, J. Jaeckel, Hunting All the Hidden Photons, *JHEP* 07 (2018) 094, [*JHEP*18,094(2020)]. arXiv:[1803.05466](https://arxiv.org/abs/1803.05466), doi:[10.1007/JHEP07\(2018\)094](https://doi.org/10.1007/JHEP07(2018)094).
- [42] P. Ilten, Y. Soreq, M. Williams, W. Xue, Serendipity in dark photon searches, *JHEP* 06 (2018) 004. arXiv:[1801.04847](https://arxiv.org/abs/1801.04847), doi:[10.1007/JHEP06\(2018\)004](https://doi.org/10.1007/JHEP06(2018)004).
- [43] A. Hook, E. Izaguirre, J. G. Wacker, Model Independent Bounds on Kinetic Mixing, *Adv. High Energy Phys.* 2011 (2011) 859762. arXiv:[1006.0973](https://arxiv.org/abs/1006.0973), doi:[10.1155/2011/859762](https://doi.org/10.1155/2011/859762).
- [44] K. Ehret, et al., ALPS, Resonant laser power build-up in ALPS: A 'Light-shining-through-walls' experiment, *Nucl. Instrum. Meth. A* 612 (2009) 83–96. arXiv:[0905.4159](https://arxiv.org/abs/0905.4159), doi:[10.1016/j.nima.2009.10.102](https://doi.org/10.1016/j.nima.2009.10.102).

- [45] R. Cameron, et al., Search for nearly massless, weakly coupled particles by optical techniques, *Phys. Rev. D* 47 (1993) 3707–3725. doi:[10.1103/PhysRevD.47.3707](https://doi.org/10.1103/PhysRevD.47.3707).
- [46] M. Ahlers, H. Gies, J. Jaeckel, J. Redondo, A. Ringwald, Light from the hidden sector, *Phys. Rev. D* 76 (2007) 115005. arXiv:[0706.2836](https://arxiv.org/abs/0706.2836), doi:[10.1103/PhysRevD.76.115005](https://doi.org/10.1103/PhysRevD.76.115005).
- [47] R. Bähre, et al., Any light particle search II —Technical Design Report, *JINST* 8 (2013) T09001. arXiv:[1302.5647](https://arxiv.org/abs/1302.5647), doi:[10.1088/1748-0221/8/09/T09001](https://doi.org/10.1088/1748-0221/8/09/T09001).
- [48] S. Andriamonje, et al., CAST, An Improved limit on the axion-photon coupling from the CAST experiment, *JCAP* 0704 (2007) 010. arXiv:[hep-ex/0702006](https://arxiv.org/abs/hep-ex/0702006), doi:[10.1088/1475-7516/2007/04/010](https://doi.org/10.1088/1475-7516/2007/04/010).
- [49] S. J. Asztalos, et al., Squid-based microwave cavity search for dark-matter axions, *Phys. Rev. Lett.* 104 (2010) 041301. doi:[10.1103/PhysRevLett.104.041301](https://doi.org/10.1103/PhysRevLett.104.041301).
- [50] L. D. Duffy, P. Sikivie, D. B. Tanner, S. J. Asztalos, C. Hagmann, D. Kinion, L. J. Rosenberg, K. van Bibber, D. B. Yu, R. F. Bradley, ADMX, A high resolution search for dark-matter axions, *Phys. Rev. D* 74 (2006) 012006. arXiv:[astro-ph/0603108](https://arxiv.org/abs/astro-ph/0603108), doi:[10.1103/PhysRevD.74.012006](https://doi.org/10.1103/PhysRevD.74.012006).
- [51] J. Jaeckel, A. Ringwald, A Cavity Experiment to Search for Hidden Sector Photons, *Phys. Lett. B* 659 (2008) 509–514. arXiv:[0707.2063](https://arxiv.org/abs/0707.2063), doi:[10.1016/j.physletb.2007.11.071](https://doi.org/10.1016/j.physletb.2007.11.071).
- [52] A. Wagner, et al., ADMX, A Search for Hidden Sector Photons with ADMX, *Phys. Rev. Lett.* 105 (2010) 171801. arXiv:[1007.3766](https://arxiv.org/abs/1007.3766), doi:[10.1103/PhysRevLett.105.171801](https://doi.org/10.1103/PhysRevLett.105.171801).
- [53] A. P. Lobanov, H.-S. Zechlin, D. Horns, Astrophysical searches for a hidden-photon signal in the radio regime, *Phys. Rev. D* 87 (2013) 065004. doi:[10.1103/PhysRevD.87.065004](https://doi.org/10.1103/PhysRevD.87.065004).
- [54] A. J. Millar, G. G. Raffelt, J. Redondo, F. D. Steffen, Dielectric Haloscopes to Search for Axion Dark Matter: Theoretical Foundations, *JCAP* 1701 (01) (2017) 061. arXiv:[1612.07057](https://arxiv.org/abs/1612.07057), doi:[10.1088/1475-7516/2017/01/061](https://doi.org/10.1088/1475-7516/2017/01/061).
- [55] M. Trodden, S. M. Carroll, TASI lectures: Introduction to cosmology, in: *Progress in string theory. Proceedings, Summer School, TASI 2003, Boulder, USA, June 2-27, 2003, 2004*, pp. 703–793, [,703(2004)]. arXiv:[astro-ph/0401547](https://arxiv.org/abs/astro-ph/0401547).

- [56] M. Pospelov, A. Ritz, M. B. Voloshin, Bosonic super-WIMPs as keV-scale dark matter, *Phys. Rev. D* 78 (2008) 115012. [arXiv:0807.3279](#), [doi:10.1103/PhysRevD.78.115012](#).
- [57] A. Aguilar-Arevalo, et al., DAMIC, First Direct-Detection Constraints on eV-Scale Hidden-Photon Dark Matter with DAMIC at SNOLAB, *Phys. Rev. Lett.* 118 (14) (2017) 141803. [arXiv:1611.03066](#), [doi:10.1103/PhysRevLett.118.141803](#).
- [58] A. Aguilar-Arevalo, et al., DAMIC, Constraints on Light Dark Matter Particles Interacting with Electrons from DAMIC at SNOLAB (2019)[arXiv:1907.12628](#).
- [59] I. M. Bloch, R. Essig, K. Tobioka, T. Volansky, T.-T. Yu, Searching for Dark Absorption with Direct Detection Experiments, *JHEP* 06 (2017) 087. [arXiv:1608.02123](#), [doi:10.1007/JHEP06\(2017\)087](#).
- [60] R. Engel, et al., FUNK Experiment, Search for hidden-photon Dark Matter with FUNK, in: Proceedings, 13th Patras Workshop on Axions, WIMPs and WISPs, (PATRAS 2017): Thessaloniki, Greece, 15 May 2017 - 19, 2017, 2017. [arXiv:1711.02961](#).
- [61] D. Veberič, et al., FUNK Experiment, Search for hidden-photon dark matter with the FUNK experiment, *PoS ICRC2017* (2018) 880. [arXiv:1711.02958](#), [doi:10.22323/1.301.0880](#).
- [62] S. Knirck, T. Yamazaki, Y. Okesaku, S. Asai, T. Idehara, T. Inada, First results from a hidden photon dark matter search in the meV sector using a plane-parabolic mirror system, *JCAP* 1811 (11) (2018) 031. [arXiv:1806.05120](#), [doi:10.1088/1475-7516/2018/11/031](#).
- [63] P. Brun, L. Chevalier, C. Flouzat, Direct Searches for Hidden-Photon Dark Matter with the SHUKET Experiment, *Phys. Rev. Lett.* 122 (20) (2019) 201801. [arXiv:1905.05579](#), [doi:10.1103/PhysRevLett.122.201801](#).
- [64] P. Brun, et al., MADMAX, A new experimental approach to probe QCD axion dark matter in the mass range above 40 μeV , *Eur. Phys. J. C* 79 (3) (2019) 186. [arXiv:1901.07401](#), [doi:10.1140/epjc/s10052-019-6683-x](#).
- [65] J. Jaeckel, J. Redondo, Resonant to broadband searches for cold dark matter consisting of weakly interacting slim particles, *Phys. Rev. D* 88 (11) (2013) 115002. [arXiv:1308.1103](#), [doi:10.1103/PhysRevD.88.115002](#).

- [66] J. Jaeckel, S. Knirck, Directional Resolution of Dish Antenna Experiments to Search for WISPy Dark Matter, JCAP 1601 (2016) 005. [arXiv:1509.00371](#), [doi:10.1088/1475-7516/2016/01/005](#).
- [67] J. Jaeckel, J. Redondo, An antenna for directional detection of WISPy dark matter, JCAP 1311 (2013) 016. [arXiv:1307.7181](#), [doi:10.1088/1475-7516/2013/11/016](#).
- [68] M. Polyanskiy, [Refractive Index](#), accessed on July 29, 2020.
- [69] D. Veberic, et al., FUNK, Search for dark matter in the hidden-photon sector with a large spherical mirror, PoS ICRC2015 (2016) 1191. [arXiv:1509.02386](#), [doi:10.22323/1.236.1191](#).
- [70] J. Abraham, et al., Pierre Auger, The Fluorescence Detector of the Pierre Auger Observatory, Nucl. Instrum. Meth. A 620 (2010) 227–251. [arXiv:0907.4282](#), [doi:10.1016/j.nima.2010.04.023](#).
- [71] J. Abraham, et al., Pierre Auger, Properties and performance of the prototype instrument for the Pierre Auger Observatory, Nucl. Instrum. Meth. A 523 (2004) 50–95. [doi:10.1016/j.nima.2003.12.012](#).
- [72] Christoph Schäfer, Suche nach photonartigen Teilchen der Dunklen Materie im Elektronenvolt-Massenbereich mit einem sphärischen Spiegel, Bachelor thesis, KIT (2015).
- [73] ET Enterprises, [9107B series data sheet](#), accessed on July 29, 2020.
- [74] ET Enterprises, [Understanding Photomultipliers](#), accessed on July 29, 2020.
- [75] B. Döbrich, et al., The FUNK search for Hidden Photon Dark Matter in the eV range, in: Photon 2015: International Conference on the Structure and Interactions of the Photon and 21th International Workshop on Photon-Photon Collisions and International Workshop on High Energy Photon Linear Colliders Novosibirsk, Russia, June 15-19, 2015, 2015. [arXiv:1510.05869](#).
- [76] ET Enterprises, [Practical Photon Counting](#), accessed on July 29, 2020.
- [77] Christoph Schäfer, Search for Hidden-Photon Dark-Matter with a Spherical Mirror, Master thesis, KIT (2018).
- [78] CAEN, [User's Manual Mod. SY127 40 Channel High Voltage System](#), accessed on July 29, 2020.
- [79] ET Enterprises, [FACT50/LCT50 data sheet](#), accessed on July 29, 2020.

- [80] OWIS, [LTM 60 Product Information](#), accessed on July 29, 2020.
- [81] UNIBLITZ, [NS65B 65mm Bi-Stable Optical Shutter](#), accessed on July 29, 2020.
- [82] THORLABS, [MFF101 and MFF102 Motorized Filter Flippers](#), accessed on July 29, 2020.
- [83] PICO Technology, [PicoScope 6000 Series](#), accessed on July 29, 2020.
- [84] CAEN, [DT5751 2/4 Ch. 10 bit 2/1 GS/s Digitizer](#), accessed on July 29, 2020.
- [85] F. J. Lombard, F. Martin, Statistics of electron multiplication, *Review of Scientific Instruments* 32 (2) (1961) 200–201. doi:10.1063/1.1717310.
- [86] J. Prescott, A statistical model for photomultiplier single-electron statistics, *Nuclear Instruments and Methods (Netherlands) Formerly Nucl. Instrum. Changed to Nucl. Instrum. Methods Phys. Res.* 39 (1966) 173–179. doi:10.1016/0029-554X(66)90059-0.
- [87] H. H. Tan, A Statistical Model of the Photomultiplier Gain Process With Applications to Optical Pulse Detection, *Telecommunications and Data Acquisition Progress Report* 68 (1982) 55–67.
- [88] T. E. Harris, *The Theory of Branching Processes*, 1st Edition, Springer-Verlag, 1963.
- [89] E. H. Bellamy, G. Bellettini, F. Gervelli, M. Incagli, D. Lucchesi, C. Pagliarone, F. Zetti, Yu. Budagov, I. Chirikov-Zorin, S. Tokar, Absolute calibration and monitoring of a spectrometric channel using a photomultiplier, *Nucl. Instrum. Meth.* A339 (1994) 468–476. doi:10.1016/0168-9002(94)90183-X.
- [90] G. Bourlis, T. Avgitas, A. Tsirigotis, S. Tzamarias, KM3NeT, Characterization of the KM3NeT photomultipliers in the Hellenic Open University, *AIP Conf. Proc.* 1630 (1) (2015) 106–109. doi:10.1063/1.4902783.
- [91] Maxim Integrated, [DS18S20 High-Precision 1-Wire Digital Thermometer](#), accessed on July 29, 2020.
- [92] Bosch Sensortec, [BMP180 Digital pressure sensor](#), accessed on July 29, 2020.
- [93] M. Ambrosio, et al., MACRO, Seasonal variations in the underground muon intensity as seen by MACRO, *Astropart. Phys.* 7 (1997) 109–124. doi:10.1016/S0927-6505(97)00011-X.

- [94] G. Bellini, et al., Borexino, Cosmic-muon flux and annual modulation in Borexino at 3800 m water-equivalent depth, JCAP 1205 (2012) 015. [arXiv:1202.6403](#), [doi:10.1088/1475-7516/2012/05/015](#).
- [95] K. P. Arunbabu, et al., Dependence of the muon intensity on the atmospheric temperature measured by the GRAPES-3 experiment, *Astropart. Phys.* 94 (2017) 22–28. [doi:10.1016/j.astropartphys.2017.07.002](#).
- [96] J. Poirier, T. Catanach, Atmospheric Effects on Muon Flux at Project GRAND, in: *Proceedings, 32nd International Cosmic Ray Conference (ICRC 2011): Beijing, China, August 11-18, 2011, Vol. b*, p. 347. [doi:10.7529/ICRC2011/V11/0307](#).
- [97] S. Cecchini, M. Spurio, Atmospheric muons: experimental aspects (2012)[arXiv:1208.1171](#).
- [98] T. K. Gaisser, R. Engel, E. Resconi, *Cosmic Rays and Particle Physics*, 2nd Edition, Cambridge University Press, 2016. [doi:10.1017/CB09781139192194](#).
- [99] D. Chirkin, Fluxes of atmospheric leptons at 600-GeV - 60-TeV (2004)[arXiv:hep-ph/0407078](#).
- [100] E. Bründermann, H.-W. Hübers, M. F. Kimmitt, *Terahertz Techniques*, Springer Series in Optical Sciences, Springer, Berlin, 2012. [doi:10.1007/978-3-642-02592-1](#).
- [101] Rhode Scharz company, [Spectrometer \(XFFTS\)](#), accessed on July 29, 2020.
- [102] H. Hubers, M. F. Kimmitt, N. Hiromoto, E. Bründermann, Terahertz spectroscopy: System and sensitivity considerations, *IEEE Transactions on Terahertz Science and Technology* 1 (1) (2011) 321–331.
- [103] Philips Photonics, *Photomultiplier Tubes: Principles and Applications* (1994).
- [104] P. Coates, Thermionic emission from photocathodes, *J. Phys. D Appl. Phys.* 5 (8) (1972) 1489–1498. [doi:10.1088/0022-3727/5/8/319](#).
- [105] Hamamatsu, [Photomultiplier Tubes: Basics and Applications](#), accessed on July 29, 2020.
- [106] K. Helbing, et al., Light emission in Amanda pressure spheres, Tech. rep., [AMANDA-IR/20030701](#) (2003).

- [107] M. G. Aartsen, et al., IceCube, The IceCube Neutrino Observatory: Instrumentation and Online Systems, *JINST* 12 (03) (2017) P03012. [arXiv:1612.05093](#), [doi:10.1088/1748-0221/12/03/P03012](#).
- [108] P. Lipari, Lepton spectra in the earth's atmosphere, *Astropart. Phys.* 1 (1993) 195–227. [doi:10.1016/0927-6505\(93\)90022-6](#).
- [109] O. Allkofer, K. Carstensen, W. Dau, The absolute cosmic ray muon spectrum at sea level, *Physics Letters B* 36 (4) (1971) 425 – 427. [doi:10.1016/0370-2693\(71\)90741-6](#).
- [110] B. C. Rastin, An accurate measurement of the sea-level muon spectrum within the range 4 to 3000 GeV/c, *Journal of Physics G: Nuclear Physics* 10 (11) (1984) 1609–1628. [doi:10.1088/0305-4616/10/11/017](#).
- [111] I. P. Ivanenko, et al., Results of investigation of muon fluxes of super-high energy cosmic rays with X-ray emulsion chambers, in: *Proc. 19th Int. Cosmic Ray Conf. (NASA Conf. Publ. No. 2376)*, Vol. 8, 1985, p. 210.
- [112] J. Kremer, et al., Measurements of ground-level muons at two geomagnetic locations, *Phys. Rev. Lett.* 83 (1999) 4241–4244. [doi:10.1103/PhysRevLett.83.4241](#).
- [113] E. V. Bugaev, A. Misaki, V. A. Naumov, T. S. Sinegovskaya, S. I. Sinegovsky, N. Takahashi, Atmospheric muon flux at sea level, underground and underwater, *Phys. Rev. D* 58 (1998) 054001. [arXiv:hep-ph/9803488](#), [doi:10.1103/PhysRevD.58.054001](#).
- [114] P. K. F. Grieder, *Cosmic rays at earth: Researcher's reference, manual and data book*, Elsevier, Amsterdam, 2001.
- [115] W. Lohmann, R. Kopp, R. Voss, *Energy Loss of Muons in the Energy Range 1-GeV to 10000-GeV* (1985).
- [116] G. Badino, Is it always dark in caves?, *Int. J. Speleol.* B 29 (2000) 89–126. [doi:10.5038/1827-806X.29.1.5](#).
- [117] F. Jones, The Refractivity of Air, *J. Res. Nat. Bur. Stand.* 86 (1) (1981). [doi:10.6028/jres.086.002](#).
- [118] Johanna Linek, Investigation of the muon induced background at the KATRIN main spectrometer, Master thesis, KIT (2015).
- [119] G. Molenberghs, G. Verbeke, C. G. B. Demétrio, A. M. C. Vieira, A Family of Generalized Linear Models for Repeated Measures with

- Normal and Conjugate Random Effects, *Stat. Sci.* 25 (3) (2010) 325–347. doi:10.1214/10-STS328.
- [120] T. Kozubowski, K. Podgorski, Distributional properties of the negative binomial lévy process 29 (Fasc. 1) (2009) 43–71.
- [121] S. Boziev, Why fluctuations in multiplicity of muon groups do not conform to a Poisson distribution?, in: *Proceedings of 23rd International Cosmic Ray Conference, Calgary, Canada, July 19-30, 1993, Vol. 4, 1993*, pp. 403–406.
- [122] F. Henningsen, *STRAW -Strings for Absorption Length in Water*, Poster at the Invisible18 School, accessed on July 29, 2020.
- [123] R. Abbasi, et al., IceCube, Calibration and Characterization of the IceCube Photomultiplier Tube, *Nucl. Instrum. Meth. A* 618 (2010) 139–152. arXiv:1002.2442, doi:10.1016/j.nima.2010.03.102.
- [124] H. O. Meyer, Spontaneous electron emission from a cold surface, *EPL (Europhysics Letters)* 89 (5) (2010) 58001. doi:10.1209/0295-5075/89/58001.
- [125] K. Dressler, L. Spitzer, Photomultiplier tube pulses induced by γ rays, *Review of Scientific Instruments* 38 (3) (1967) 436–438. doi:10.1063/1.1720730.
- [126] Hamamatsu, *Photon Counting*, accessed on July 29, 2020.
- [127] G. J. Feldman, R. D. Cousins, A Unified approach to the classical statistical analysis of small signals, *Phys. Rev. D* 57 (1998) 3873–3889. arXiv:physics/9711021, doi:10.1103/PhysRevD.57.3873.
- [128] M. E. Tiuri, Radio astronomy receivers, *IEEE Transactions on Antennas and Propagation* 12 (7) (1964) 930–938. doi:10.1109/TAP.1964.1138345.
- [129] Felix Werner, Investigation of the muon induced background at the KATRIN main spectrometer, Phd thesis, KIT (2013).